Universidade de São Paulo

Università degli Studi di Padova

Excited state lifetimes in the fp - shell mirror nuclei

Rafael Escudeiro

Supervisors: Nilberto Heder Medina

Francesco Recchia

Thesis submitted to the Institute of Physics of the University of São Paulo as a requirement to obtain the degree of Doctor of Science, under a double degree agreement with University of Padova.

Instituto de Física - USP

President of the Graduate Commission: Prof. Dr. Luis Raul W. Abramo

Dipartimento di Fisica e Astronomia "G. Galilei" - UNIPD

Coordinator of the Doctoral Course: Prof. Giulio Monaco

Examining Committee:

Dr. Nilberto Heder Medina (IFUSP)

Dr. Francesco Recchia (UNIPD)

Dr. Brett Vern Carlson (ITA)

Dr. Luis Fernando Cristancho Mejia (UNAL)

Dr. Calin Alexandru Ur (IFIN-HH)

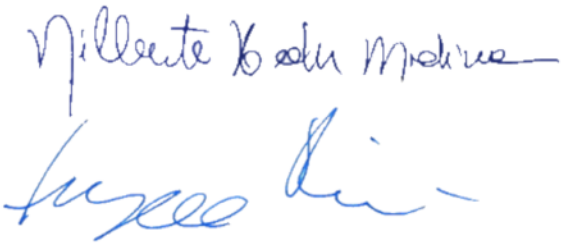

São Paulo

2023

FICHA CATALOGRÁFICA
Preparada pelo Serviço de Biblioteca e Informação
do Instituto de Física da Universidade de São Paulo

Escudeiro, Rafael

Vidas-médias de estados excitados em núcleos espelho nos orbitais fp / Excited state lifetimes in the fp - shell mirror nuclei São Paulo, 2022.

Tese (Doutorado) – Universidade de São Paulo. Instituto de Física. Depto. de Física Nuclear

Orientador: Prof. Dr. Nilberto Heder Medina

Área de Concentração: Física

Unitermos: 1. Física nuclear: 2. Estrutura nuclear; 3. Espectroscopia de raio gama.

USP/IF/SBI-88/2022

Universidade de São Paulo

Università degli Studi di Padova

Vidas-médias de estados excitados em núcleos espelho nos orbitais fp

Rafael Escudeiro

Orientadores: Nilberto Heder Medina

Francesco Recchia

Tese de doutorado apresentada ao Instituto de Física da Universidade de São Paulo para a obtenção do título de Doutor em Ciências, em convênio de dupla titulação com a Università degli Studi di Padova.

Instituto de Física - USP

Presidente da Comissão de Pós-Graduação: Prof. Dr. Luis R. W. Abramo

Dipartimento di Fisica e Astronomia "G. Galilei" - UNIPD

Coordenador do Curso de Doutorado: Prof. Giulio Monaco

Banca Examinadora:

Dr. Nilberto Heder Medina (IFUSP)

Dr. Francesco Recchia (UNIPD)

Dr. Brett Vern Carlson (ITA)

Dr. Luis Fernando Cristancho Mejia (UNAL)

Dr. Calin Alexandru Ur (IFIN-HH)

São Paulo

2023

Universidade de São Paulo

Università degli Studi di Padova

Vita media degli stati eccitati nei nuclei speculari nella fp shell

Rafael Escudeiro

Supervisori: Nilberto Heder Medina

Francesco Recchia

Tesi di dottorato presentata all'Instituto de Fisica dell'Universidade de São Paulo per conseguimento del titolo di Dottore in Ricerca, in accordo di doppia titolazione con l'Università degli Studi di Padova.

Instituto de Física - USP

Presidente del Comitato Post-Laurea: Prof. Dr. Luis R. W. Abramo

Dipartimento di Fisica e Astronomia "G. Galilei" - UNIPD

Coordinatore del Corso di Dottorato: Prof. Giulio Monaco

Commissione:

Dr. Nilberto Heder Medina (IFUSP)

Dr. Francesco Recchia (UNIPD)

Dr. Brett Vern Carlson (ITA)

Dr. Luis Fernando Cristancho Mejia (UNAL)

Dr. Calin Alexandru Ur (IFIN-HH)

São Paulo

2023

Agradecimentos

Meus agradecimentos:

Aos meus pais, Tânia e Carlos, por financiarem a pesquisa científica brasileira. Aos meus irmãos, Larissa e João, por existirem.

Aos meus orientadores, Medina e Francesco, que possibilitaram o desenvolvimento deste trabalho, sendo sempre compreensivos e dispostos a ajudar. Ao Zero pelo curso de física nuclear. À Silvia pela ajuda com o Shell Model e discussões.

Aos meus amigos do tempo de graduação pelos bons momentos nos nossos raros encontros. Aos amigos do DFN, Alessandro, Daniel, Erick, Greiciane, Osvaldo, Paula, Saulo, Valdir e Vitor pela ajuda nas disciplinas cursadas e no desenvolvimento deste trabalho, sanando ou aumentando as dúvidas. Aos amigos de infância e aos cria da rua 4 pelos momentos bons e conversas sobre outros assuntos não relacionados à física. À Capes pelas bolsas de estudo (proc. n. 88887.369950 / 2019-00 - 88887.571093 / 2020-00 - 88882.332873 / 2019-01), ao INFN-PD, à FAPESP (proc. n. 2019 / 07767-1) e ao INCT-FNA (proc. n. 464898/2014-5).

Agli amici e colleghi del Dipartimento di Fisica Galileo Galilei, Guanxin, Jaime, Jeongsu Ha, Kseniia, Pablo, S. Carollo and S. Pigliapoco. Ai amici e colleghi dei Laboratori Nazionali di Legnaro. A Denise Piatti per avermi insegnato la lingua Italiana attraverso il rivoluzionario metodo dell'alto rapporto segnale/rumore.

To my fellow Ducceschians, Antonio Jorquera, Elif, Gagandeep, Hari, Kannan, Luciana, Paula Arrías, Sukannya, Sumanta, and Vahab for all the good moments and goodbye parties, and to all of those who contributed directly or indirectly for the development of this work.

This study was financed by the Coordenação de Aperfeiçoamento de Pessoal de Nível Superior - Brasil (CAPES) - Finance Code 001.

Rafael Escudeiro

March, 2023

Abstract

Experimental and theoretical studies on nuclear structure aim to describe the observed phenomenology of the atomic nucleus. One of the most useful theoretical tools for the description of nuclear structure is the symmetry between protons and neutrons under the action of the nuclear force. From this symmetry arises the isospin formalism, which describes protons and neutrons as two states of the same particle, the nucleon. Conservation and breaking effects of the so-called isospin symmetry allowed the explanation of several nuclear phenomena and provided a powerful probe for the study of the nuclear force. Mirror nuclei are nuclei that have the number of protons and neutrons exchanged, resulting in an almost identical level scheme for the pair reflecting the similarities in the underlying structure. The measurement of the differences in excitation energy between isospin analogue states could advance the understanding about the structure of nuclei. Transition probabilities of mirror nuclei are, as well, an important instrument to understand how protons and neutrons contribute to the collective behavior of nuclei.

In this work, two experiments are reported for the study of isospin symmetries by comparing lifetimes of excited states in nuclei in the mass region $A \approx 50$. The first experiment obtained the lifetimes of isospin analogue excited states in the mirror nuclei ^{47}Cr-^{47}V and ^{49}Mn-^{49}Cr and was performed in the GANIL laboratory, France. The fusion-evaporation reactions that populated excited states in these nuclei were performed using a beam of ^{36}Ar with 115 MeV bombarding a target of 0.55 mg/cm^2 CaO with a gold backing of 10 mg/cm^2. The particles emitted during evaporation were detected with the ancillary detectors DIAMANT, *NEutron Detector Array - NEDA*, and Neutron Wall. The gamma rays depopulating the excited states in these nuclei were detected using the Advanced GAmma Tracking Array - AGATA apparatus.

The second experiment obtained the lifetime of the 6^+ state of the ^{54}Ni nucleus and was performed at the RIKEN *Nishina Center* laboratory, Japan. In order to populate low spin states in the ^{54}Ni nucleus, a neutron knockout

reaction of an exotic beam of ^{55}Ni on a 6 mm thickness target of ^{9}Be was performed. The ^{55}Ni beam was produced through the fragmentation of a ^{78}Kr primary beam with 345 MeV/u on a production target, consisting in a 7 mm thickness of ^{9}Be. The ^{55}Ni beam was separated and selected in the BigRIPS fragment separator using the TOF-Bρ-ΔE method. The detection of gamma rays depopulating the excited states of ^{54}Ni was performed by the Detector Array for Low-Intensity radiation DALI2+ and the identification of the ^{54}Ni produced in the reaction was performed by the ZeroDegree spectrometer.

The structure of the nuclei studied in this work was interpreted by comparison to the Large Scale Shell Model with the use of the ANTOINE code and the effective interaction KB3G, which allows the interaction of nucleons in the full fp space and includes the effects of the Coulomb interaction. From the comparison of experimental data and Large Scale Shell Model calculations, it was possible to obtain a value for the effective charges of protons and neutrons.

Keywords: nuclear physics; nuclear structure; nuclear excited states; gamma-ray spectroscopy; lifetime; gamma-ray spectrometers; AGATA; DALI2+; particle detectors; fusion evaporation reactions; knockout reactions; nuclear shell model.

Resumo

Os estudos experimentais e teóricos sobre a estrutura nuclear visam descrever a fenomenologia observada do núcleo atômico. Um dos instrumentos teóricos mais úteis para a descrição da estrutura nuclear é a simetria entre prótons e nêutrons sob a ação da força nuclear. Dessa simetria surge o formalismo de isospin, que descreve prótons e nêutrons como dois estados da mesma partícula, o núcleon. Os efeitos de conservação e quebra da chamada simetria de isospin permitiram a explicação de vários fenômenos nucleares e forneceram uma poderosa ponta de prova para o estudo da força nuclear. Os núcleos-espelho são núcleos que têm o número de prótons e nêutrons trocados, resultando num esquema de nível quase idêntico para o par, refletindo as semelhanças na estrutura subjacente. A medição das diferenças de energia de excitação entre estados análogos de isospin pode ajudar no entendimento da estrutura dos núcleos. As probabilidades de transição dos núcleos-espelho são também um instrumento importante para compreender como os prótons e os nêutrons contribuem para o comportamento coletivo dos núcleos.

Neste trabalho, são descritos dois experimentos para o estudo das simetrias de isospin através da comparação de vidas de estados excitados em núcleos na região de massa $A \approx 50$. O primeiro experimento obteve as vidas-médias dos estados excitados análogos nos núcleos-espelho ^{47}Cr - ^{47}V e ^{49}Mn - ^{49}Cr, e foi realizado no laboratório GANIL, França. As reações de fusão-evaporação que popularam estados excitados nesses núcleos foram realizadas usando um feixe de ^{36}Ar com 115 MeV de energia, bombardeando um alvo de 0,55 mg/cm^2 de CaO com um *backing* de ouro de 10 mg/cm^2. As partículas emitidas durante a evaporação foram detectadas com os detectores ancilares DIAMANT, *NEutron Detector Array - NEDA*, e *Neutron Wall*. Os raios gama que depopulam os estados excitados nesses núcleos foram detectados utilizando o espectrômetro *Advanced GAmma Tracking Array* - AGATA.

O segundo experimento obteve a vida-média do estado 6^+ do núcleo ^{54}Ni e foi realizado no laboratório RIKEN *Nishina Center*, Japão. Para popular estados de baixo spin no núcleo ^{54}Ni foi realizada uma reação de *neutron*

knockout de um feixe exótico de ^{55}Ni sobre um alvo de espessura de ^{9}Be de 6 mm. O feixe ^{55}Ni foi produzido através da fragmentação de um feixe primário de ^{78}Kr com 345 MeV/u sobre um alvo de produção, consistindo num alvo de 7 mm de espessura de feito de ^{9}Be. O feixe ^{55}Ni foi separado e selecionado no separador de fragmentos BigRIPS usando o método TOF-Bρ-ΔE. A detecção dos raios gama depopulando os estados excitados do ^{54}Ni foi realizada pelo *Detector Array for Low-Intensity radiation* - DALI2+ e a identificação dos ^{54}Ni produzidos na reação foi realizada pelo espectrômetro ZeroDegree.

A estrutura dos núcleos estudados neste trabalho foi interpretada pela comparação com o Modelo de Camadas com a utilização do código ANTOINE e a interação efetiva KB3G, que permite a interação dos núcleons na camada fp e inclui os efeitos da interação Coulombiana. A partir da comparação entre os dados experimentais e os cálculos do Modelo de Camadas, foi possível obter um valor para as cargas efetivas de prótons e nêutrons.

Palavras-chave: física nuclear; estrutura nuclear; estados nucleares excitados; espectroscopia de raios gama; vida-média; espectrômetros de raios gamma; AGATA; DALI2+; detectores de partículas; reações de fusão evaporação; reações de *knockout* ; modelo de camadas nuclear.

Riassunto

Gli studi sperimentali e teorici sulla struttura nucleare provano a descrivere la fenomenologia osservata del nucleo atomico. Uno degli strumenti teorici più utili per la descrizione della struttura nucleare è la simmetria tra protoni e neutroni sotto l'azione della forza nucleare. Da questa simmetria nasce il formalismo di isospin, che descrive protoni e neutroni come due stati della stessa particella, il nucleone. Gli effetti di conservazione e rottura della cosiddetta simmetria di isospin hanno permesso di spiegare diversi fenomeni nucleari e hanno fornito un potente strumento per lo studio della forza nucleare. I nuclei specchio sono nuclei in cui il numero di protoni e neutroni viene scambiato, dando luogo a uno schema di livelli quasi identico per la coppia, che riflette le somiglianze nella struttura sottostante. La misura delle differenze di energia di eccitazione tra gli stati analoghi potrebbe far progredire la comprensione della struttura dei nuclei. Le probabilità di transizione dei nuclei specchio sono, inoltre, uno strumento importante per capire come protoni e neutroni contribuiscono al comportamento collettivo dei nuclei.

In questo lavoro vengono presentati due esperimenti per lo studio delle simmetrie di isospin, confrontando i tempi di vita degli stati eccitati nei nuclei nella regione di massa $A \approx 50$. Il primo esperimento ha ottenuto i tempi di vita di stati eccitati analoghi nei nuclei specchio ^{47}Cr - ^{47}V e ^{49}Mn - ^{49}Cr ed è stato eseguito a GANIL, in Francia. Le reazioni di fusione-evaporazione che hanno popolato gli stati eccitati di questi nuclei sono state eseguite utilizzando un fascio di ^{36}Ar con 115 MeV che bombarda un bersaglio di 0,55 mg/cm^2 CaO con un supporto d'oro di 10 mg/cm^2. Le particelle emesse durante l'evaporazione sono state rilevate con i rivelatori accessori DIAMANT, *NEutron Detector Array - NEDA* e *Neutron Wall*. I raggi gamma che depopolano gli stati eccitati di questi nuclei sono stati rilevati con l'apparato *Advanced GAmma Tracking Array* - AGATA.

Il secondo esperimento ha ottenuto il tempo di vita dello stato 6^+ del nucleo ^{54}Ni ed è stato eseguito presso il RIKEN *Nishina Center*, in Giappone. Per popolare gli stati a basso spin del nucleo di ^{54}Ni, è stata eseguita una

reazione di *neutron knockout* di un fascio esotico di ^{55}Ni su un bersaglio di ^{9}Be dello spessore di 6 mm. Il fascio di ^{55}Ni è stato prodotto attraverso la frammentazione di un fascio primario di ^{78}Kr con 345 MeV/u su un bersaglio, costituito da uno spessore di ^{9}Be di 7 mm. Il fascio di ^{55}Ni è stato separato e selezionato nel *fragment separator* BigRIPS utilizzando il metodo TOF-Bρ-ΔE. La rivelazione dei raggi gamma che diseccitano gli stati eccitati di ^{54}Ni è stata effettuata dal Detector Array for Low-Intensity radiation DALI2+ e l'identificazione del ^{54}Ni prodotto nella reazione è stata effettuata dallo spettrometro ZeroDegree.

La struttura dei nuclei studiati in questo lavoro è stata interpretata attraverso il confronto con il Large Scale Shell Model con l'uso del codice ANTOINE e dell'interazione efficace KB3G, che permette l'interazione dei nucleoni nell'intero spazio fp e include gli effetti dell'interazione Coulombiana. Dal confronto tra i dati sperimentali e i calcoli del Large Scale Shell Model, è stato possibile ottenere un valore per le cariche efficaci di protoni e neutroni.

Parole chiave: fisica nucleare; struttura nucleare; stati eccitati nucleari; spettroscopia di raggi gamma; vita media; spettrometri di raggi gamma; AGATA; DALI2+; rivelatori di particelle; reazioni di fusione evaporazione; reazioni da *knockout*; modello nucleare a *shell*.

Summary

List of Figures

List of Tables

Chapter 1

Introduction

Symmetries have ever fascinated human minds; the ancient Greeks, for instance, related symmetries to harmony, beauty, and unity, and they played a decisive role in their theories about Nature [1]. Many centuries after the Greeks, Kepler applied his symmetry notions to the planetary movement. The equivalence of inertial reference frames implied by Newton's laws of mechanics was yet another example of the role of symmetries in physics. However, the acknowledgment of the role of symmetries in physical theories is much more recent, dating back to the 20^{th} century, when a series of theoretical enhancements set the symmetries as an important principle for physical laws. In classical mechanics, the symmetry principles are related to conservation laws, like momentum and energy conservation. In quantum mechanics, the consequences went further, becoming, in fact, a fundamental framework for the understanding of the phenomena characterizing the microscopic scale.

Nuclear structure studies aim to describe the observed phenomenology of atomic nuclei, exploiting symmetries and systematic studies to uncover the regular patterns that emerge from the experimental investigation. Phenomena like nuclear deformation, shape evolution and collectivity drive the nuclear models. Remarkable success has been achieved by the nuclear Large Scale Shell Model for the A = 40 - 60 mass region, being capable of reproducing in great detail the level schemes and even the electromagnetic properties of the excited states. The knowledge of the electromagnetic properties of the excited states allows one to study nuclear shape evolution, deformation, and changes in the internal nuclear structure. Gamma-ray spectroscopy can pro-

vide experimental information about the nuclear states such as the excitation energy of the levels, parity, spin and angular momentum, and level lifetimes.

1.1 Isospin Symmetry - General Overview

The existence of an approximate exchange symmetry between neutrons and protons is one of the most basic and fundamental observation that allow a description of the atomic nucleus[2]. After the discovery of the neutron by James Chadwick in 1932 [3], Heisenberg, Iwanenko and Majorana [4, 5, 6] proposed an attractive force between protons and neutrons which could balance the Coulomb repulsion, and which affect neutrons and protons in a nearly identical way. The development of these ideas led to the description of protons and neutrons as two states of the same particle, the nucleon, with the introduction of a new quantum number, the isotopic spin, later called isospin. From the mathematical point of view, the isospin distinguishes protons and neutrons by the value of their isospin third component and it follows angular momentum algebra [7]. The nucleon carries isospin $t = \frac{1}{2}$ and the labeling convention widely adopted in nuclear physics is:

$$p = \left| \frac{1}{2} \; -\frac{1}{2} \right\rangle \quad \text{and} \quad n = \left| \frac{1}{2} \; +\frac{1}{2} \right\rangle \tag{1.1}$$

This formal description of protons and neutrons as two states of the same particle requires two fundamental assumptions over the nuclear interaction, charge symmetry and charge independence. The charge symmetry requires that the proton-proton interaction (V_{pp}) is equal to the neutron-neutron interaction (V_{nn}), while charge independence requires $(V_{pp} + V_{nn})/2 = V_{np}$ [7, 8]. These conditions are known to be good approximations for the effective nucleon-nucleon interaction inside the nuclear medium. However, such symmetries are slightly broken by the difference in proton-neutron mass and by isospin non-conserving forces such as the Coulomb one. Therefore, studying isospin symmetry conservation and breaking effects can reveal details about the nuclear interaction and vice versa. Isospin non-conserving interac-

tions can be used to infer nuclear structure information from experimentally observed symmetry breaking. The nuclei located near the N = Z line are particularly suitable for studying isospin symmetry breaking effects. The case of mirror nuclei, which are nuclei with the number of protons and neutrons interchanged, is even more special, as the number of pp interactions in one nucleus equals the number of nn interactions in the other, it is possible to directly study the charge symmetry of the nuclear interaction[8].

A widely adopted tool to study isospin symmetry conservation and breaking effects is the Coulomb Energy Differences (CED), defined as the differences in excitation energy between the excited Isobaric Analogue States (IAS). A set of states with the same isospin, T, for nuclei with the same mass number are termed IAS. The CED has been used for studying isospin symmetry-breaking phenomena and understanding a series of nuclear phenomena from the microscopic point of view. Coulomb energy differences are called Mirror Energy Differences (MED) for mirror nuclei. The reduced transition probabilities ($B(E\lambda)$ and $B(M\lambda)$) are also a tool for isospin symmetry-breaking effects, and they are directly related to the excited state's lifetimes.

The study of the nuclear deformation for nuclei between ^{40}Ca and ^{56}Ni, dominated by the $f_{7/2}$ proton and neutron shell, has historically played a fundamental role in developing the understanding of nuclear structure. Mirror symmetry has been exploited in this region to highlight the microscopic mechanism it plays in constructing spin along the yrast line of these nuclei. Studies of isospin symmetry, shape change, radius change, and microscopic configuration resulted in a consistent description of this portion of the nuclear chart. Although excitation energies have been measured and compared for yrast bands between mirror nuclei, the information on the evolution of quadrupole collectivity regarding spin is still limited as a consequence of experimental constrains. In the following, some fp shell isobaric multiplets are discussed alongside the ones under study in the present work.

1.2 Work Motivation

A recent study in this mass region with the A = 46 isobaric triplet ^{46}Cr-^{46}V-^{46}Ti has tested isospin symmetry laws for transition probabilities [9]. All triplet members were populated in the same fragmentation reaction to minimize systematic errors. The lifetime of the 2^+ states of each member of the pair has been measured using the so-called "stretched target" technique. The $B(E2)$ values followed a linear trend in T_z, as expected, and presented a dominant isoscalar character.

Using MED, Cameron and collaborators studied the mirror pair ^{47}Cr - ^{47}V, where no substantial deviation from isospin symmetry was found [10]. Brandolini later revised this pair in 2009 [11] where shell model calculations considering Coulomb interaction were able to reproduce the observed MED. The lifetime of three excited states in the ^{47}Cr was determined by D. Tonev et al. using Doppler Shift Attenuation Method [12]. This mirror pair is being revisited in the present work to evaluate the lifetime of excited states of the ^{47}Cr. To minimize systematic errors and crosscheck the method, the well-known lifetimes of excited states of its mirror, ^{47}V, will also be measured.

Mirror energy differences in the mirror pair ^{49}Mn - ^{49}Cr were first studied in 1990 by Cameron et al., in which the mirror symmetries up to $J^\pi = 19/2^-$ were studied [13, 14]. In this study, the authors related the energy differences of the IAS to the different nucleon alignments. When this mirror pair was revisited by O'Leary et al. in 1997, the mirror symmetry was studied up to their band termination at $J^\pi = 31/2^-$ [15]. It was demonstrated how the nuclei generate their angular momentum, from collective rotational motion to a full alignment of the angular momentum vectors of the valence nucleons. In 2015, Bentley and collaborators [8] used this and other fp shell mirror pairs to determine the J dependency of the isospin non-conserving matrix elements. However, their study pointed to missing electromagnetic contributions in the model leading to a failure in reproducing the J dependency [8]. This mirror pair is being revisited in the present work to determine the lifetime of four excited states of the ^{49}Mn for the first time. The well-known lifetimes of

the IAS in the ^{49}Cr were also measured to minimize systematic errors and crosscheck the method.

The CED in the $A = 50$ mirror pair $T = 1$ ^{50}Fe-^{50}Cr were studied by Lenzi et al [16]. Shell model calculations were able to reproduce experimental data when considering Coulomb multipole and radial correction terms. This study also explained that the observed backbending is due to an alignment mechanism in odd-mass $f_{7/2}$-shell nuclei, as it becomes energetically favorable for the nucleons to couple in pairs of particles to maximum angular momentum [16].

In a recent study of the A = 54 isobaric triplet ^{54}Ni-^{54}Co-^{54}Fe, the mirror transitions of the $T_z = -1$ and $T_z = 1$, ^{54}Ni and ^{54}Fe, were explored with Shell Model calculations in the fp space aiming to reproduce known experimental data [17]. The authors successfully reproduced the observed MED by including a Coulomb multipole term, a Coulomb single-particle modification, a spin-orbit term, and an Isospin breaking term of 100 keV. The results allowed Rudolf and collaborators [17] to give an approximated prediction for the lifetime of the 6^+ excited state of the ^{54}Ni of about $\tau \approx 1.5$ ns. The ^{54}Ni nucleus is being revisited in the present work to determine for the first time the 6^+ excited state's lifetime experimentally.

This thesis work aims to determine the lifetimes of some excited states of ^{47}Cr, ^{49}Mn, and ^{54}Ni, and to compare the obtained transition probabilities with their respective mirror nuclei. The results will be evaluated and interpreted with shell-model calculations. Two different experiments were performed for this work. One experiment was performed at GANIL laboratories, France, and used low-energy stable beam to induce a fusion-evaporation reaction. A beam of ^{36}Ar with 115 MeV bombarded a 550 μg/cm^2 CaO target with a 10 mg/cm^2 gold backing. This experiment took advantage of the gamma-ray spectrometer Advanced GAmma Tracking Array (AGATA) [18] to detect low intensity gamma-rays, supported by ancillary detectors to enhance reaction channel selection. The second experiment was performed at Riken laboratories, Japan, and used high energy exotic beams to induce

knockout reactions. The reaction was performed using a 345 MeV/u ^{78}Kr primary beam to produce the exotic secondary beam of ^{55}Ni, which was selected and tagged by the BigRIPS fragment separator [19]. The 6^+ excited state of the ^{54}Ni was populated in a one neutron-knockout reaction after the collision of the secondary beam with a 6 mm thick ^{9}Be target. The gamma-rays were detected with the DALI2+ spectrometer array [20, 21], and the ZeroDegree fragment separator [22] identified the ^{54}Ni reaction product.

Chapter 2 provides theoretical details about the structure of mirror nuclei. This chapter also presents the nuclear Shell Model (Large Scale Shell Model) used to interpret the experimental results of this work.

Chapter 3 presents the results and describes the experimental procedure to obtain the lifetime of excited states in the mirror nuclei ^{47}Cr-^{47}V, ^{49}Mn-^{49}Cr. Including a brief explanation of AGATA and its ancillary detectors, data selection, and the data analysis techniques.

Chapter 4 presents the results and describes the experimental procedure to obtain the lifetime of the 6^+ excited state in the ^{54}Ni. The description of the experimental setup BigRIPS + DALI2+ + ZeroDegree, data selection and data analysis are also provided in this chapter. The conclusions and future perspectives are discussed in chapter 5.

Chapter 2

Theoretical considerations

2.1 Nuclear Shell Model

The atomic nucleus is a quantum system composed of neutrons and protons interacting with each other, confined in a tiny volume [23]. Evidence of the shell distribution of nucleons has been observed experimentally since the 1930s. However, only in 1949 the evidence becomes overwhelming, with the works of Mayer [24] and Haxel [25]. The distribution of nucleons into shells arises in the model as a solution to the Schrödinger equation for a given interaction potential. The Shell Model considers that some nucleons do not contribute to the nuclear structure as they are restricted to inner closed shells. The nucleons in the closed shells constitute an inert core, while external nucleons, fundamental to describe low-lying states, are called valence nucleons. These calculations in their simplest implementation consist in the Independent Particle Model considers that only one nucleon outside the inert core, and its interaction with the core nucleons is given through the nuclear potential. The Large Scale Shell Model can deal with more than one valence nucleon by using two potentials, an effective potential between the valence nucleons and the inert core, and a residual potential between the valence nucleons.

2.1.1 Independent Particle Model

In 1949 Mayer and Haxel independently suggested a nuclear Shell Model structure interpretation for the atomic nucleus, based on growing experimental evidence. Among the experimental evidence that led to the proposal of this model were special properties, such as a greater abundance of certain elements in nature and larger binding energy, for nuclei with a certain amount of nucleons: 2, 8, 20, 28, 50, 82 and 126 [24]. These numbers, called magic numbers, correspond to the number of nucleons needed to obtain a closed shell. Figure 2.1 shows the energy of the first excited state for some nuclei as a function of the number of nucleons (protons on the left, neutrons on the right), where it is possible to notice that nuclei with a magic number of nucleons have energy from the first excited state higher, indicating they have more stable configurations and evidencing their shell structure. This model

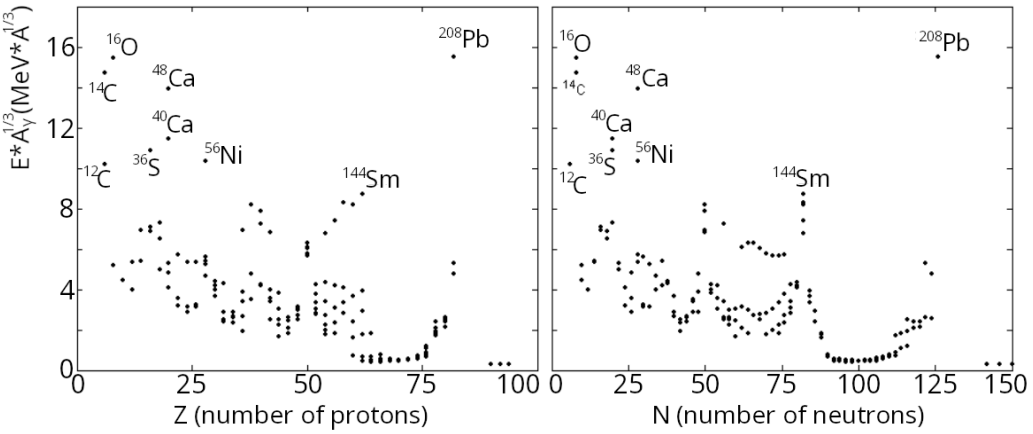

Figure 2.1: Energy of the first excited state normalized by $A^{1/3}$ for known nuclei with a lifetime greater than 10^{15} s as a function of the number of protons (Z) and the number of neutrons (N). Taken from [26].

considers that the valence nucleon interacts with an average field produced by the closed-shell nucleons, according to a given potential, in a two-body problem. An inert core is defined by nucleons in a closed shell, and valence nucleons are then defined outside the closed shell, which are responsible for the properties of the nucleus. Potentials such as square well, harmonic os-

cillator, Woods-Saxon, and others can describe to a different degree of approximation, the nuclear structure. In the classical implementation with the harmonic oscillator potential, it is necessary to add some correction terms, a surface correction term, and a strong spin-orbit interaction (equation 2.1) [24, 25] to reproduce the experimentally observed magic numbers.

$$U(r) = \frac{1}{2}\bar{h}\omega r^2 + D\vec{l}^2 + C\vec{l}\cdot\vec{s} \tag{2.1}$$

Figure 2.2 compares the magic numbers obtained by solving the Schroedinger equation for the potential of the isotropic harmonic oscillator and how the terms of surface correction ($\vec{l}^2$) and spin-orbit interaction ($\vec{l}\cdot\vec{s}$) affect them. It is possible to notice that the potential $U(r)$ (equation 2.1) can adequately describe the experimental magic numbers.

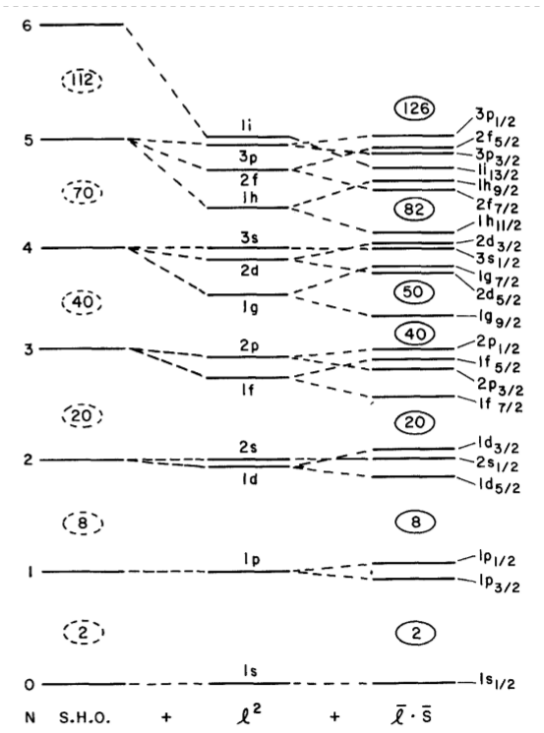

Figure 2.2: Comparison between the number of nucleons needed to complete these orbitals. The magic numbers are reproduced after the insertion of the surface term, proportional to l^2, and spin-orbit coupling, proportional to $\vec{l}\cdot\vec{s}$. Taken from [27].

As an example, the fundamental state properties of the nucleus ^{17}O can be well explained by this model since this nucleus has only one valence nucleon. In Figure 2.3 a schematic representation of the nucleons in the shells s, p, and d is shown. The valence neutron occupying the $1d_{5/2}$ orbital defines the spin and parity of the ground state ^{17}O, $J^{\pi} = \frac{5}{2}^{+}$ [1]. However, this simple model is limited to describing a few excited states in a small group of nuclei with only one valence nucleon.

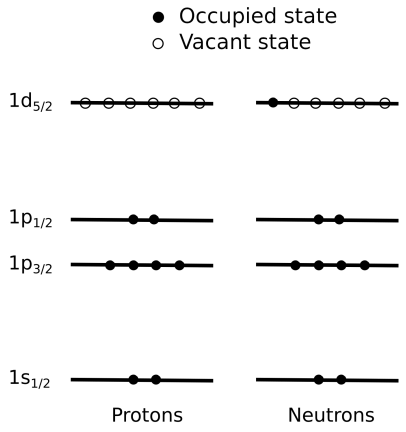

Figure 2.3: Schematic representation of the occupancy of the levels of ^{17}O ground state. The closed shell of protons does not contribute to this nucleus's structure; the properties of the ground state are mainly determined by the unpaired neutron. Adapted from[28].

2.1.2 Large Scale Shell Model

A more sophisticated description that can reproduce the structure of a broad variety of nuclei is provided by the Large Scale Shell Model, in which several nucleons are considered in the valence space. This is possible because the nuclear interaction is divided into two parts: an interaction between the valence nucleons and the average field produced by the inert core (H)

[1] J is total angular momentum ($\vec{J} = \vec{l} + \vec{s}$) and the parity is defined as $\pi = (-1)^l$.

and an interaction between the valence nucleons themselves called residual interaction (H_{res}) [29]. Equation 2.2 shows the Hamiltonian of the effective interaction of the problem.

$$\tilde{H} = H + H_{res} \tag{2.2}$$

To solve the many-body quantum problem, the unperturbed Hamiltonian is solved as in the independent particle model, and then the residual potential is treated as a perturbation to the system. The equation for the k-th nucleon with eigenfunction ϕ_k and energy e_k can be written as:

$$h\phi_k(r_i) = e_k\phi_k(r_i) \tag{2.3}$$

where r_i is the notation for all coordinates of the k-th nucleon. Since the ϕ_k functions are the eigenfunctions of individual Hamiltonians, the nuclear state wave function with A nucleons can then be written as:

$$\Psi_{1,...,A}(r_1, ..., r_A) = \prod_{k=1}^{A} \phi_k(r_i) \tag{2.4}$$

with energy:

$$E = \sum_{k=1}^{A} e_k \tag{2.5}$$

The eigenfunctions and eigenvalues (energies) for the perturbed Hamiltonian are calculated, diagonalizing $\tilde{H}$ on the basis of the $\Psi_{1,...A}(r_1, ..., r_A)$, that is, solve the equation for the effective interaction 2.6.

$$\tilde{H}\Psi_{1,...A}(r_1, ..., r_A) = \tilde{E}\Psi_{1,...A}(r_1, ..., r_A) \tag{2.6}$$

Equation 2.6 leads to a set of linear equations. When the number of valence nucleons is large, the solution to this problem requires great computational power and a specific algorithm that makes solving the problem a time-demanding job. In this work, the code ANTOINE [30, 31] was used for

the diagonalization of the operator $\tilde{H}$ of the equation 2.6.

Given this theoretical framework, the choice of the number of valence nucleons, active shells, and residual interaction, must be carefully handled, taking into account the problem to be solved and the region of mass of the nucleus of interest. According to [30, 29] it is necessary to construct an effective interaction for the problem, which is performed by comparison to experimental data and, it is developed specifically for each configuration space [32]. An example is given by the effective interaction KB3G [33], which was developed to describe the fp shell using a ^{40}Ca core. This is the interaction used in this work to calculate the structure of the mirror pairs A = 47 and A = 49. A modified version of this interaction optimized for nuclei in the upper part of the fp shell was used to calculate the structure of the ^{54}Ni [34].

2.2 Mirror nuclei

Differences in excitation energies between Isobaric Analog States (IAS) have been studied using the shell model with very good accuracy for nuclei lying in the $f_{7/2}$ shell and allowed isospin symmetry-breaking effects of multiple origins to be investigated. The symmetry between neutrons and protons in the nuclear interaction can be broken by any isospin non-conserving term. The Coulomb interaction accounts for the largest of those effects because the repulsion between protons diminishes the binding energy of a nuclear state with respect to its lower-Z counterpart [2]. The total binding energy difference is called Coulomb displacement energy (CDE), and for any two pairs of an isobaric multiplet in an exchange of k protons for neutrons, it can be expressed as:

$$CDE(T, T_z) = M_{T,T_z} - M_{T,T_z+k} + k\Delta_{nH} \tag{2.7}$$

where M is the atomic mass, Δ_{nH} is the neutron-hydrogen atomic mass difference, and T_z is the isospin projection for the larger-Z isobar. A charge-violating interaction, such as the Coulomb one, will lift the degeneracy of a set of IAS and can be treated as a perturbation if the energy difference is

small compared to the binding energy due to the nuclear force [2].

An equation aiming to understand the dependence of the binding energy with T_z was introduced by Wigner [35] in 1957, the Isobaric Multiplet Mass Equation (IMME). In the absence of charge-violating terms, the binding energy may be obtained by calculating the expected value of the charge-independent interaction:

$$BE(\alpha T T_z) = \langle \alpha T T_z \big| H_{CI} \big| \alpha T T_z \rangle \tag{2.8}$$

where H_{CI} is the charge-independent interaction, $\big|\alpha T T_z\rangle$ is the eigenstate with α accounting for all the other quantum numbers of the state. The charge-violating interaction, considering only two-body forces, can be written as a tensor of rank two:

$$H'_{CV} = \sum_{k=0}^{2} H_{CV}^{(k)} = H_{CV}^{(0)} + H_{CV}^{(1)} + H_{CV}^{(2)} \tag{2.9}$$

where $H_{CV}^{(0)}$, $H_{CV}^{(1)}$, $H_{CV}^{(2)}$ correspond to the isoscalar, isovector, and isotensor components of this interaction, respectively [2]. These components are related to the nucleon-nucleon interactions and can be expressed as:

$$\begin{aligned} H_{CV}^{(0)} &= \frac{v_{pp} + v_{nn} + v_{np}}{3} \\ H_{CV}^{(1)} &= v_{pp} - v_{nn} \\ H_{CV}^{(2)} &= v_{pp} + v_{nn} - 2v_{np} \end{aligned} \tag{2.10}$$

It is possible to observe from the equations 2.10 that the charge symmetry condition arises if the isovector component is zero, $H_{CV}^{(1)} = 0$ which implies $v_{pp} = v_{nn}$, and that the charge independence condition holds if the isotensor contribution is zero, $H_{CV}^{(2)} = 0$ which implies $v_{np} = (v_{pp} + v_{nn})/2$. However, both symmetries are slightly broken, making the IMME a tool for studying isospin symmetry-breaking phenomena. The energy difference in the isobaric

multiplet is then given by:

$$\Delta BE(\alpha TT_z) = \langle \alpha TT_z | \sum_{k=0}^{2} H_{CV}^{k} | \alpha TT_z \rangle \tag{2.11}$$

Extracting the T_z dependency explicitly with the Wigner-Eckart theorem and writing the analytical form of the remaining Wigner 3 - j symbols for the 3 values of k, the IMME equation can be written as

$$\Delta BE(\alpha TT_z) = \frac{1}{\sqrt{2T+1}} \times \left[M^{(0)} + \frac{T_z}{\sqrt{T(T+1)}} M^{(1)} + \frac{3T_z^2 - T(T+1)}{\sqrt{T(T+1)(2T+3)(2T-1)}} M^{(2)} \right] \tag{2.12}$$

where $M^{(k)}$ are the reduced matrix elements $< \alpha T | H_{CV}^{(k)} | \alpha T >$. By ordering the terms the equation 2.12 can be written as:

$$\Delta BE(\alpha TT_z) = a + bT_z + cT_z^2 \tag{2.13}$$

These components can be experimentally obtained by studying a set of IAS. In this form, the a coefficient is related to the isoscalar component, while the b and c are related only to the isovector and isotensor components, respectively. This quadratic form holds as long as higher-order perturbation effects are not needed and three-body forces contributions are not important [2]. The CDE can be directly related to IMME coefficients and can be written for any adjacent members of a multiplet as:

$$CDE(T, T_z) = -b - c(2T_z + 1) + \Delta_{nH} \tag{2.14}$$

where T_z is the isospin projection for the larger Z isobar [2, 36]. The CDE has been theoretically calculated for a wide range of IAS for which experimental data exists. Although several corrections to the 2.14 equation were performed over the years, an underestimation in the CDE value of around 7% still remains, known as the Nolen-Schiffer anomaly [37, 38].

The differences in the excitation energies between isobaric analog states are called Coulomb Energy Differences (CED). In order to calculate these energy differences, the absolute binding energies of the ground states are normalized, and the CED only accounts for the change in CDE with respect to the ground state. This procedure allows one to study how the Coulomb energy, or other charge-depended phenomena, changes as a function of excitation energy and spin J for a set of IAS. The measured CED are typically 100 keV or less and thus are very sensitive to nuclear structure properties [2, 36].

The CED for IAS in mirror nuclei are called Mirror Energy Differences (MED), and can be expressed as the difference in excitation energy as a function of the spin and can also be expressed in terms of the IMME coefficients:

$$MED_{J,T} = E^*_{J,T_z=-1/2} - E^*_{J,T_z=1/2} = \Delta b_J \tag{2.15}$$

in a pair of mirror nuclei with $T = 1/2$, where Δb_J is a variation of the b coefficient as a function of spin with respect to the ground state. For multiplets with $T = 1$, it is possible to define also the triplet energy differences TED, which yield information about the isotensor component for the charge-violating interaction.

If the electromagnetic effects are sufficiently well known, the use of MED and TED data allows the study of charge-symmetry and charge independence in the nuclear interaction [2]. The contribution of the electromagnetic effects for the MED can be summarized in a multipole term and a monopole term, responsible for accounting for the recoupling of nucleons, and radius variation with the increasing angular momentum, respectively. Shell model calculations are utilized to reproduce MED accounting for all these effects with remarkable success in the $f_{7/2}$ shell. Figure 2.4 compares experimental and shell model calculated data. It is possible to observe that the effects are due to the Coulomb multipole (C_M), Coulomb monopole (C_r), and an extra isospin non-conserving interaction (V_B) adds up to the experimentally observed value. The isospin non-conserving interaction (V_B) has isovector

and isotensor components, and its origin remains an open question.

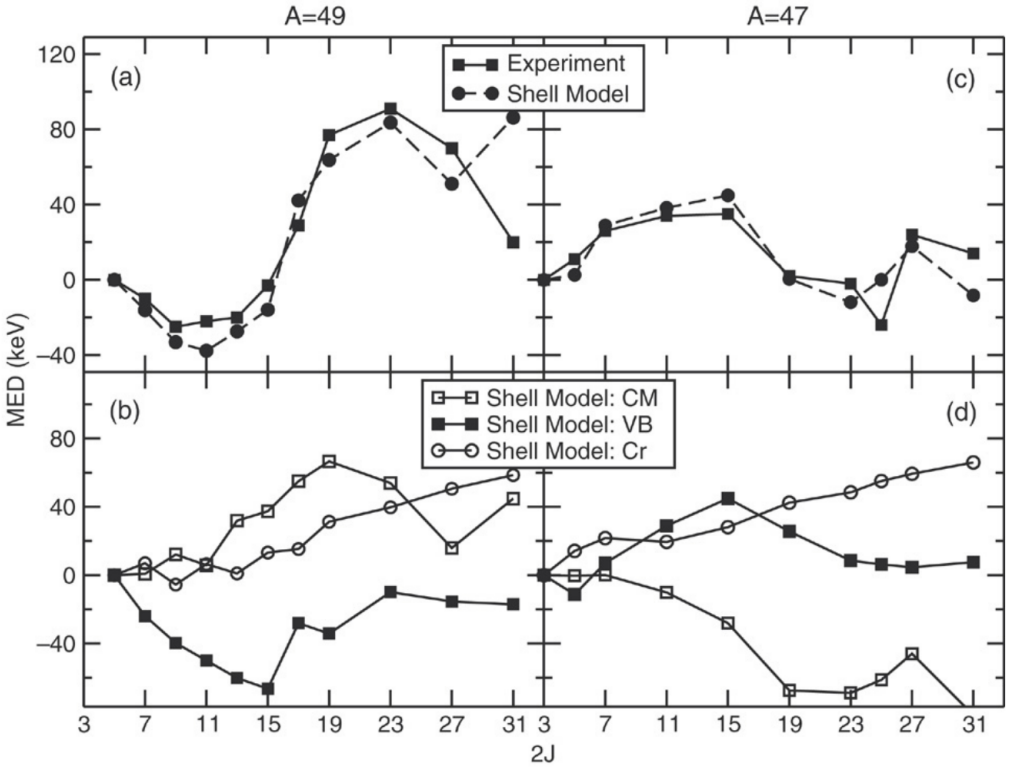

Figure 2.4: a) Experimental and calculated MED for the mirror pair ^{49}Cr-^{49}Mn. b) Shell model calculated contributions for A=49 pair. c) Experimental and calculated MED effect for the mirror pair ^{47}Cr-^{47}V. d) Shell model calculated contributions for A=47 pair. Taken from [2].

The selection rules for the electromagnetic transitions can be derived considering the constraint of isospin symmetry. The electromagnetic hamiltonian can be divided in two terms [36]:

$$\hat{H}' = \sum_k \hat{H}^{(k)} = \hat{H}^{(0)} + \hat{H}^{(1)} \tag{2.16}$$

where the 0 and 1 indexes refer to the isoscalar and isovector components. The eigenstate of the system can be represented by $|\alpha T T_z>$, where α represents all other variables not dependent on T or T_z. Then, by applying this

Hamiltonian operator to an initial state $|\alpha T^i T_z^i >$ we have:

$$\begin{aligned}\left\langle \alpha T^f T_z^f \right| \hat{H}' \left| \alpha' T^i T_z^i \right\rangle &= \left\langle \alpha T^f T_z^f \right| \hat{H}^{(0)} + \hat{H}^{(1)} \left| \alpha' T^i T_z^i \right\rangle \\ &= \Big(-1 \Big)^{T^f - T_z^f} \begin{bmatrix} T^f & 0 & T^i \\ -T_z^f & 0 & T_z^i \end{bmatrix} \left\langle \alpha T^f \middle\| \hat{H}^{(0)} \middle\| \alpha' T^i \right\rangle \\ &+ \Big(-1 \Big)^{T^f - T_z^f} \begin{bmatrix} T^f & 1 & T^i \\ -T_z^f & 0 & T_z^i \end{bmatrix} \left\langle \alpha T^f \middle\| \hat{H}^{(1)} \middle\| \alpha' T^i \right\rangle \end{aligned} \quad (2.17)$$

after the application of the Wigner-Eckhart theorem. The initial and final states of an electromagnetic transition occur inside the nucleus, which implies $T_z^f =, T_z^i = T_z$. This implies that the expression for the isoscalar matrix elements can be written as:

$$\left\langle \alpha T^f \middle\| \hat{H}^{(0)} \middle\| \alpha' T^i \right\rangle = \frac{1}{\sqrt{2T^i + 1}} \left\langle \alpha T^f T_z^f \right| \hat{H}^{(0)} \left| \alpha' T^i T_z^i \right\rangle \delta_{T^i T^f} \quad (2.18)$$

meaning that the isoscalar component is zero unless the transition is for states of the same isospin ($T \to T$). The isovector component for $T^f = T^i = T$ can be expressed as:

$$\begin{bmatrix} T^f & 1 & T^i \\ -T_z^f & 0 & T_z^i \end{bmatrix} = \Big(-1 \Big)^{T - T_z} \frac{T_z}{\sqrt{T(T+1)(2T+1)}} \quad (2.19)$$

Both equations generated the following selection rule for analogue transitions: transitions for states of different isospin have the same strength due to a vanishing isoscalar component; transitions for states of the same isospin have a non-vanishing isoscalar component. In terms of the Shell Model, the electric dipole and quadrupole operators can be expressed as [39]:

$$\hat{T}_\mu(E1) = \sum_{k=1}^{A} e_k r_\mu(k) = \frac{e}{2} \Big(\sum_{k}^{A} r_\mu(k) + 2 \sum_{1}^{A} \hat{t}_z(k) r_\mu(k) \Big) \quad (2.20)$$

$$\hat{T}_\mu(E2) = \sum_{k=1}^{A} e_k r_\mu^2(k) = \frac{e_\nu + e_\pi}{2} \hat{T}_\mu^{(0)}(E2) + \frac{e_\nu - e_\pi}{2} \hat{T}_\mu^{(1)}(E2) \quad (2.21)$$

where e_ν and e_π are the effective charges for the neutron and proton, respectively. It is possible to demonstrate [36, 40] that the $B(E1)$ for analogue transitions in mirror nuclei should have the same value under the isospin symmetry conservation assumption. The electric quadrupole operator for transitions $\Delta T = 0$ is given by:

$$\left\langle \alpha T^f T_z^f \middle| \hat{T}_\mu^{(0)}(E2) + \hat{T}_\mu^{(1)}(E2) \middle| \alpha' T^i T_z^i \right\rangle = \tag{2.22}$$
$$\frac{1}{\sqrt{2T+1}} \left\langle \alpha T \middle| \hat{T}_\mu^{(0)}(E2) \middle| \alpha' T \right\rangle + \frac{T_z}{\sqrt{T(T+1)(2T+1)}} \left\langle \alpha T \middle| \hat{T}_\mu^{(1)}(E2) \middle| \alpha' T \right\rangle$$

and shows that E2 transition elements must have a linear dependence on T_z for an isobaric multiplet [36].

The effective charges are introduced in the Shell Model description to account for the polarization effects caused by the valence nucleons on the inert core. In the absence of isospin-breaking interactions, the wave functions of analogue states in mirror nuclei are identical and thus provide a way to probe the polarization effect of the core. This effect can be accounted for by the polarization charges which are related to the effective charges according to the equation 2.23, meaning that the B(E2) values of mirror transitions are sensitive to the polarization charge [41].

$$\begin{aligned} e_\pi &= 1 + e_{pol}^{(0)} - e_{pol}^{(1)} \\ e_\nu &= e_{pol}^{(0)} + e_{pol}^{(1)} \end{aligned} \tag{2.23}$$

Where the $e_{pol}^{(0)}$ and $e_{pol}^{(1)}$ are called isoscalar and isovector polarization charges and are believed to arise from virtual excitations of isoscalar and isovector giant quadrupole resonances (GQR) of the core [41]. The GQR are high-frequency collective excitations of atomic nuclei, typically occurring in many-body quantum systems confined in a potential well, such as the case of atomic nuclei. A description of the GQR can be found in the refs [42, 43]. Following Bohr description [44], the polarization charge provided by E2 effective charges

for low-energy transitions can be calculated according to equation 2.24.

$$e_{pol} = e\Big(\frac{Z}{A} - 0.32\frac{N-Z}{A} + \Big(0.32 - 0.3\frac{N-Z}{A}\Big)\tau_z\Big) \tag{2.24}$$

Where $\tau_z = 2T$, with T being the isospin. In the equation 2.24, the terms not accompanying τ_z correspond to the isoscalar polarization charge, while terms accompanying τ_z correspond to the isovector polarization charge.

Chapter 3

Lifetime measurements in the ^{47}Cr - ^{47}V and ^{49}Mn - ^{49}Cr

The lack of experimental information regarding excited states lifetimes for the ^{47}Cr and ^{49}Mn, prevented any comparison with their mirror counterparts and further investigation of their possible features. Gamma-ray spectroscopy is the main tool to obtain experimental information about the properties of excited nuclear states and therefore study their structure. Among the nuclear properties within the scope of gamma-ray spectroscopy are the excitation energy of the levels, the transition energies, the spin, the parity, and the excited-state lifetimes.

An experiment to measure the lifetimes of excited states in the ^{47}Cr and ^{49}Mn nuclei has been performed at GANIL laboratories using a fusion-evaporation reaction, in which a 115 MeV ^{36}Ar beam bombarded a 550 μg/cm^2 CaO target with a 10 mg/cm^2 gold backing. This reaction also populated excited states in the ^{47}V and ^{49}Cr, which have a well-known structure and thus were used as benchmark tools for the data analysis techniques employed in this work. The gamma rays depopulating the produced nuclei were detected by AGATA. Further reaction channel selection was performed with the usage of neutron and charged particle detection arrays.

In the following sections, an overview of the detector types, a description of the experimental setup used in this experiment, the lifetime measurement

technique, data selection, data analysis procedure, and the experimental results are presented.

3.1 Experimental setup

3.1.1 Large Gamma-ray Detector Arrays

Combining multiple gamma-ray detectors into detector arrays was an important development for gamma-ray spectroscopy, enabling studies of nuclear structures at high spins and high multiplicity of events [45]. The first generation of those large arrays, built in the early 1980s, such as the Oak Ridge Spin Spectrometer and the Darmstadt-Heidelberg Crystal Ball, which resulted in an array with very high gamma-ray detection efficiency but, being composed of scintillator detectors, had the drawback of low energy resolution [46]. Starting from the 1970s, the advent of solid-state lithium-drifted germanium detectors and later hyper-pure germanium detectors represented a major step forward in gamma-ray spectroscopy, dramatically improving the energy resolution, leading to the construction of arrays like the Total Energy Suppression Shield Array (TESSA) [47]. The second and third-generation arrays improved the energy resolution and were introduced in the late 1980s and 1990s, with Compton-suppressed hyper-pure germanium detectors, like GASP [48, 49], EUROBALL [50, 51], and GAMASPHERE [52, 53] spectrometers. The introduction of Compton suppressed detectors is needed in view of the three most relevant interaction effects of gamma-ray with matter, photoelectric absorption, Compton scattering, and pair production. Figure 3.1 presents the case of the interaction cross-section of gamma-rays in the germanium. The interaction effect that dominates for gamma rays in the energy range of interest for nuclear physics, 200 to 2500 keV, is Compton scattering, which corresponds to a partial energy deposit of the incident photon energy into the detection medium. The large Compton scattering cross-section led to the development of anti-coincidence techniques to suppress the Compton-generated background when using germanium radiation detectors.

The Compton suppressors consist of Bismuth Germanate (BGO) scintillators

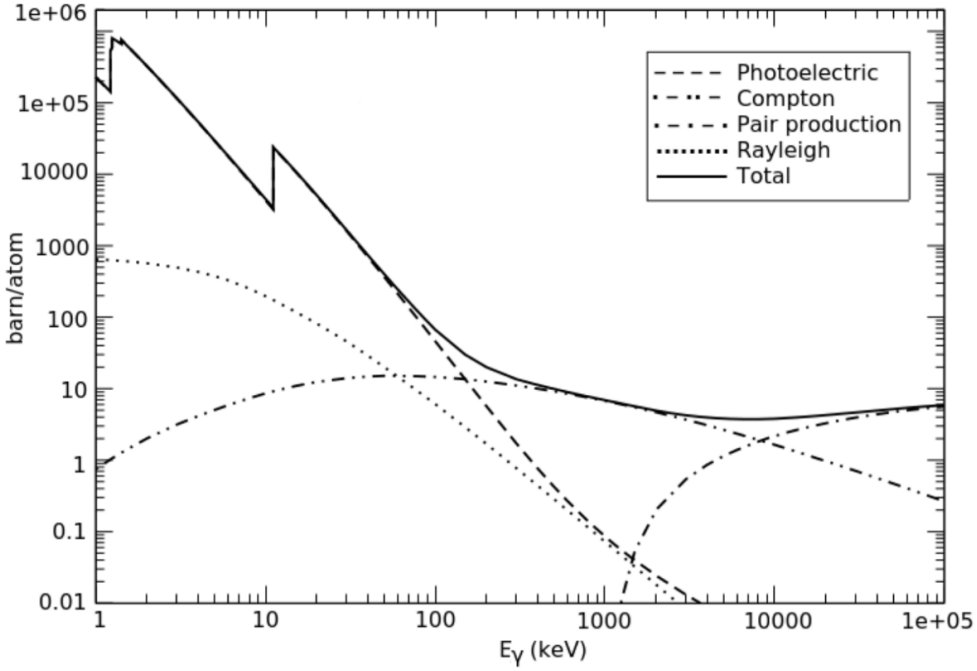

Figure 3.1: The Compton scattering, photoelectric, and pair production cross-sections for Germanium material as a function of the gamma-ray photon energy. Taken from [54].

surrounding the germanium detectors to perform anti-coincidence with the escaping Compton-scattered gamma rays. This suppression technique significantly increased the peak-to-total counting ratio in gamma-ray spectra, decreasing the continuous Compton background [50]. Those enhancements in detector arrays allowed the experimental verification of new nuclear structure discoveries such as superdeformation, shape coexistence and high-K isomers [46]. Although the Compton-suppressed arrays significantly improved the peak-to-total ratio in the gamma-ray spectra, they have an intrinsic limitation imposed by design: the presence of the Compton suppressors limits the solid angle available for the HPGe detector and reduces the array efficiency. Those limitations can be overcome by current-generation gamma-ray tracking arrays that utilize electrically segmented germanium detectors com-

bined with tracking algorithms to unfold the energy of the original incident gamma-ray.

3.1.2 Advanced GAmma Tracking Array

The Advanced GAmma Tracking Array (AGATA) spectrometer is a high-resolution and high-efficiency gamma-ray detection system developed and constructed by a wide European collaboration and designed for the needs of contemporary nuclear physics research to study nuclear structures far from the stability line. The AGATA spectrometer utilizes position-sensitive electrically segmented HPGe detectors and powerful algorithms to track the gamma rays path over successive Compton interactions within the detectors, making Compton suppressor detectors unnecessary, because the full solid angle around the target can be covered by germanium detectors. The tracking technique allows the trajectory reconstruction of the incident photons over successive interactions in the germanium material in order to determine their energy and direction [18]. The unique capabilities and features of AGATA allow it to obtain high efficiency and state-of-the-art Doppler correction capabilities, thus achieving unprecedented resolving power[1]. In Figure 3.2 the AGATA spectrometer and the previous generation detection arrays are compared.

The AGATA detectors are composed of electrically segmented coaxial n-type HPGe crystals, having three different shapes optimized to be combined into triple clusters that can be arranged in a spherical shell (figure 3.3). Each AGATA detector is divided into 36 segments. When completed, the triple clusters will cover 82% of 4π solid angle. During the experimental campaign for this work, an incomplete version of the array was utilized, composed of 12 triple clusters (36 crystals) covering almost 1π spherical shell, ranging from 110° to 160° with respect to the beam direction. Figure 3.4 shows a representation of the complete AGATA array and a picture of the array used during the experimental campaign. Each AGATA crystal provides 37

[1] to be understood as the lowest cross section accessible by the array exploiting gamma coincidences [55].

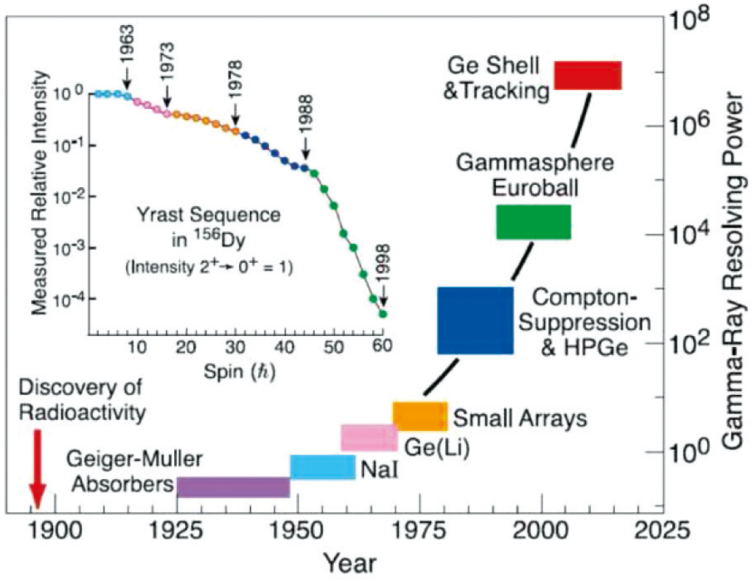

Figure 3.2: Comparison between the smallest measured yrast intensity in ^{156}Dy, for the $2^+ \rightarrow 0^+ +$ transition measured with successive generations of gamma-ray spectrometers. Indicated in red is the AGATA generation. Taken from [56].

high-resolution spectroscopic channels, 36 for the segments and one for the core, adding up to 111 for each triple cluster. As AGATA detectors must be kept at cryogenic temperatures, the triple clusters hold cryostats for the crystals and provide mechanical support for the cold and warm preamplifier electronics. The AGATA electronic system needs to handle the high count rate specifications of up to 50 kHz per crystal. A full description of the AGATA electronic system is beyond the scope of this work. For details about it, refer to [18, 57].

3.1.3 Pulse Shape Analysis

As already discussed, when a gamma ray interacts with germanium detectors, it creates charged carriers (electron-hole pairs) that must be collected by an electric field to generate the detector response pulse. As the charge carriers travel a considerable distance until collection, the leading edge of the generated pulses depends on the position at which they were formed, and, by

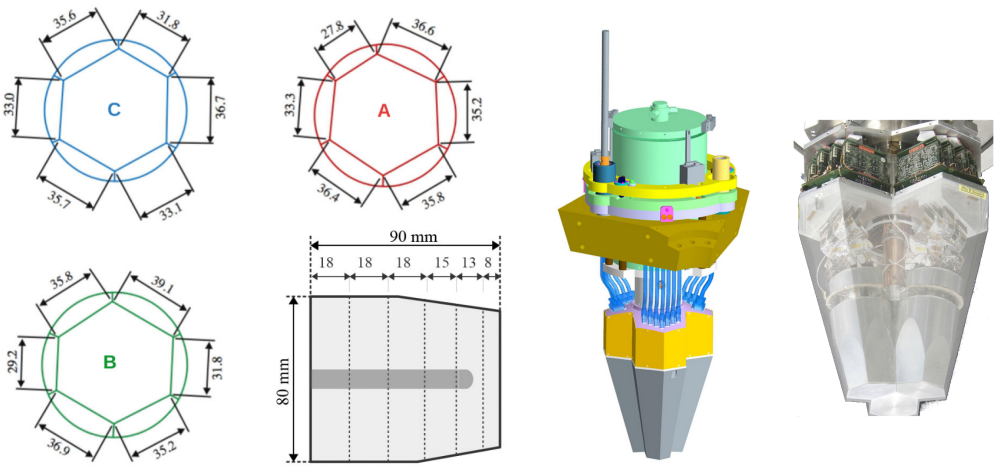

(a) AGATA crystals.

(b) AGATA triple cluster.

Figure 3.3: The three types of AGATA crystals and the crystals assembled in a triple cluster. Taken from [57].

analyzing the pulse shape, it is possible to obtain high-precision information about the interaction point position. Non-segmented coaxial germanium detectors are sensitive to the radial position of the incident gamma rays [58]. Figure 3.5 illustrates three different interaction points in a given section along the symmetry axis of a regular germanium detector, and it is possible to observe that the pulse shape is different depending on the point of interaction.

The AGATA crystals, thanks to the electric segmentation are truly position-sensitive. When an interaction occurs, it produces pulses on the segment hit by the gamma ray and in the neighboring segments. Figure 3.6 illustrates two single interaction events occurring in different segments. It is possible to observe the net current on the hit segment and some transient signals in the adjacent ones. AGATA Pulse Shape Analysis (PSA) is fast enough to be performed in real-time. It consists of an adaptive grid search, relying on the comparison between the experimental digitized signals with a reference basis in which a position is associated with each response signal. The PSA algorithm provides the three-dimensional interaction position, energy, and

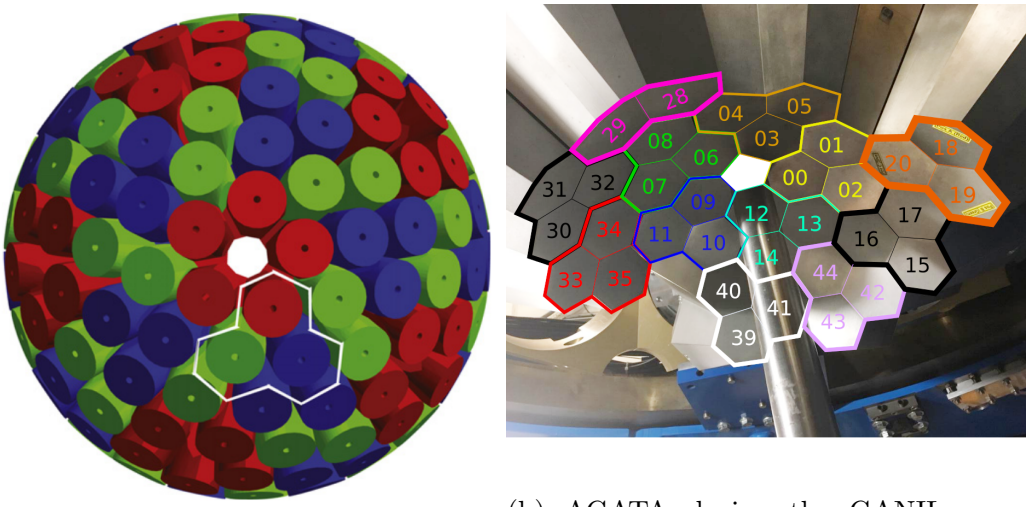

(a) Representation of AGATA 4π.

(b) AGATA during the GANIL campaign.

Figure 3.4: Graphical representation of complete AGATA and a image with the identification numbers of the crystals.

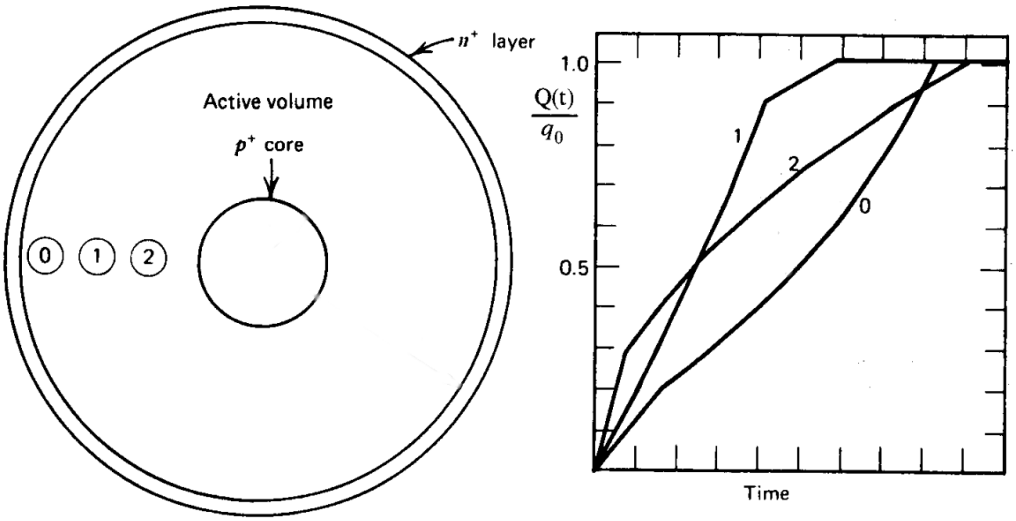

Figure 3.5: Simplified model for a non-segmented germanium detector and its different pulse shapes depending on the position of interaction. Taken and adapted from [58].

time [18].

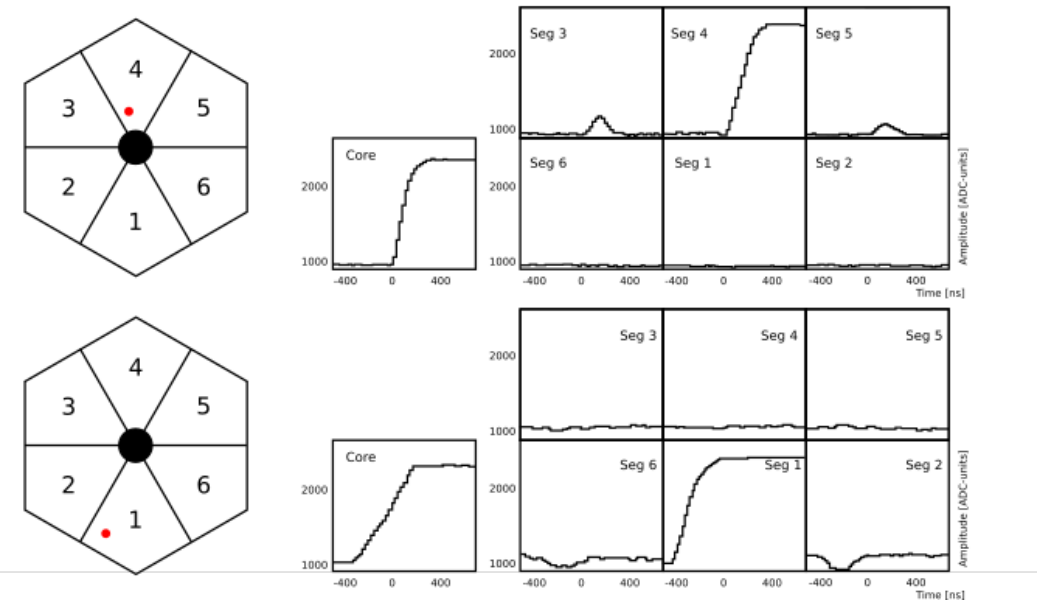

Figure 3.6: Illustration of two single interactions (red dots) happening in different segments. It is possible to see the pulse shape differences between the segments and core. Adapted from [54, 59].

3.1.4 Tracking algorithms

The main feature of the AGATA array relies on its tracking capabilities; therefore, the tracking algorithm's goal is to reconstruct the energy of the incident gamma-ray by disentangling and following the scattering sequence [54]. In order to perform gamma-ray tracking, the interaction positions and energies are assumed to be known because this is exactly what the PSA algorithm provides with a precision better than 5 mm. As discussed before, the dominant interaction effect for gamma rays in the range of 200 to 2500 keV is Compton scattering, which can be described by the equation 3.1, corresponding to momentum and energy conservation, where E'_γ is the energy of the scattered photon, E_γ is the energy of the incident gamma-ray, and θ is the angle between the direction of the photons.

$$E'_\gamma = \frac{E_\gamma}{1 + \frac{E_\gamma}{m_e c^2}(1 - cos\theta)} \tag{3.1}$$

A possible way to track the gamma rays would be simply to check which of the possible sequences within a set of points is compatible with the Compton scattering recalculated. However, this is not achievable in practice due to computational requirements [54, 59]. In order to track the gamma-ray energies, clustering [60] techniques have been developed and consist of packing together smaller sets of interaction points by checking any two points for an angular separation smaller than a given reference. Once the clusters are formed, a check for the validity of the Compton scattering formula is performed for each of the Compton vertices. Figure 3.7 presents an angular map for a simulated ideal 4π Ge shell sphere in the presence of a schematic point source emitting 1333 keV photons with a multiplicity of 30. The first interaction point of each photon is marked in blue, the other points being drawn in red if the photon is fully absorbed or in green if partly escaping [54]. Incomplete detected gamma-ray energies are discarded, making the tracking algorithms a Compton suppression technique. There are different tracking algorithms, and their development and improvement is an ongoing process [18].

3.1.5 AGATA ancillary detectors

In order to study the structure of a nucleus, in general it is necessary the construction of a partial level scheme and the measurement of key quantities like the lifetime of excited states to compare with theoretical calculations. In a nuclear reaction, many reaction channels are open. For this reason, in most practical applications, gamma-ray detectors are combined with auxiliary detectors to improve channel selectivity. Particle detectors are used to tag a determined type of particle by requiring coincidences. The evaporated charged particles were detected with DIAMANT [61, 62]. The evaporated neutrons were detected with NEutron Detector Array (NEDA) [63] and Neutron Wall [64]. Those ancillary systems in combination with AGATA were able to select events in coincidence with the desired reaction channel and allowed for the clear observation of the gamma-ray transitions from the nuclei

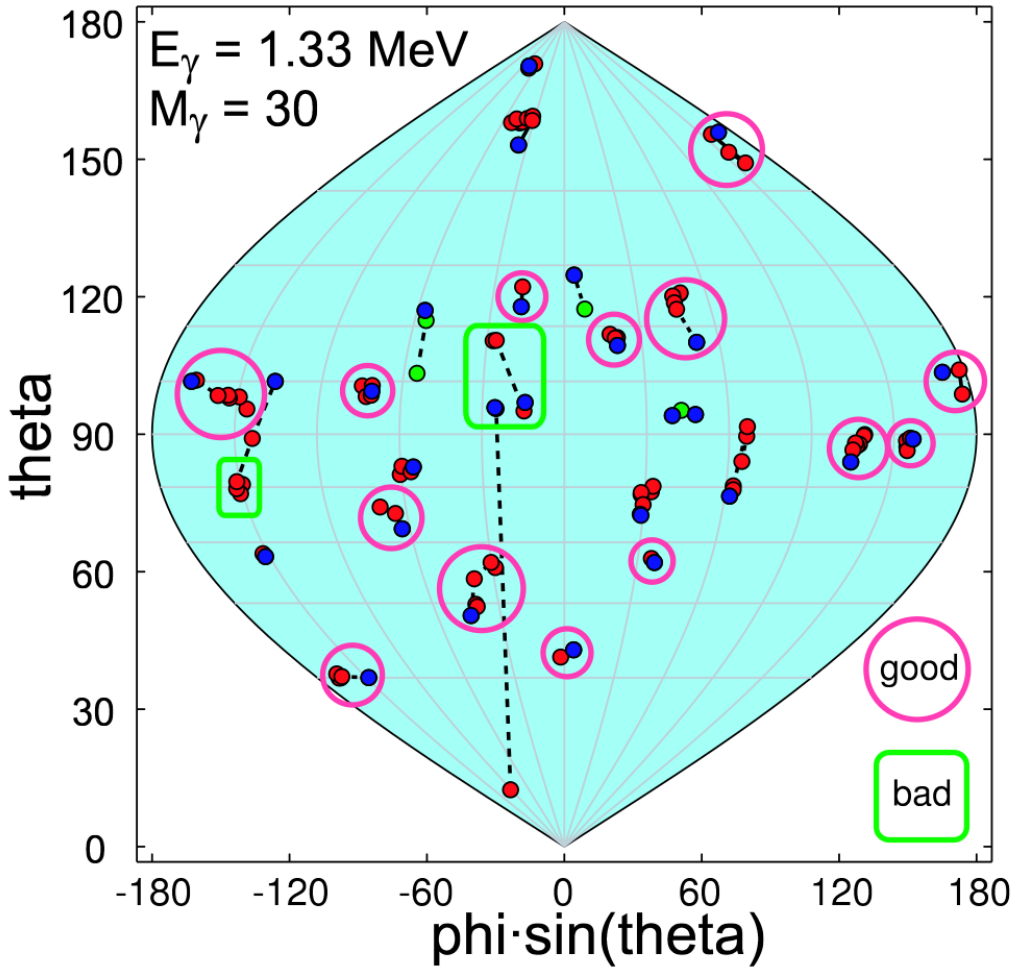

Figure 3.7: Illustration of clustering techniques. Correctly reconstructed transitions are encircled; the rectangles represent badly reconstructed events. Taken from [54].

^{47}Cr, ^{47}V, ^{49}Mn, and ^{49}Cr.

The DIAMANT is an array of CsI(Tl) scintillator detectors for light-charged particles, like protons and alpha particles, allowing the selection of these reaction channels in fusion-evaporation reactions. Each detector is made from a slab of 3 mm thick CsI(Tl) scintillation crystal, a plexiglass light guide, and a PIN photodiode. A tridimensional rendering of DIAMANT geometry can be observed in Figure 3.8.

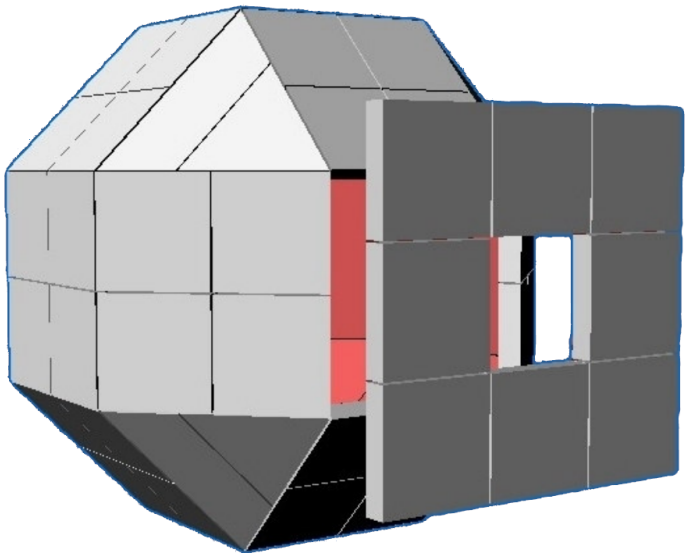

Figure 3.8: Tridimensional rendering of DIAMANT geometry. Taken from [65].

NEDA is a neutron detector array composed of liquid scintillators covering, when completed, a solid angle of 2π for neutron detection, allowing the identification of exotic neutron-deficient nuclei[63]. Each detector unit is composed of a volume of $\approx$ 3.15 l filled with the liquid organic scintillator EJ301 in a hexagonal enclosure attached to a photomultiplier tube. NEDA was designed to operate as a neutron tagging device for AGATA, selecting the neutron-related events by pulse-shape discrimination and Time-of-Flight (ToF). The Neutron Wall (NW) detectors share several similarities with NEDA detectors, including the liquid scintillator, but NW detectors are built-in cells of different sizes, and volumes [66]. The NW detectors were

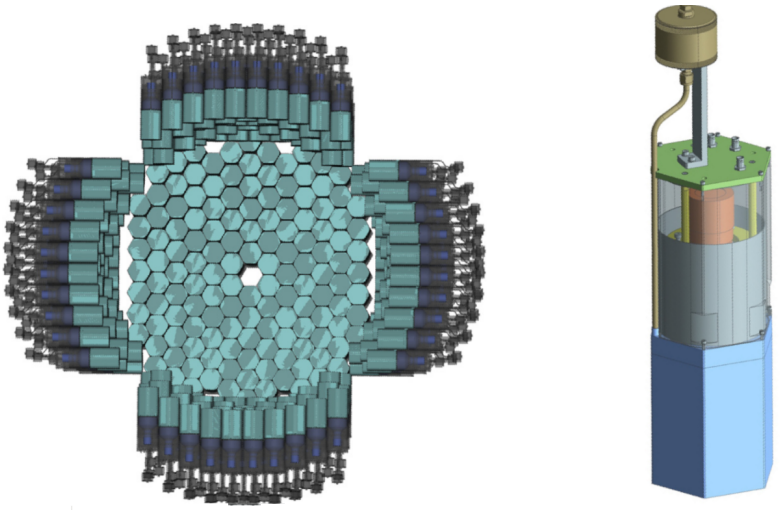

Figure 3.9: Proposed NEDA geometry for a 2π angular coverage and representation of the design of a NEDA neutron detector. Taken from [63].

arranged in a 90° ring around the target, and such a position was kinematically unfavored by the reaction. These arrays were utilized for the first time together during the AGATA-NEDA+NW-DIAMANT campaign, and their performance is discussed later in this chapter.

3.2 Lifetime Measurement Techniques

The lifetime of excited states is directly related to the reduced transition probabilities and thus is a valuable source of information about the nuclear structure. Nuclear excited states have lifetimes ranging from fraction of femtosecond to seconds, and therefore several experimental techniques have to be applied depending on the lifetime value. Figure 3.10, presents some of the techniques and the range covered by them.

3.2.1 Doppler Shift Attenuation Method

The Doppler Shift Attenuation Method (DSAM) utilizes the fact that in a stopper material, the Doppler effect is attenuated as the nuclei are slowing down inside the stopping material. Assuming that a gamma-ray from an excited state is emitted at rest with an energy E_γ, the Doppler-shifted energy

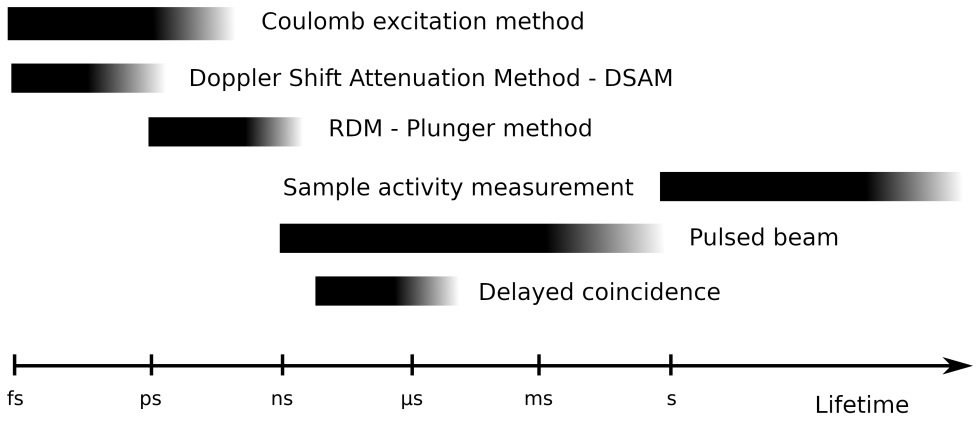

Figure 3.10: Schematic representation of the region of lifetimes covered by each technique. Adapted from [26].

E'_γ is given by the equation 3.2.

$$E'_\gamma \;=\; E_\gamma \frac{\sqrt{1 \,-\, \beta^2}}{1 \,-\, \beta\, cos\theta} \tag{3.2}$$

If the β is small, the energy shift is given by the equation 3.3.

$$E'_\gamma \;\approx E_\gamma\,(1 + \beta\, cos\theta) \tag{3.3}$$

From this equation we can obtain the Doppler shift (eq. 3.4), by recalling $\Delta E = E'_\gamma - E_\gamma$.

$$\Delta E = E_\gamma \beta\, cos\theta \tag{3.4}$$

The equations above are valid only for Doppler shifts, and in the DSAM, it is modified because the nucleus is being continuously slowed down inside the stopping material; the modification to the eq. 3.4 can be achieved by including a term $F(\tau)$ (eq. 3.5), which is a function of the stopping power of the material and the lifetime of the level being depopulated by the gamma-ray.

$$\Delta E(\tau) \;=\; F(\tau) E_\gamma \beta\, cos\theta \tag{3.5}$$

As suggested by the eq. 3.5, the observed Doppler shift also depends on the observation angle. In this technique is crucial to know the stopping power of the stopping material, so the lifetime of the excited states can be extracted as a parameter by fitting the deformed gamma-ray peak envelope.

To measure lifetimes in the range of DSAM for the mirror pairs A=47 and A=49, the setup AGATA + DIAMANT + NEDA + Neutron Wall has been used. The AGATA configuration used during the experiment was such that all detectors were positioned at backward angles to the beam direction, meaning that the Doppler shifts will be negative ($\theta > 90°$), and the full peak energy in the spectra will be deformed to the left as can be observed in the Figure 3.11. The target utilized in this experiment possesses a gold

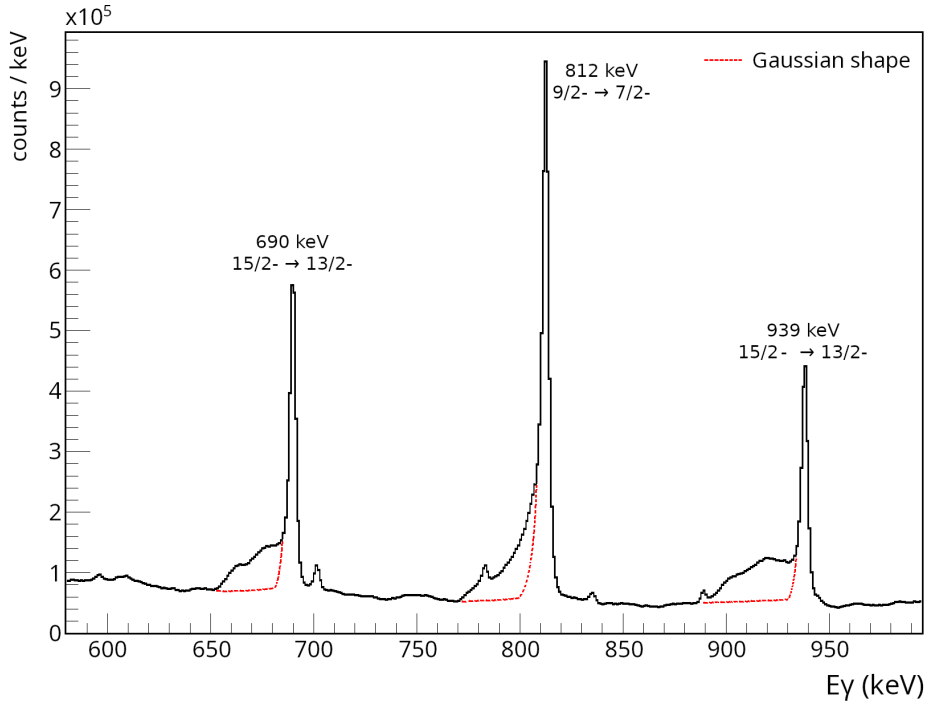

Figure 3.11: Experimental spectrum showing deformed energy peaks in a ^{49}Cr spectrum due to the Doppler shift. It is possible to observe that for the transitions shown the peaks strongly deviates from a Gaussian shape.

backing of 10 mg/cm^2 to stop the recoiling residual nuclei produced in a fusion-evaporation reaction. Some possible shapes for the function $F(\tau)$ in

the literature accounting for different effects can be found in the references [67, 68, 69].

3.3 Data selection

Fusion-evaporation reactions open many reaction channels in the reaction which can overshadow the low-intensity channels under investigation. The trigger conditions to record an event during the data acquisition were gamma-gamma or gamma-neutron coincidence, which suppresses non-neutron-related events. A total of $\approx 10^{10}$ coincidence gamma-ray events were recorded during the experiment, however, only a tiny fraction of them arose from the desired reaction channels, i.e., gamma-rays in coincidence with the emission of α-particles and neutrons (^{47}Cr), or two neutrons and a proton (^{49}Mn). For this reason, the necessary selection of the reaction channels is performed by identifying the particles and splitting the data into coincidence channels. The following section describes the adopted procedure to filter and select data for AGATA and its ancillaries. A detailed description of the processing of the signals performed to store an event is given in Appendix A.

3.3.1 AGATA and its ancillary detectors

A careful selection of the AGATA processed events is needed to ensure proper identification of the reaction channels and avoid false coincidences. The AGATA detectors were calibrated using runs performed with ^{60}Co and ^{152}Eu radiation sources. The same runs were also used to find the parameters and perform the neutron damage correction, which can recover the normal Gaussian shape response of the detectors [70]. These source runs allowed the estimation of the relative efficiency of AGATA detectors. Although the efficiency curve was fit using formulas commonly used for Compton-suppressed unsegmented germanium detector arrays [71], the curve presented was satisfactory for the present work. The AGATA processed event presents the gamma-ray energy data in two different ways: the tracked and core (untracked) (Figure 3.12). As the name suggests, tracked gamma-ray spectra

are constructed using the energy reconstructed by the tracking algorithm, while untracked gamma-ray spectra are constructed using the energy collected in the central contact of the crystal detector. Figure 3.13 shows the relative efficiency curve for tracked and core (untracked) gamma-rays. The efficiency after tracking, as expected, is higher, for the most part of the energy spectrum. To take advantage of the full capability of AGATA, all spectra used for spectroscopy purposes in this experiment were created using tracked gamma-ray energies. The energy calibration of the individual crys-

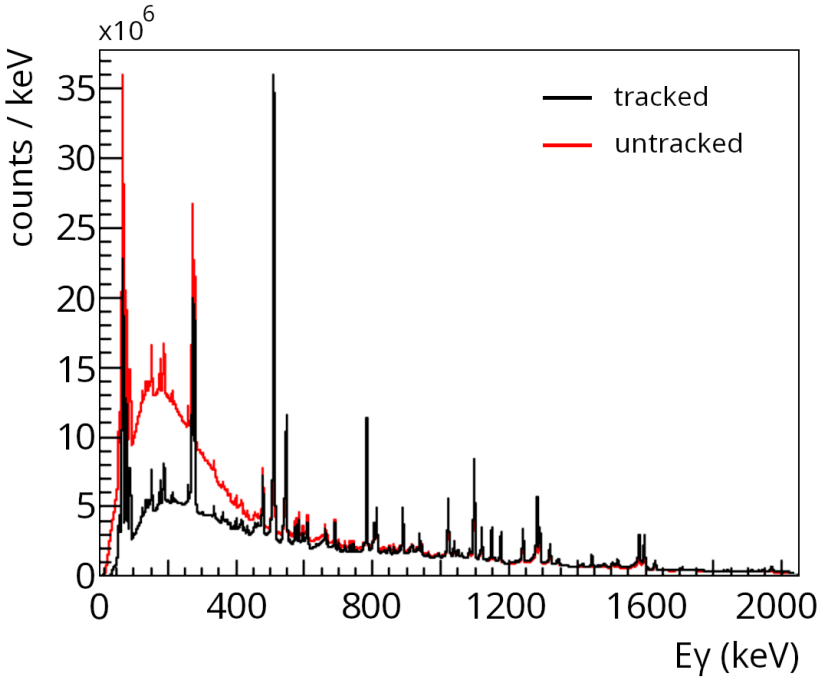

Figure 3.12: Comparison between tracked gamma-ray and core energy spectra.

tals needs to be verified as small deviations can occur after correction due to radiation damage, by plotting the crystal ID against the energy in a 2D spectrum it is possible to observe and fix miscalibrated crystals, as shown in figure 3.14. Once the data is properly calibrated it can be sorted into final gamma-gamma coincidence matrices, allowing the identification of coincident gamma-ray transitions, as shown in figure 3.15. Coincidence matrices can be

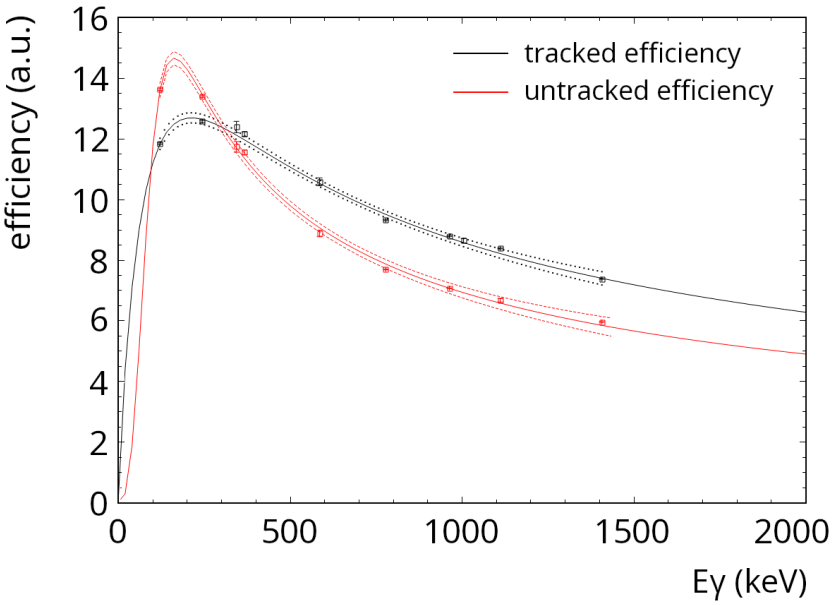

Figure 3.13: Tracked and untracked gamma-ray energy efficiency curve. The dotted curves represent 1 sigma confidence limit.

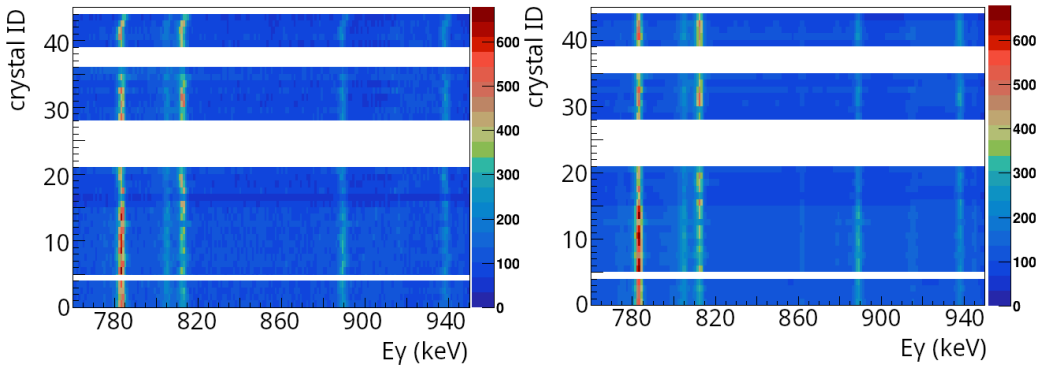

(a) (b)

Figure 3.14: a) Bi-parametric histogram containing the AGATA crystal ID vs energy prior to the last alignment, it is possible to notice a misalignment between certain crystals; b) Bi-parametric histogram containing the AGATA crystal ID vs energy after the last alignment, it is possible to notice the alignment between all of the crystals.

built after the adjustments, allowing easy visualization of the gamma-ray cascade when gating on gamma-ray transition energy. The stored events are

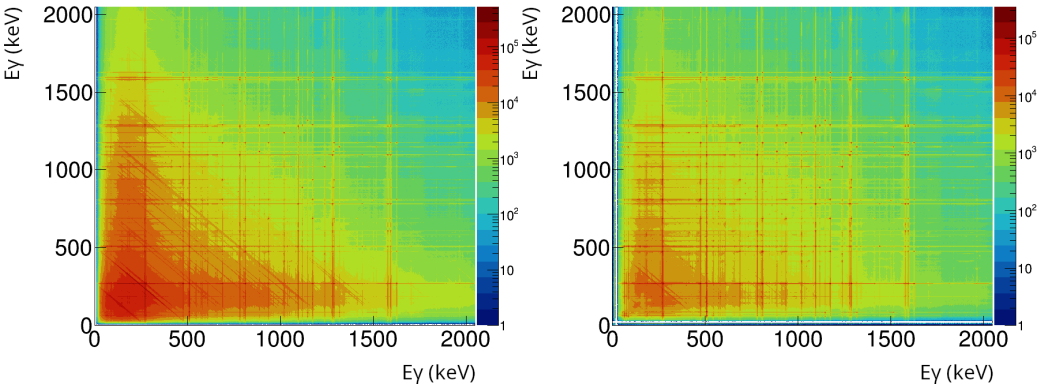

(a) Matrix using untracked gamma-rays. (b) Matrix using tracked gamma-rays.s

Figure 3.15: Gamma-gamma coincidence matrices for untracked and tracked gamma-ray events.

built using time coincidence windows of 200 ns. This is intended to observe possible event construction errors and to avoid the necessity of several reprocessing of the data to find the optimal size for the time windows. In order to minimize random coincidences it is important to use narrower time coincidence windows. During data selection, the time window is narrowed to 40 ns as shown in Figure 3.16. Similar conditions on time differences are used for AGATA, DIAMANT, and NEDA, and the values were carefully determined to maximize efficiency and prevent leaking.

3.3.2 Gamma-ray coincidence matrices

The sorting of coincident gamma-ray data into 2D energy matrices, also known as gamma-gamma matrices, is very useful to perform gamma-ray spectroscopy, as it can properly unveil the gamma-ray coincidence cascades, and allow further data selection. Gamma-ray coincidence matrices were produced for the nuclei being studied in this work imposing conditions to perform reaction channel selection. For instance, the gamma-gamma matrix used to study

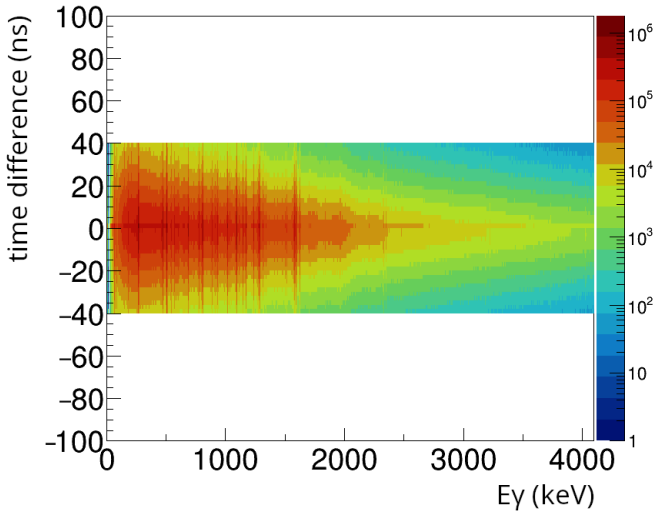

Figure 3.16: Time difference between coincident tracked gamma-rays vs energy. It is possible to observe the time window for tracked gamma-gamma coincidences.

the gamma-rays from the ^{49}Cr was produced by imposing a coincidence of gamma-rays with two protons and one neutron, while the gamma-gamma matrix for the ^{49}Mn was constructed by imposing a coincidence of gamma-rays with two neutrons and one proton. Figure 3.18 shows a 3D representation of the gamma-gamma matrix. Gates on the gamma-ray energy peaks were performed to obtain spectra in coincidence with the selected energy. The resulting spectra were used to obtain the lifetime of excited states.

3.3.3 Background subtraction

When gating on a particular gamma-ray transition on a gamma-gamma matrix, it is necessary to subtract the events in coincidence with the underlying background. Although there are several techniques for background subtraction, in the present work only two of them were applied. In the first method, a gate is set in a transition peak of interest to obtain the events in coincidence with the selected gamma-ray energy peak. One or more additional gates are set in the background near the peak to evaluate the events arising

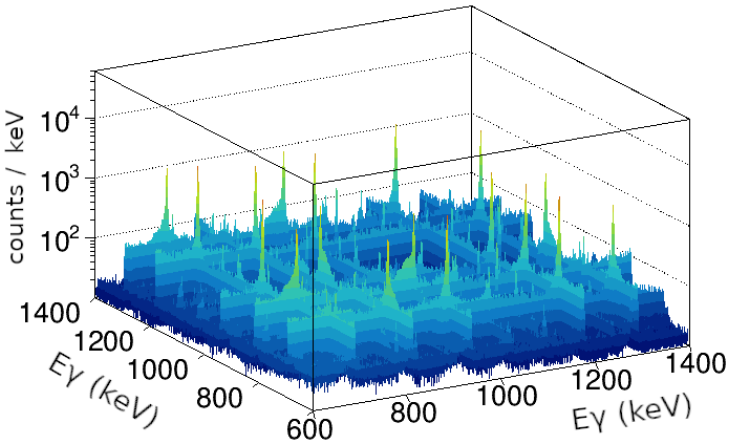

Figure 3.17

Figure 3.18: Three-dimensional representation of the symmetric gamma-ray coincidence matrices produced with AGATA data. The Gamma-gamma matrix is produced by requiring gamma rays in coincidence with two protons and one neutron.

from the background. A normalized fraction of the background projections is subtracted from the peak-projected spectrum. Such procedure removes the peaks in coincidence with the background [72]. Figure 3.19 illustrates all the described steps for the background subtraction procedure performed for a ^{49}Cr gamma-ray peak. Figure 3.20 shows the resulting background subtracted spectrum for the mirror pairs $A = 47$ and $A = 49$. The second method adopted was the `root` built-in background elimination algorithm, which implements the Sensitive Nonlinear Iterative Peak (SNIP) clipping algorithm [73, 74]. Such a method estimates the background in an iterative procedure and up to some extent can eliminate the contribution based on the number of iterations provided by the user. Figure 3.21 illustrates the SNIP method. It is important to point out that the methods serve different purposes. The first method can remove most of the transitions that are not in coincidence with the gated transition, but the background itself may not be completely removed. The second method can remove the background but the peaks in coincidence with the background are not subtracted. By

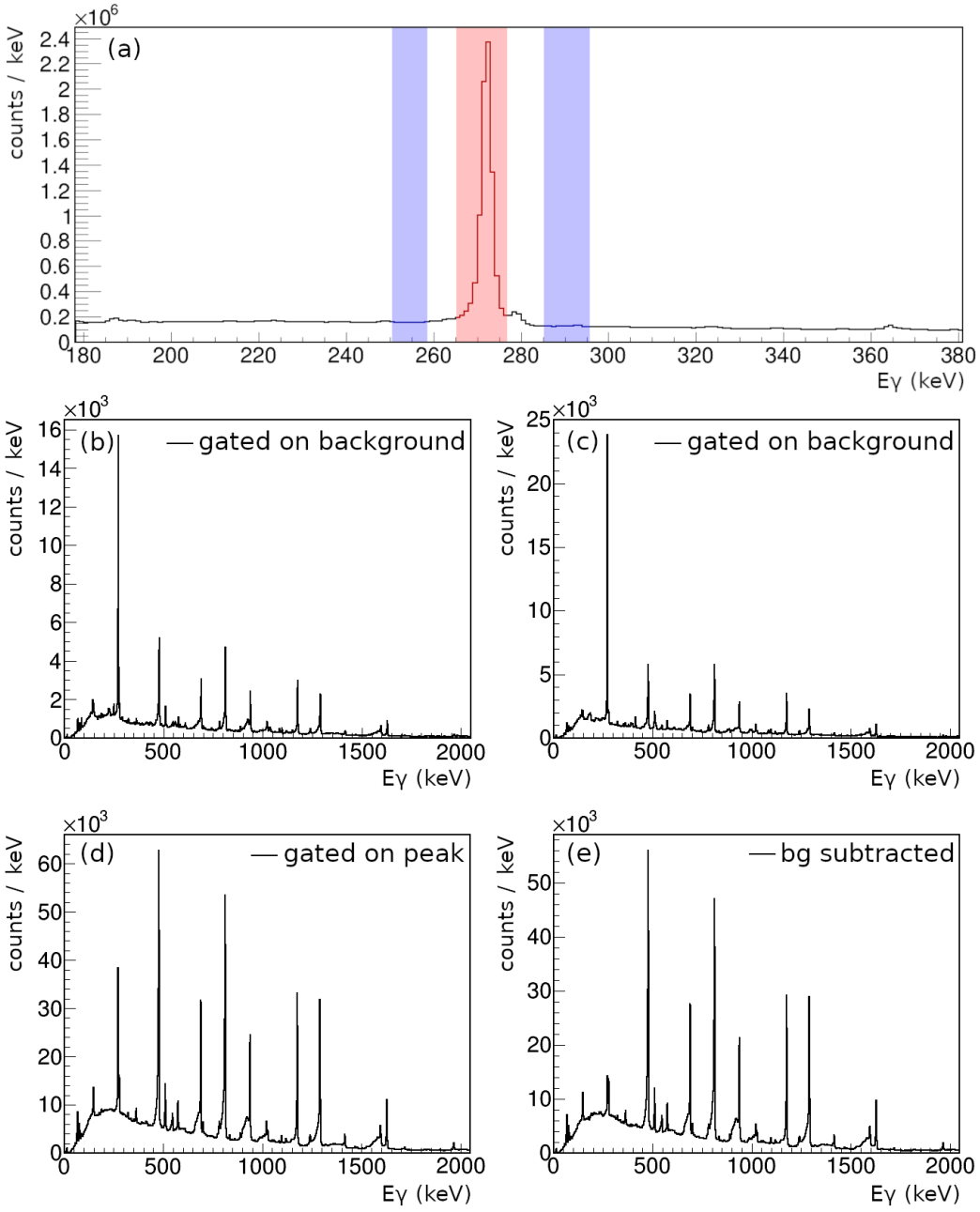

Figure 3.19: (a) Gamma-ray spectrum corresponding to the full projection of one axis of the gamma-gamma matrix. The area in red is for the peak events and the blue ones are used for the background. (b) Gamma-ray spectrum in coincidence with the leftmost blue area, corresponding to the energies from 251 to 259 keV . (c) Gamma-ray spectrum in coincidence with the rightmost blue area, corresponding to the energies from 285 to 295 keV. (d) Gamma-ray spectrum in coincidence with the red area, corresponding to the 272 keV peak. (e) background-subtracted gamma-ray spectrum, corresponding to the (d) spectrum with a subtracted fraction of the (b) and (c).

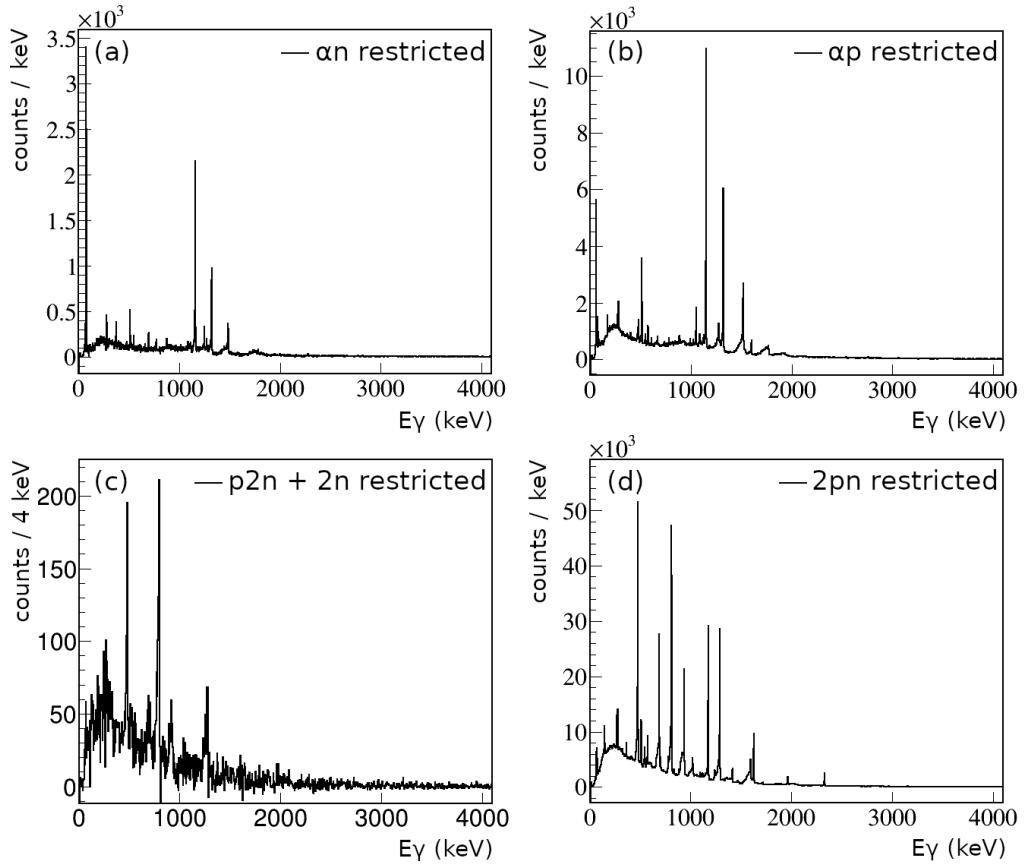

Figure 3.20: (a) Background subtracted spectrum gated on the 99 keV ($(5/2^-) \rightarrow 3/2^-$) of the ^{47}Cr. (b) Background subtracted spectrum gated on the 87 keV ($5/2^- \rightarrow 3/2^-$) of the ^{47}V. (c) Background subtracted spectrum gated on the 262 keV ($7/2^{(-)} \rightarrow 5/2^-$) of the ^{49}Mn. (d) Background subtracted spectrum gated on the 272 keV ($7/2^- \rightarrow 5/2^-$) of the ^{49}Cr.

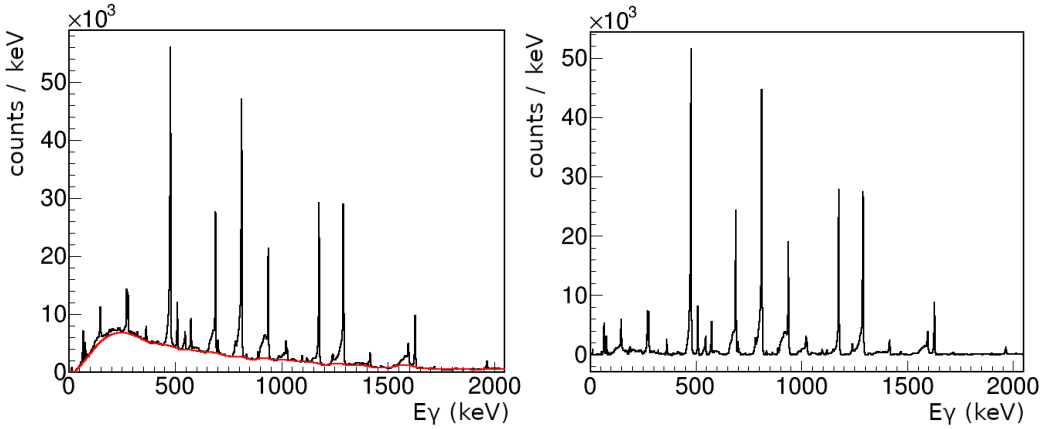

(a) SNIP estimated background. (b) Background subtracted spectrum.

Figure 3.21: (a) Gamma-ray spectra illustrating the SNIP background curve in red. (b) Gamma-ray spectrum after the SNIP background subtraction.

utilizing both methods it is possible to remove most of the undesired gamma-ray peaks with the first method and from the resulting spectra remove the background with the second one.

3.3.4 NEDA and Neutron Wall

In order to detect neutrons, the NEDA (NEutron Detector Array) and Neutron Wall were used. These ancillary neutron arrays are also sensitive to gamma radiation. Therefore, it is fundamental to identify and discriminate neutron-related events from gamma rays induced background. Discrimination can be achieved using different methods. A combination of time of flight, energy, and a digital Charge-Comparison (CC) pulse shape discrimination can be chosen to achieve maximum selectivity. The Time-of-Flight, i.e., the elapsed time between the beginning of the acquisition, given by the digital CFD[2] zero-crossover, and the stop of the acquisition, given by the accelerator, is different between gamma-ray and neutrons, which provides a first degree of discrimination as can be seen in Figure 3.22. A digital CC algorithm can be utilized for further discrimination, and it relies on the discrimination of the different pulse shapes produced by the detector depending on the type

[2]Constant Fraction Discriminator

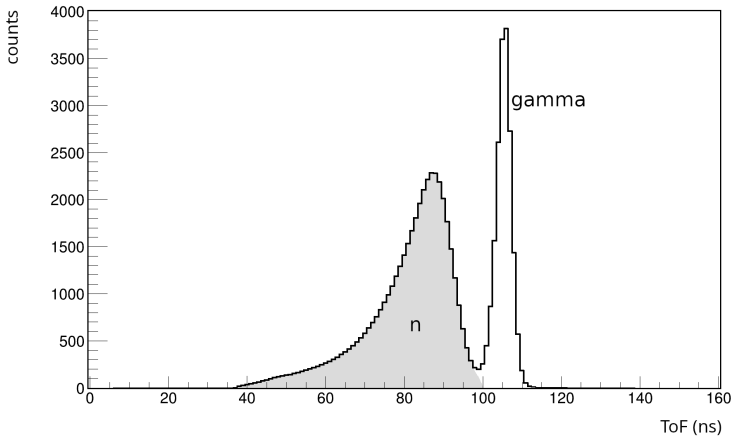

Figure 3.22: Example of time of flight histogram for the NEDA detector. It is possible to see two main regions. The highlighted area corresponds mainly to neutron-related events, and the rightmost peak corresponds to gamma-ray events.

of incident radiation [75]. The discrimination is achieved by placing two sets of gates on the digitized signal, one on the slow part and another one on the fast part of the traces, and then calculating the ratio between the integrated events lying inside the gates. The combination of the CC, ToF, and energy spectrum into bi-parametric histograms provides a straightforward way to perform neutron discrimination by setting 2D gates, as can be seen in figure 3.23. These gates allow only events lying inside to be selected as neutron correlated. The size of the gates must be carefully determined to increase the detection efficiency and simultaneously minimize leaking, i.e., the presence of non-neutron-related events in the neutron channel. Indeed gamma rays are sometimes passing the selection filters and being misidentified as neutrons. In order to select neutron events out of the detected signal, the charged comparison algorithm was combined with time-of-flight and energy, and then neutron gates were set individually for each NEDA and Neutron Wall detector. Figure 3.24 demonstrates the gates applied for single NEDA and NW detectors. It is also possible to observe the difference in the responses of NEDA and NW. The differences are evident mainly because NW detectors are positioned at 90°, a position disfavoured by the experiment

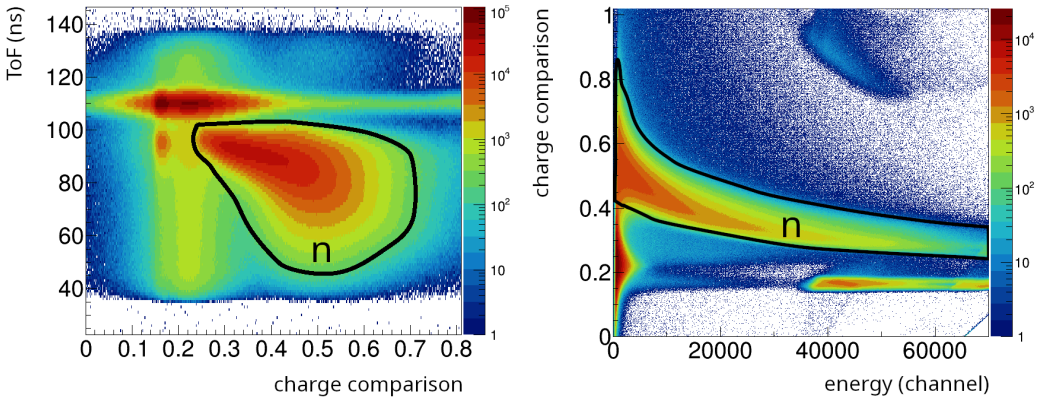

Figure 3.23: (a) bi-dimensional histogram combining ToF and CC, it is possible to observe clear discrimination between neutron and gamma-ray events, the black line corresponds to the neutron gate; (b) bi-dimensional histogram combining CC and NEDA energy, it is possible to observe discrimination between neutron and gamma-ray events, the black line corresponds to the neutron gate.

kinematics to detect neutrons compared with NEDA. The neutron detection efficiency was determined using a special run performed without a trigger on neutron events. The procedure can be summarized in the following steps and is shown in figure 3.25:

a) Gamma-ray events, in coincidence with at least one neutron, were sorted into a gamma-gamma coincidence matrix;

b) All gamma-ray events were sorted into an unrestricted gamma-gamma coincidence matrix;

c) A gate was placed in the same gamma-ray transition known to be in coincidence with one neutron in both matrices;

d) The number of events in a coincident transition is estimated in both matrices;

e) The one-neutron detection efficiency is obtained by calculating the ratio between the number of events in the neutron-gated and unrestricted one;

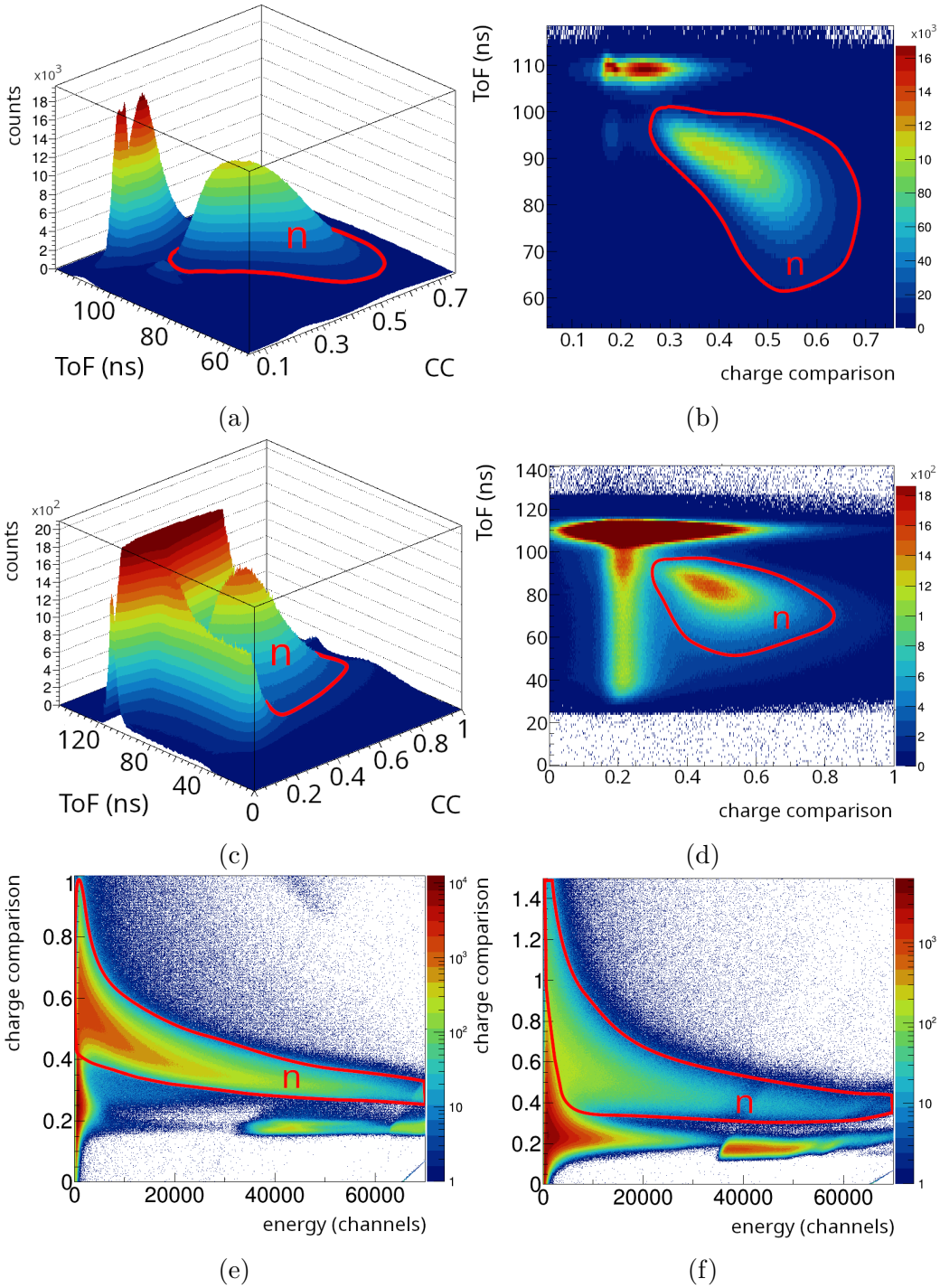

Figure 3.24: a) ToF vs CC histogram for a NEDA detector. b) Projection on the z plane of the ToF vs CC for a NEDA detector. c) ToF vs CC histogram for a NW detector. d) Projection on the z plane of the ToF vs CC for a Neutron Wall detector. e) Projection on the z plane of Energy vs CC histogram for a NEDA detector. f) Projection on the z plane of Energy vs CC histogram for a NW detector.

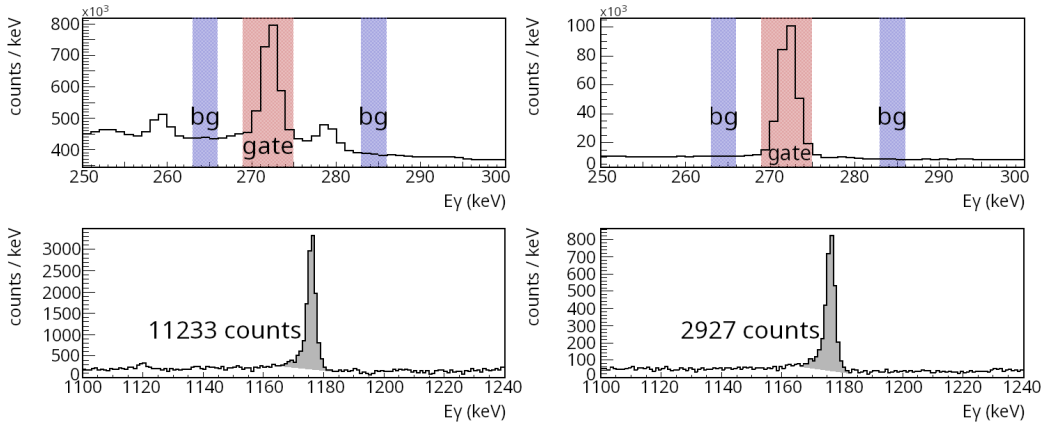

(a) (b)

Figure 3.25: a) Gate in the 272 keV transition from ^{49}Cr in the unrestricted gamma-gamma matrix and its background subtracted spectrum showing the 1177 keV coincidence transition. b) Gate in the 272 keV transition from ^{49}Cr in the at least one neutron gamma-gamma matrix and its background subtracted spectrum showing the 1177 keV coincidence transition.

The number of peak events in the figure 3.25 was obtained following the procedure described by Gordon R. Gilmore [76]. The contamination of non-neutron correlated events (leaking) was obtained by performing a similar procedure but gating in a gamma-ray transition known to not have a neutron in coincidence.

3.3.5 Charged Particle Selection

The charged particle events selection, aiming to provide channel discrimination for light-charged particles, followed a procedure analogous to the neutron selection but using DIAMANT data to discriminate between the protons and alpha particles related events. As protons and alpha particles generate different detector responses, the ratio between the slow and the fast part of the signal provides the Particle IDentification (PID), as shown in the figure 3.26. The combination of the PID and energy histogram into a bi-parametric histogram provided a better approach to perform the discrimination, as shown in figure 3.27. The gate size for protons and alpha particles

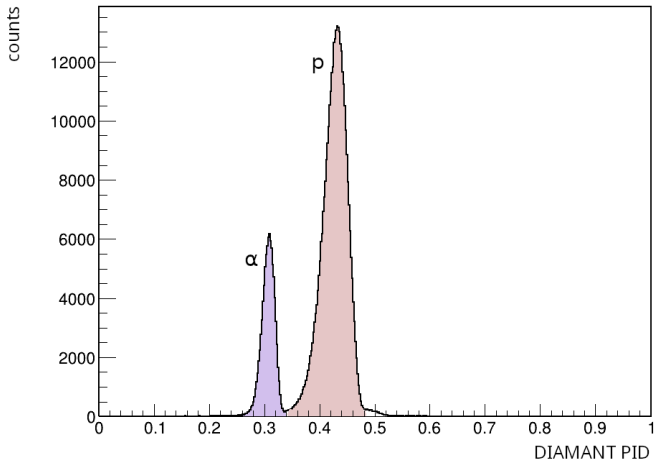

Figure 3.26: Particle identification histogram with the highlighted type of particle.

must be carefully determined to increase the detection efficiency and simultaneously minimize leaking. The efficiencies for one-proton and one-alpha

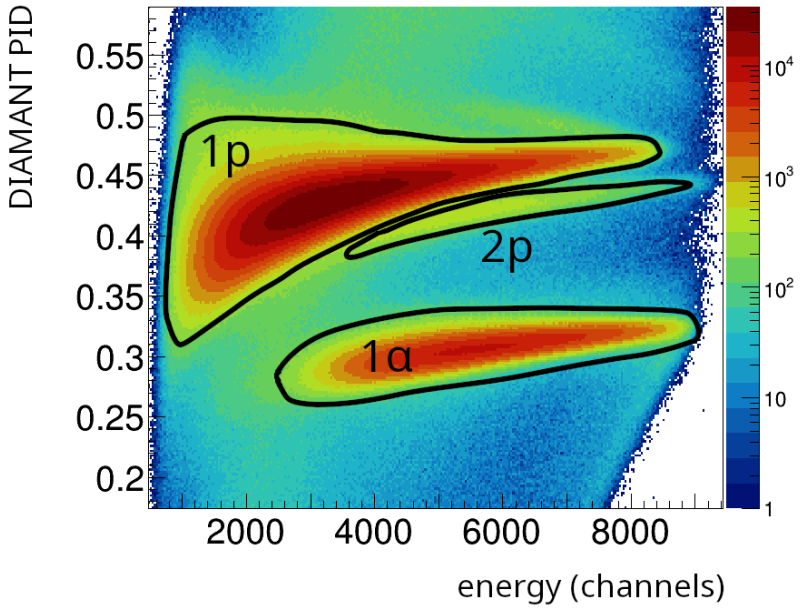

Figure 3.27: One proton (1p), two protons (2p) and one alpha particle (1a) identification.

detection were obtained following an analogous procedure to the one performed for neutrons and the results are shown in table 3.1. The efficiency

Table 3.1: Obtained efficiencies for the ancillary detectors.

Channel	Efficiency (%)	Leaking (%)
1n	26.1 (7)	0.1%
1p	40 (1)	0.1%
1a	26.1 (6)	$< 0.1\%$

values are compatible with the expected ones for the ancillary arrays and provide a layer of consistency check for the data. The time windows for the coincidences were carefully determined and are arranged in table 3.2.

Table 3.2: Timming coincident events.

Detector	Time gate (ns)		
	AGATA	DIAMANT	NEDA + NW
AGATA	40	90	90
DIAMANT	40	40	-
NEDA + NW	90	-	40

3.4 Data analysis procedure

The experimental data to obtain the lifetimes of excited states can be analyzed using different implementations of data analysis for DSAM. The methods rely on reproducing the Doppler broadened components of the gamma-ray transitions to extract the lifetime information. In this work, two methods based on Monte Carlo simulations have been used to reproduce the observed Doppler-broadened gamma-ray transitions and extract lifetimes.

3.4.1 LINESHAPE Program Suite

The first lifetime determination method was performed with a modified version of the LINESHAPE set of programs [77, 78]. This suite of software was successfully used to analyze several GASP experiments in DSAM lifetime measurements. The first program is called `dechistu` which performs Monte Carlo simulations of the velocity history of each recoiling nucleus while slowing down inside the target and backing materials, assigning in each discrete

step a position and velocity vector for it. The parameters of the nuclear reaction such as beam energy, target composition, and evaporated particles are also taken into account. The code describes the nuclear stopping power of the recoiling ions according to the LSS theory [79], and the electronic one according to the Northcliffe-Schilling corrected for atomic shell effects [80, 81]. The second program is called `histaver40` which uses the geometry of the detector to generate response functions based on the recoil velocity histories generated before. The last software of this set of programs is called `dbls2k` which allows the fit of the previously generated response as a function of the lifetime of the states and gamma-ray intensities. The intensity of the gamma rays and their branching ratio is necessary for the fitting procedure. Additional artificial feeding[3] can be considered to account for missing intensity from unobserved feeding transitions, the so-called side feeding. The LINESHAPE programs have been used to determine the lifetime of excited states in the nuclei ^{47}Cr, ^{47}V, ^{49}Mn, and ^{49}Cr, and the results are presented in next section. Although very capable, this set of programs is limited to the scope of lifetime measurements of short-lived (< 1 ps) excited states.

3.4.2 GEANT4

It is known that Monte Carlo simulations are an essential part of planning and analyzing contemporary experiments in nuclear and high-energy physics. The increasing complexity of those research fields demanded the creation of a general framework, easily configurable and expandable for a wide range of applications. GEANT4 is a toolkit for simulating the passage of particles through matter, created by worldwide collaboration. Since its inception, the code was provided with several libraries aiming for different applications [82]. The simulations basically include the generation of the event, setup geometry, and the physical processes involving the simulated particles and material volumes. Using that information, the GEANT4 kernel produces the history of each simulated particle in discrete steps, and, by following the

[3] Added gamma-ray transition coming from an unobserved level.

particles over the successive interaction steps, it is possible to retrieve the desired information [82, 59].

In this work, the GEANT4 simulations were split into three basic steps, event generation, event building, and event selection or reconstruction. The event generator considers the interaction processes between the beam and the target, the evaporation of particles from the formed compound, the recoil of the residual nucleus into the target material, and the interaction between the emitted gamma rays with the detector materials. This generates an output file containing the required information to build an event. Then, the event builder reads the previously generated event file and groups up the events based on given parameters, and the event selection sorts the built events generating gamma-gamma matrices and histograms that accurately reproduce the experimental results.

3.4.3 `Agata` simulation code

The `Agata` simulation code is based on C++ classes of the Geant4 framework and has been developed to evaluate the AGATA performance under a wide range of experimental conditions [83]. The event generation is performed using the G4 simulation libraries to provide a full microscopic description of the radiation interaction processes, considering the type of reaction, array geometry, and passive materials. This code is capable of simulating the gamma-ray emission of excited nuclei during in-beam experiments and outputs the results as a list of simple events, where only one photon or particle is emitted at a time, and higher multiplicity events are built by the event builder. The excited states lifetimes and structure are included with a configuration file. The adequate geometry description and event generation are crucial for the good quality of the simulation. For this reason, a geometry file containing the details of the experimental setup used in each experiment must be provided by the user since their description is not embedded in the code.

The tracking algorithm is also not included in the event generation code,

and it is applied to the simulated data by the event builder that reads the simulation output. The advantage of this modular approach is the easy exchange of geometry and algorithms without needing to change the code. In order to build the events with the gamma rays properly tracked, it is necessary to obtain a response function that considers the detector's finite resolution and the effects caused by neutron-damaged detectors, which produce left tails in the spectrum photopeaks due to an incomplete charge collection. This is achieved by finding a smearing function that, when applied to the simulation, can reproduce the experimental run with an ^{152}Eu source (Figure 3.28). The smearing function was determined as a Gaussian with an exponential

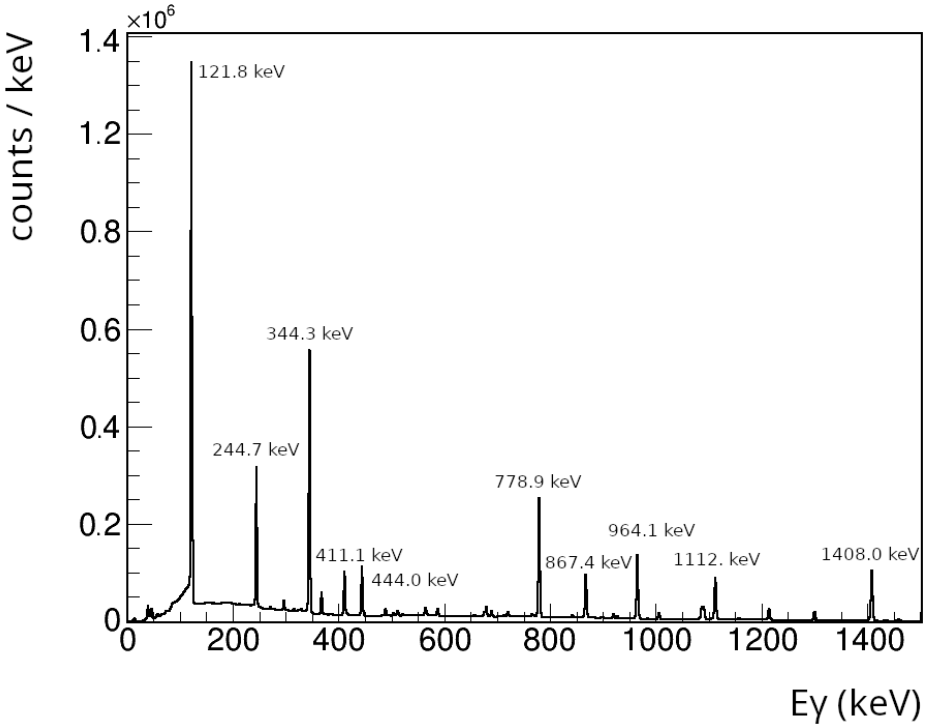

Figure 3.28: Gamma-ray spectrum observed in an experimental run performed with an ^{152}Eu source utilized to observe the experimental response function in a wide range of energies.

left tail in the gamma-ray peaks (Figure 3.29a). Like real Germanium detectors, the simulated energy resolution (FWHM) depends on the energy. A weight function is used to control the size of the smearing effect so that

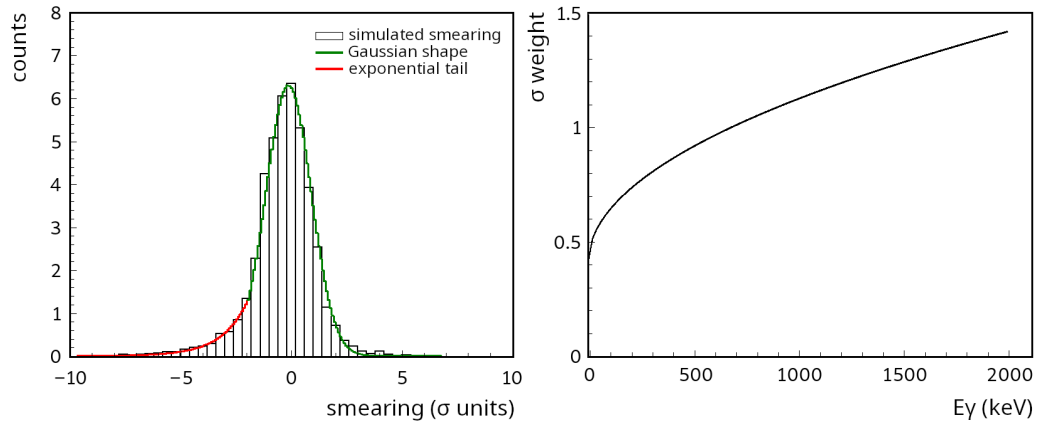

(a) (b)

Figure 3.29: (a) Smearing function shape, a Gaussian distribution with a left tail. (b) Energy-dependent weight function was created to reproduce the energy dependency of the germanium detector energy resolution.

the simulation can reproduce the experimental response function. A function taken from the literature [84] was slightly modified to meet the actual resolution observed in the experimental gamma-ray spectra (Figure 3.29b). After the response function implementation, the experimental and simulated gamma-ray spectra behave similarly, as shown in Figure 3.30.

Finally, in the selection step, the events were sorted into `root` histograms with the same set of parameters used to build the experimental data. The key parameter to correctly reproduce the experimental data is the population of the excited nuclear states, which can be obtained from the experimental spectra by accounting for the intensities of the gamma rays depopulating the excited nuclear states. The lifetimes are determined by comparing the simulated spectrum with the experimental one and finding the value that minimizes the χ^2 (grid-search algorithm). Figure 3.31 shows a comparison between the experimental and simulated spectra for the ^{50}Cr studied with this procedure [85]. This lifetime determination procedure was followed to determine the lifetime of excited states in the nuclei ^{47}Cr, ^{47}V, ^{49}Mn, and ^{49}Cr. The results and comparison with LINESHAPE results are presented

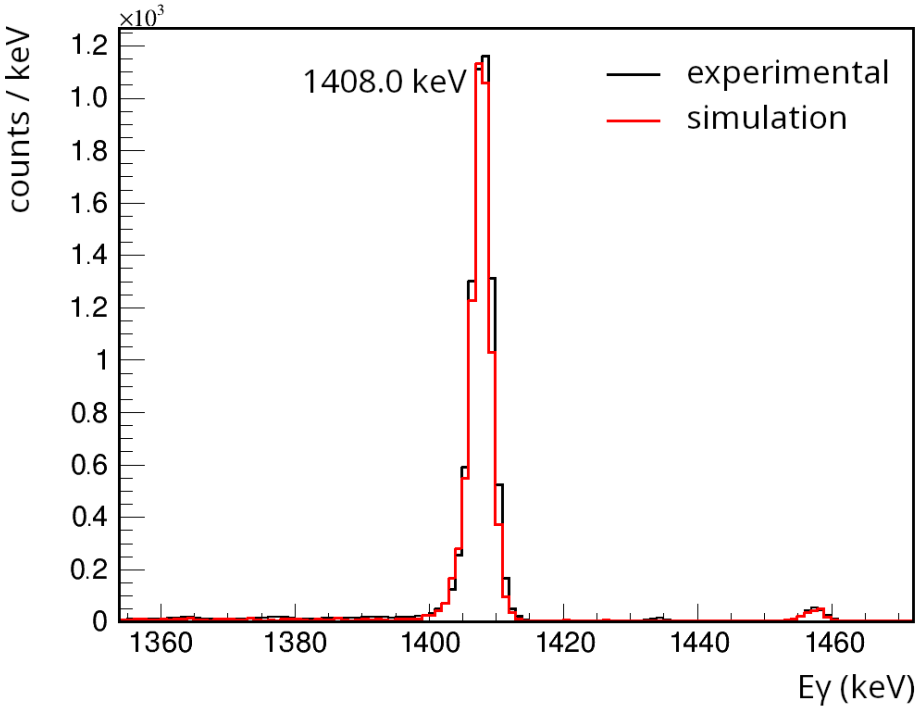

Figure 3.30: Experimental and simulated Gamma-ray peak of 1408.0 keV emitted by an ^{152}Eu source.

in the next section.

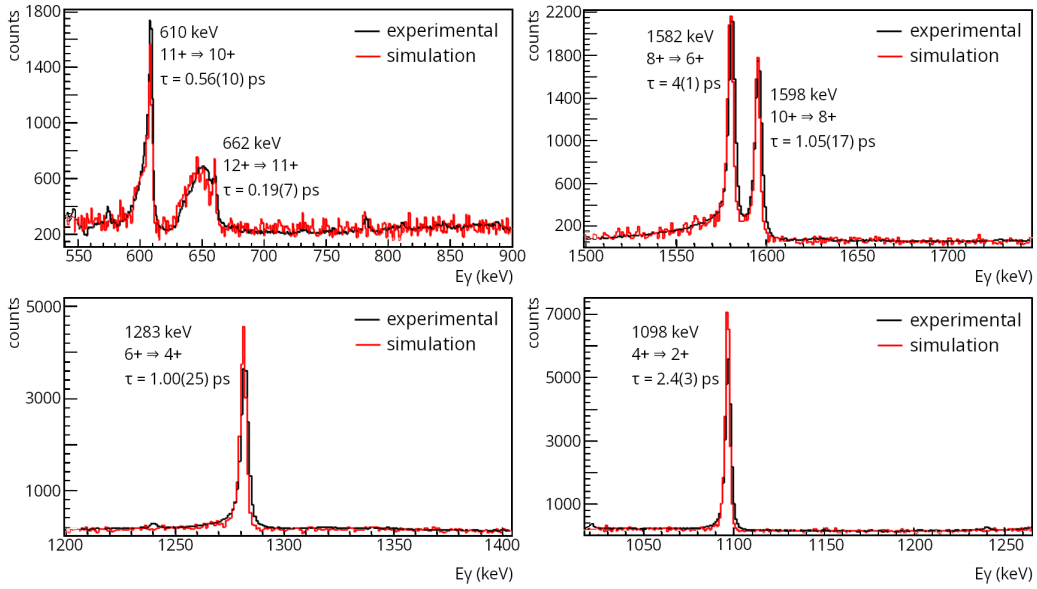

Figure 3.31: Comparison between simulated and experimental gamma-ray spectra emitted by the ^{50}Cr nuclei. Taken from [85].

3.5 Experimental results

The data analysis of this experiment was performed, for the mirror pairs ^{47}Cr - ^{47}V and ^{49}Mn - ^{49}Cr, following the procedures previously described. The collected data was divided across 84 different runs, being 67 with the beam on target and 17 for calibration purposes. The data analysis is shown first for the ^{47}Cr and ^{49}Mn as those are the weakest populated channels under analysis, and then for their respective mirrors to validate the adopted data analysis procedure.

3.5.1 The lifetime of ^{47}Cr excited states

The ^{47}Cr nucleus is produced by the αn exit channel in the fusion-evaporation reaction ^{36}Ar + ^{16}O. This nucleus was predicted to have a production cross-section of around 6 mb according to PACE [86] calculations. To observe the gamma-rays depopulating the excited states of the ^{47}Cr, the data from the AGATA + NEDA + Neutron Wall + DIAMANT was sorted

into αn-restricted gamma-ray coincidence matrix. The gamma-ray spectrum corresponding to the full projection of the αn-restricted gamma-gamma matrix is shown in Figure 3.32, where the most intense transitions from the ^{47}Cr and the contamination peaks from the ^{49}Cr and ^{46}V are highlighted. If the

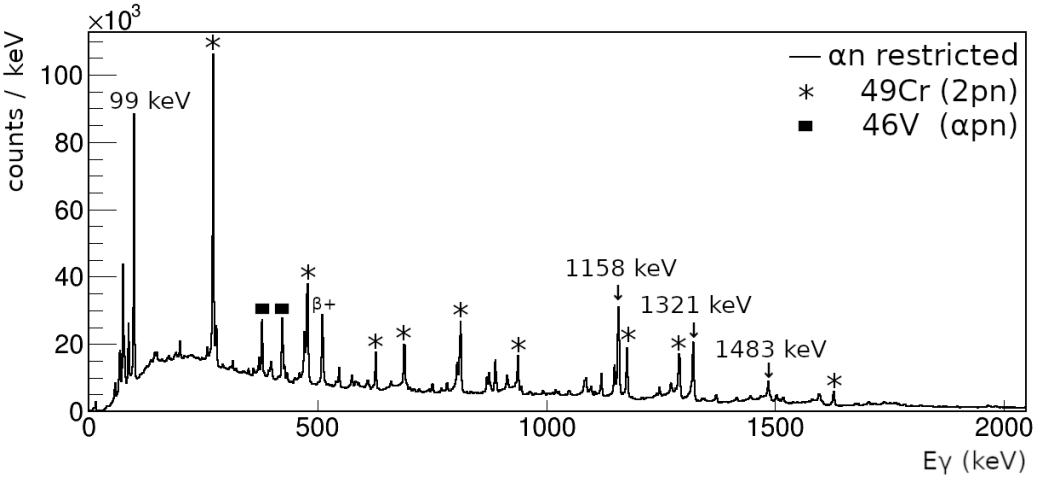

Figure 3.32: Gamma-ray spectrum projected from the αn-restricted gamma-gamma matrix. The indicated energies correspond to the most intense transitions depopulating excited states in the ^{47}Cr. The most intense contamination peaks are also presented.

gamma-ray transitions of the ^{47}Cr were not known, it would be possible to construct the level scheme for it by gating on different gamma-ray energies that do not belong to the known contaminants. However, several gamma-ray transitions belonging to the ^{47}Cr are known in literature [12], and given the difficulty of finding an isolated peaks[4] to perform gates in this αn-restricted gamma-gamma matrix, this work took from the literature the order of the gamma-rays in the level scheme and the J^{π} assignment. By gating on any isolated transition energy corresponding to gamma-ray energy belonging to the ^{47}Cr, it is possible to eliminate most of the contamination present in the full projection of the matrix. The 99 keV $((5/2^{-}) \rightarrow 3/2^{-})$ gamma-ray transition is not overlapping with contaminants and is suitable for gating for subsequent lifetime determination. In Figure 3.33, the background-subtracted gamma-

[4]Interest peaks not overlapping with contaminants.

ray spectrum gated on the 99 keV ($(5/2^-) \rightarrow 3/2^-$) gamma-ray energy is shown. The experimental values for the gamma-ray energies found in the present work are shown in the level scheme shown in Figure 3.34.

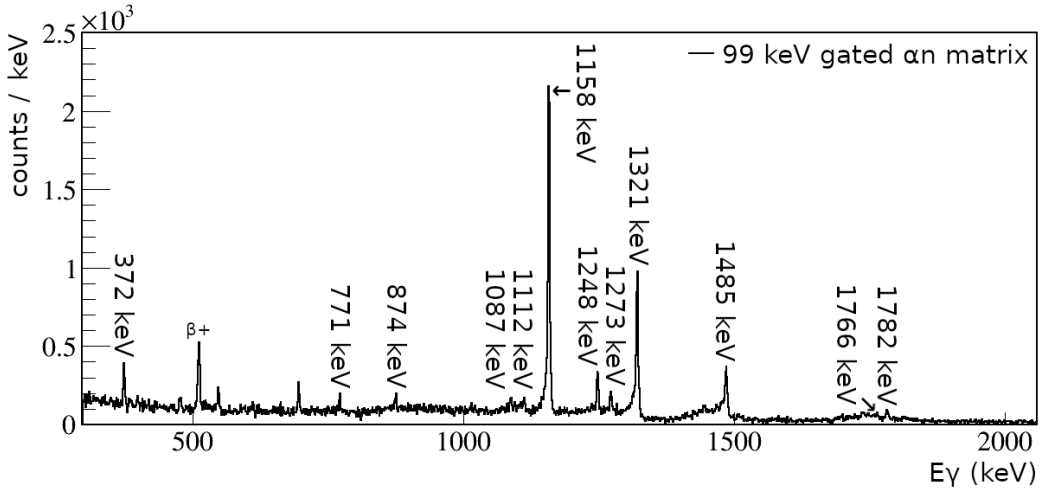

Figure 3.33: Background subtracted gamma-ray spectrum produced by gating on the 99 keV ($(5/2^-) \rightarrow 3/2^-$) gamma-ray transition in the αn-restricted gamma-gamma matrix. The indicated energies correspond to the observed transitions which depopulate excited states in the ^{47}Cr. The 75 keV transition is out of the range of this plot.

Lifetimes of excited states of the ^{47}Cr in the sub-picosecond range were determined using the different sets of programs previously presented. The level scheme and the gamma-ray intensities, obtained from the experimental spectrum were used as input parameters to obtain the lifetime of excited states in the ^{47}Cr. The lifetime estimation procedure started with the LINESHAPE package, as it is faster to perform than the Geant4 approach, and the found lifetime values can be used as starting values for the Geant4 grid search algorithm. A total of 50000 recoiling nuclei velocity histories were simulated to produce a generic response function of the detectors present in the array. The lifetimes are extracted as a parameter from the fitted curves in the experimental spectrum. In Figure 3.35 the fits performed with the LINESHAPE package are shown. The uncertainty in lifetime estimation is composed of statistical and systematic components. The statistical uncer-

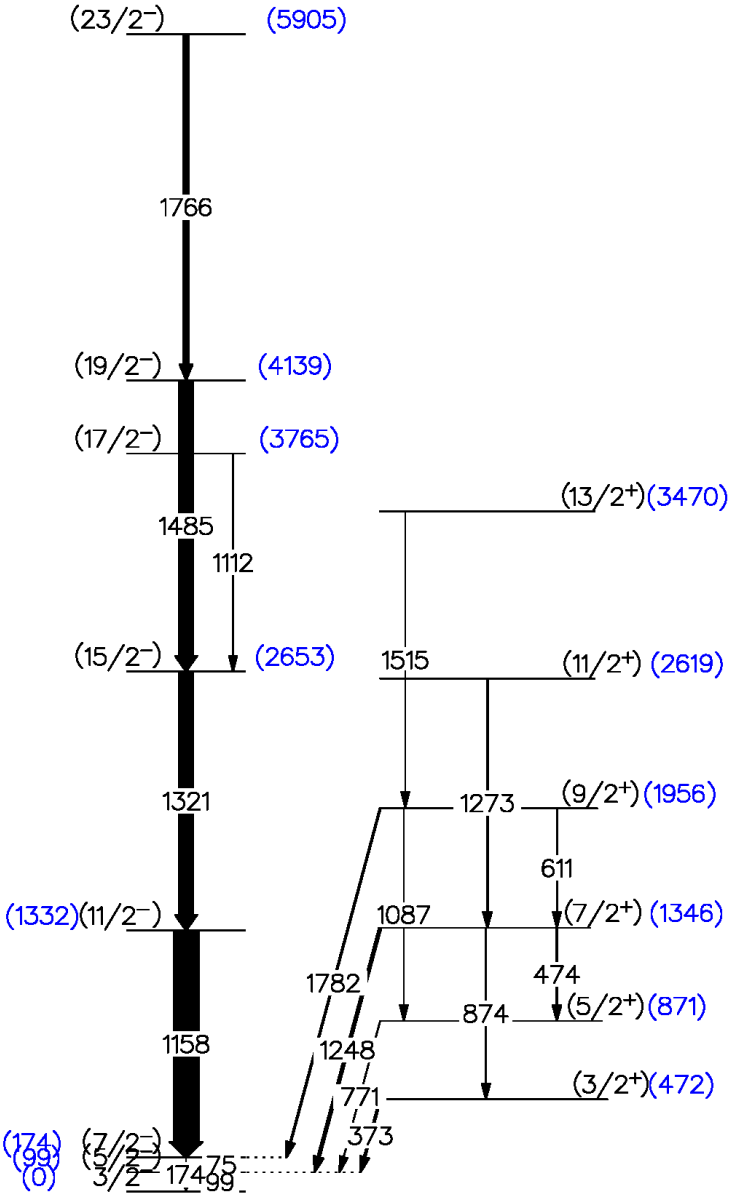

Figure 3.34: Partial level scheme for the ^{47}Cr with the gamma-ray energies found in the present work. The arrow's width is proportional to the intensities.

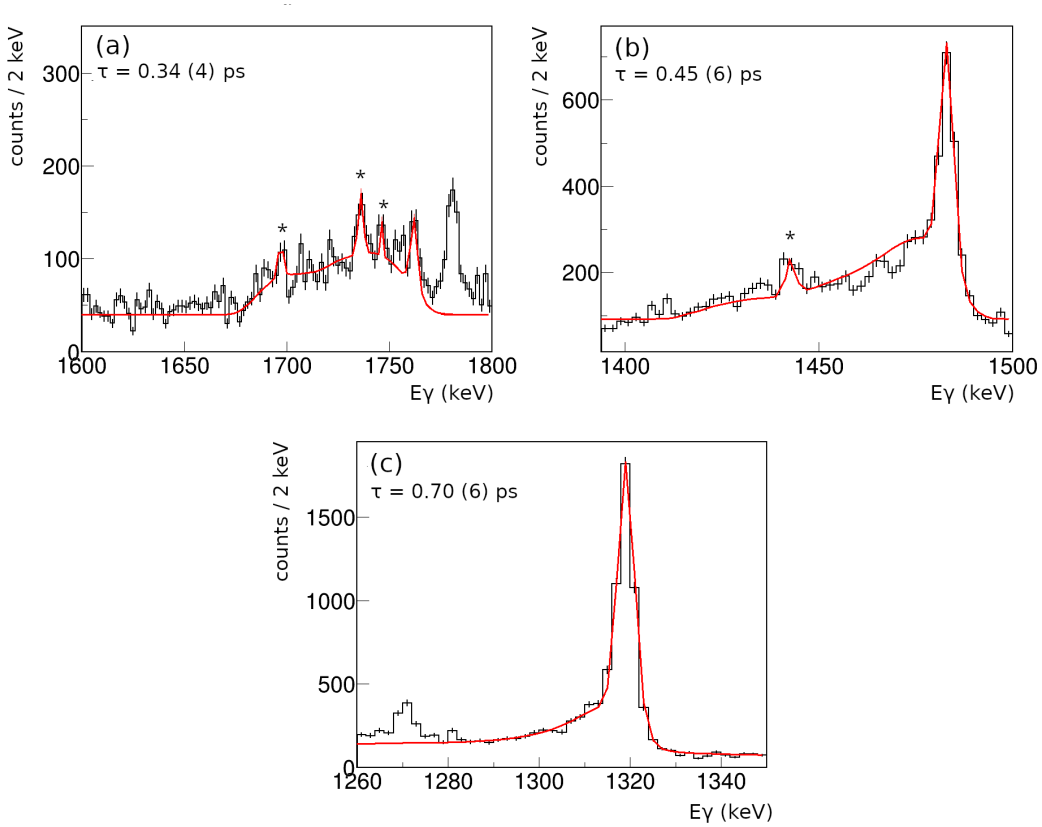

Figure 3.35: (a) LINESHAPE fitted for the 1766 keV gamma-ray transition that depopulates the $(23/2^-)$ state. (b) Same for the 1485 keV gamma-ray transition that depopulates the $(19/2^-)$ state. (c) Same for the 1321 keV gamma-ray transition that depopulates the $(15/2^-)$ state. The symbol (*) indicates the presence of a stopped peak arising from an unidentified transition.

tainty was estimated by evaluating the χ^2 curve as a function of the lifetime. The difference between χ^2_{min} and $\chi^2_{min} + 1$ was assumed as statistical uncertainty. In Figure 3.36, the χ^2 as a function of a lifetime is shown. The systematic errors have two main sources, the high uncertainty in the stopping power at low recoil velocity, and the side feeding effects in the line shape of the transition. The uncertainty due to the stopping power was considered following the convention set by Brandolini et al. [68], 8% for lifetimes down to 0.3 ps, and up to 15% below this value. The uncertainty due to the side feeding was estimated by evaluating the state lifetime in the minimum and maximum value of the side feeding times. The difference in the state lifetime obtained for the different side feeding times was adopted as a side feeding contribution to the uncertainty in the level lifetime and oscillated between 0.02 and 0.03 ps.

The values obtained with the LINESHAPE set of programs were used as a starting point for the grid-search lifetime estimation procedure with Geant4. In this approach, the lifetimes of the excited states were determined by comparing the experimental spectrum with the simulated one. Several simulations of the full spectrum were performed until achieving the minimum χ^2. A total of twenty million events were simulated aiming to reproduce the observed experimental spectrum. The comparison between the experimental and the best simulated gamma-ray spectrum is shown in Figure 3.37. The estimation of the lifetimes with Geant4 has the advantage of considering the full geometric description of the experimental setup and complete level scheme, which allowed the assignment of inferior limits for the lifetimes of certain excited states. In Figure 3.38, the line shapes corresponding to the obtained lifetimes are shown. An analogous procedure to obtain the uncertainty was followed, considering the statistical and systematical components in the same way as in the LINESHAPE method. The χ^2 as a function of the lifetimes are shown in Figure 3.39. The average velocity of the produced ^{47}Cr was estimated as 5.79% c, which stops, on average, after $\approx$ 1 ps according to TRIM calculations. For this reason, the longest lifetime that can be

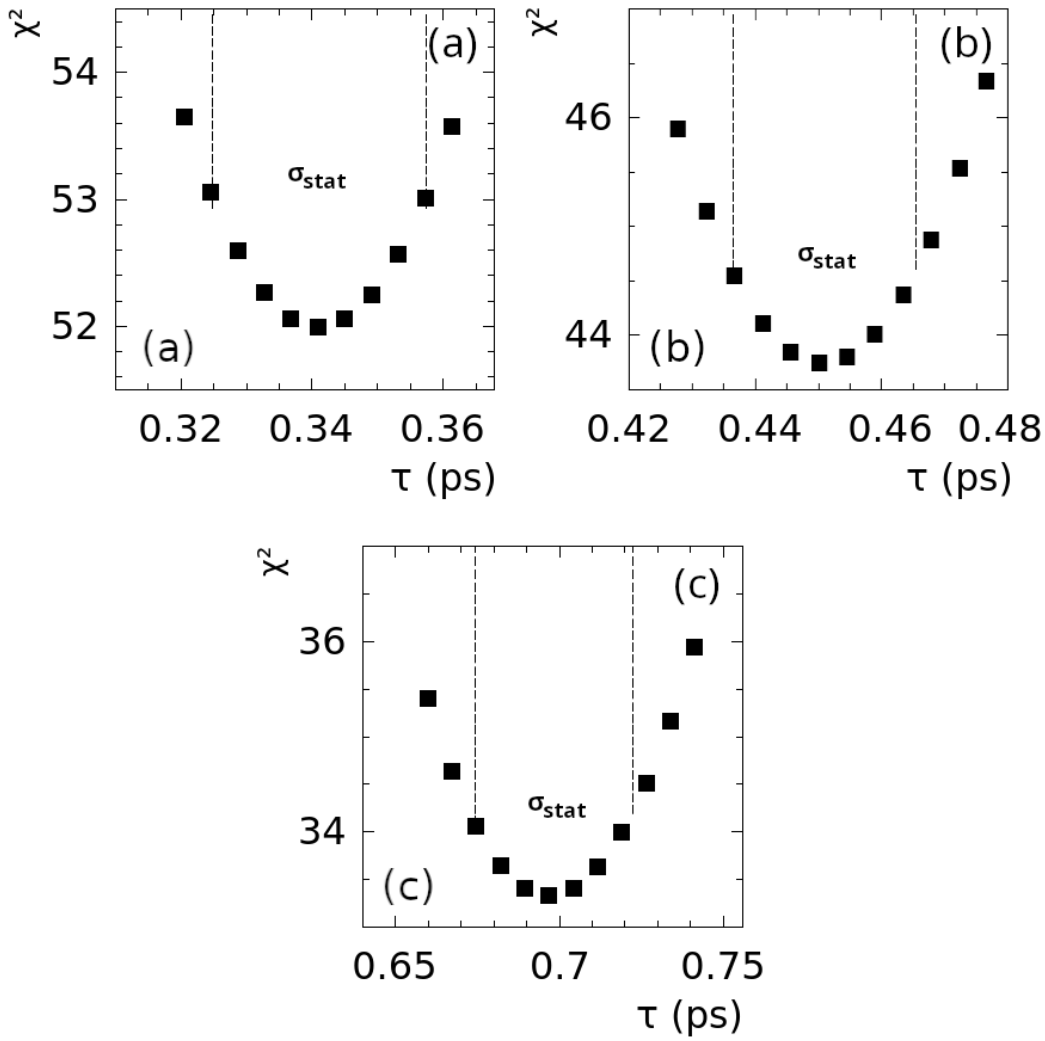

Figure 3.36: χ^2 curves as a function of the lifetime for the gamma-ray transitions of the ^{47}Cr estimated with LINESHAPE. The vertical dashed lines indicates the χ^2_{min} + 1 range. (a) χ^2 curve for the lifetime values of the $(23/2^-)$ state being depopulated by the 1766 keV gamma-ray transition. (b) Same for the lifetime values of the $(19/2^-)$ state being depopulated by the 1485 keV gamma-ray transition. (c) Same for the lifetime values of the $(15/2^-)$ state being depopulated by the 1321 keV gamma-ray transition.

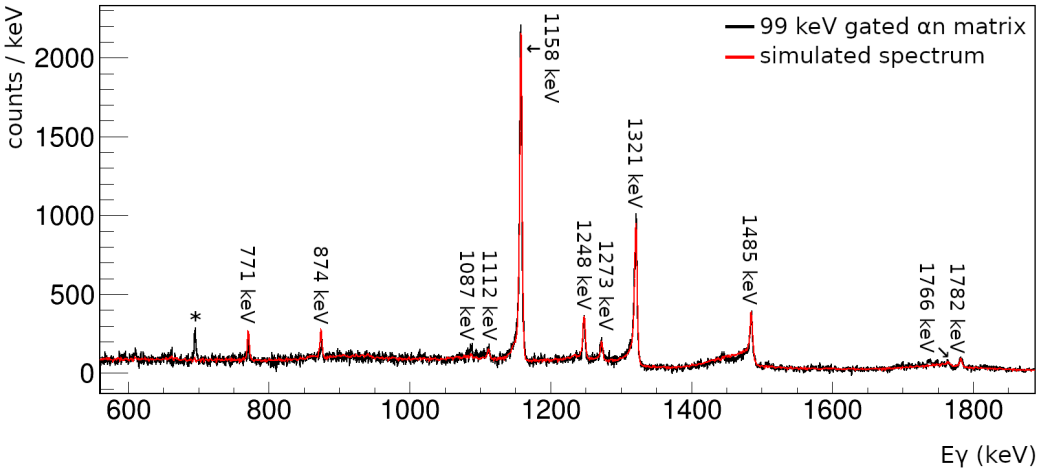

Figure 3.37: Simulated gamma-ray spectrum over the background-subtracted one. The indicated energies correspond to the observed transitions which depopulate excited states in the ^{47}Cr. The (*) symbol corresponds to a contaminant peak.

determined with this method is around ≈ 3 ps. The experimental results obtained with both methods were compiled in Table 3.3. In both methods, the stopped peaks present in the shifted components were included to improve the quality of fit and reduce the χ^2.

In this type of analysis, the lifetime of the highest level in the level scheme with observable gamma-ray transitions needs to be estimated first, as its feeding times affect the shape of the gamma-ray transitions depopulating the lower levels. The lack of knowledge of the feeding transitions for the uppermost level requires the modeling of its feeding patterns, meaning that its lifetime can not be estimated free of systematic errors [68, 87]. Once the lifetime for the uppermost level is determined, it is possible to follow the gamma-ray cascade. The 1766 keV, $(23/2^-) \rightarrow (19/2^-)$, is the uppermost gamma-ray transition observed in the 99 keV gated spectrum. The $(23/2^-)$ level was considered to be fed by a $\tau = 0.2$ ps transition supported by the fact that for the mass region $A < 90$ feeding times faster than that have been reported, as a consequence of the entry states decaying predominantly by dipole transitions to the discrete yrast states [88, 89]. In all cases, the miss-

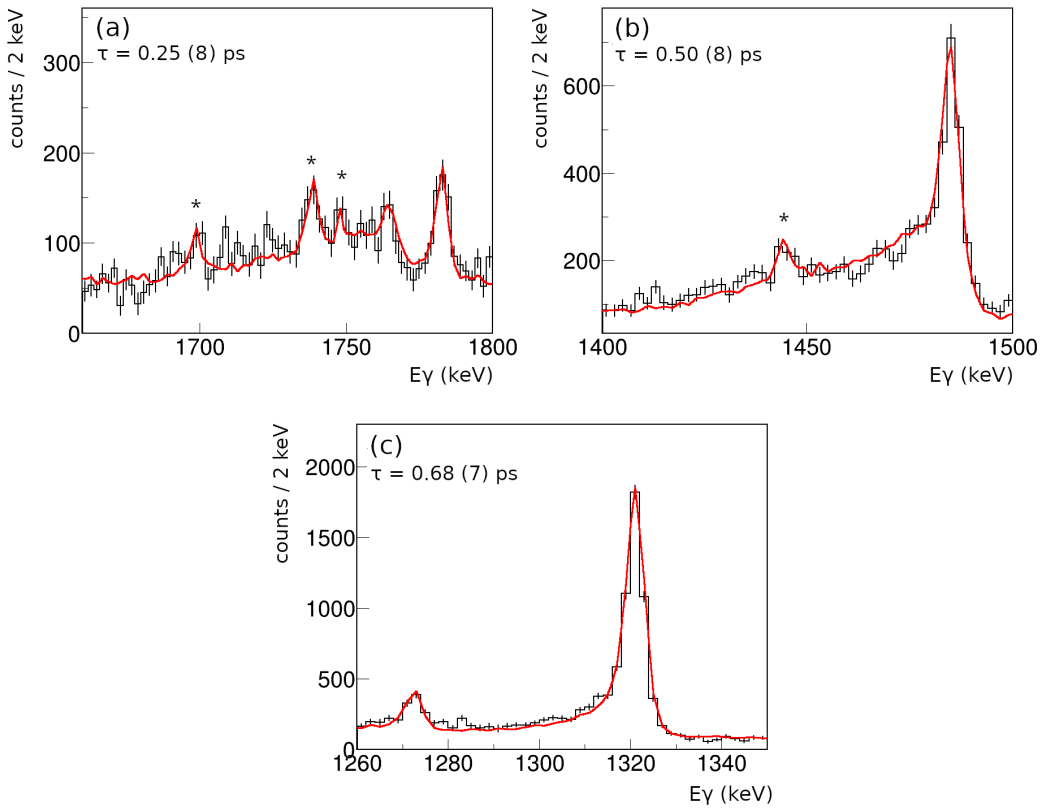

Figure 3.38: (a) Comparison between experimental spectrum and GEANT4 line shape fitted for the 1766 keV gamma-ray transition that depopulates the $(23/2^-)$ state. (b) Same for the 1485 keV gamma-ray transition that depopulates the $(19/2^-)$ state. (c) Same for the 1321 keV gamma-ray transition that depopulates the $(15/2^-)$ state. The symbol (*) indicates the presence of a stopped peak arising from an unidentified transition.

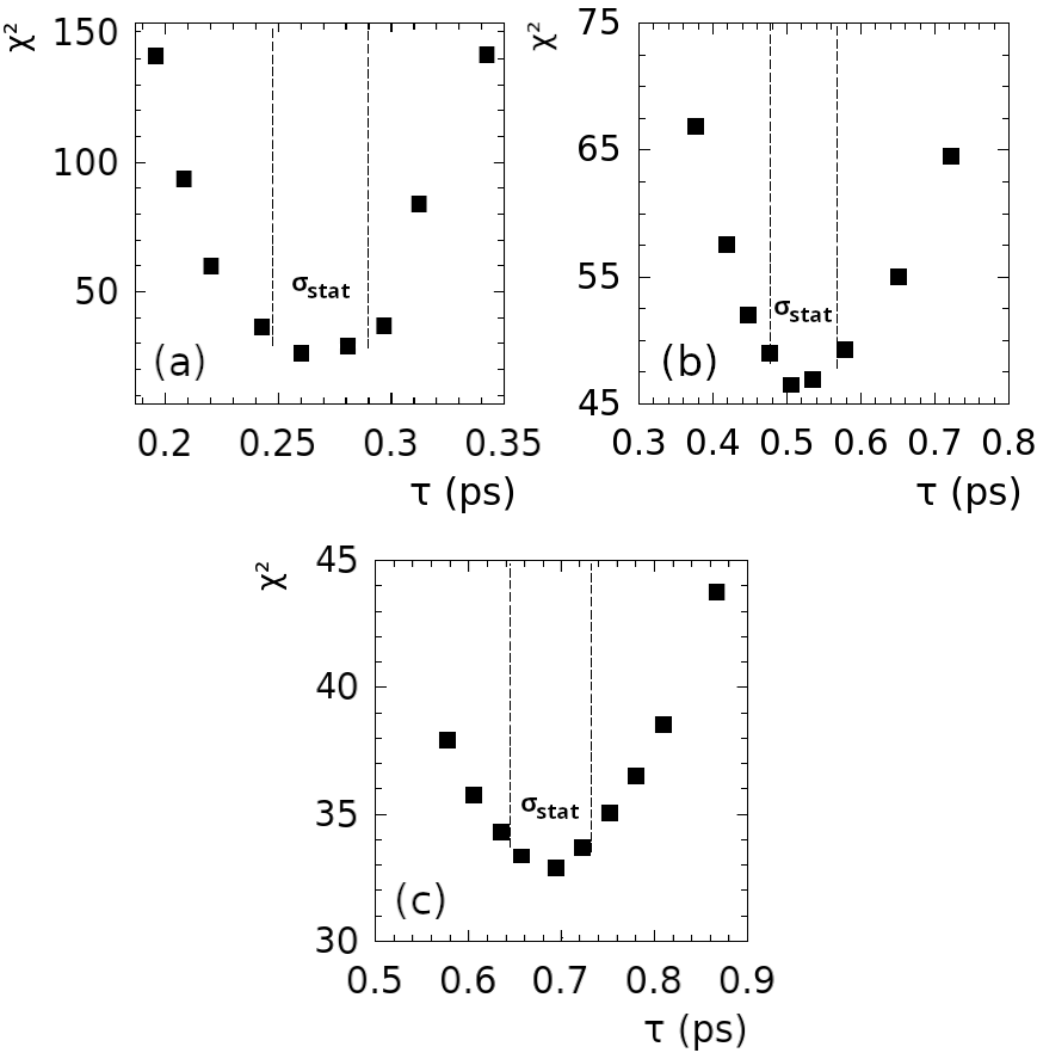

Figure 3.39: χ^2 curves as a function of the lifetime for the gamma-ray transitions of the ^{47}Cr estimated with Geant4. The vertical dashed lines indicates the χ^2_{min} + 1 range. (a) χ^2 curve for the lifetime values of the $(23/2^-)$ state being depopulated by the 1766 keV gamma-ray transition. (b) Same for the lifetime values of the $(19/2^-)$ state being depopulated by the 1485 keV gamma-ray transition. (c) Same curve for the lifetime values of the $(15/2^-)$ state being depopulated by the 1321 keV gamma-ray transition.

Table 3.3: Experimental lifetime values were obtained for the ^{47}Cr using LINESHAPE and GEANT4 set of programs.

Transition	E_γ (keV)	γ-BR (%)	Intensity (a.u.)	$\tau_{exp.}$ (ps) LINESHAPE	$\tau_{exp.}$ (ps) GEANT4	B(E2) (e^2fm^4) LINESHAPE	B(E2) (e^2fm^4) GEANT4
$(7/2^-) \rightarrow (5/2^-)$	75	99[a]	70(3)				
$(11/2^-) \rightarrow (7/2^-)$	1158	100[a]	196(6)	> 3	> 3		
$(15/2^-) \rightarrow (11/2^-)$	1321	100[a]	111(5)	0.70(6)	0.68(7)	289(24)	298(31)
$(17/2^-) \rightarrow (15/2^-)$	1112	100[a]	10				
$(19/2^-) \rightarrow (15/2^-)$	1485	95[a]	113(8)	0.42(6)	0.50(8)	255(38)	214(36)
$(23/2^-) \rightarrow (19/2^-)$	1766	88[a]	52(4)	0.34(4)	0.25(8)	122(14)	167(53)
$(3/2^+) \rightarrow (5/2^+)$	372	15[a]	12(2)				
$(5/2^+) \rightarrow (5/2^-)$	771	7[a]	3(1)				
$(7/2^+) \rightarrow (3/2^+)$	476	50[a]	6(1)	> 3	> 3		
$(7/2^+) \rightarrow (5/2^-)$	1247	25[a]	18(2)				
$(9/2^+) \rightarrow (5/2^+)$	1087	67[a]	1				
$(9/2^+) \rightarrow (7/2^+)$	611	5[a]	2(1)				
$(9/2^+) \rightarrow (7/2^-)$	1782	28[a]	7(1)				
$(11/2^+) \rightarrow (7/2^+)$	1272	74[a]	7(2)				

[a] Ref. [12].

ing gamma-ray intensities were accounted for by including fast side-feeding transitions (< 0.1 ps). Such side-feeding contribution could be avoided if gates from above could be performed. However, due to the presence of contaminants in the gamma-gamma matrix, gating from above was not possible with the present data set, resulting in higher uncertainties in the lifetime values.

3.5.2 The lifetime of ^{49}Mn excited states

The same procedures adopted for the ^{47}Cr were applied to determine the lifetimes of excited states in the ^{49}Mn. This nucleus is the 2np exit channel produced in the fusion-evaporation reaction ^{36}Ar + ^{16}O, and was predicted to be weakly populated in the reaction, around 0.9 mb cross-section according to PACE simulations. It would be possible to create the level scheme by gating on the transitions in the 2np gamma-gamma matrix and observing coincident gamma rays. However, it was not possible to perform multiple gates for such a scarcely populated nucleus, the spin assignment and the order of the levels in the level scheme were taken from the literature [13]. To increase the number of events, it was possible to sum the events from the 2n and 2np background-subtracted spectra, after gating on the lowermost transition of the ^{49}Mn, 262 keV ($7/2^{(-)} \rightarrow 5/2^{-}$). The contamination of ^{49}Cr was subtracted from the resulting spectrum by gating in the same 262 keV energy in the 2pn matrix, and scaling the resulting spectrum down until it matches to observed contamination. The final spectrum used to estimate the lifetime of 4 excited states in the ^{49}Mn is shown in Figure 3.40. The experimental values for the gamma-ray energies found in the present work are shown in the level scheme shown in Figure 3.41.

Lifetimes of excited states of the ^{49}Mn in the sub-picosecond range were determined using both the LINESHAPE and GEANT4 set of programs. As in the case of ^{47}Cr, the lifetime estimation procedure started with the LINESHAPE package, and the fits performed with the package are shown in Figure 3.42. The values of lifetime obtained using the LINESHAPE set of programs

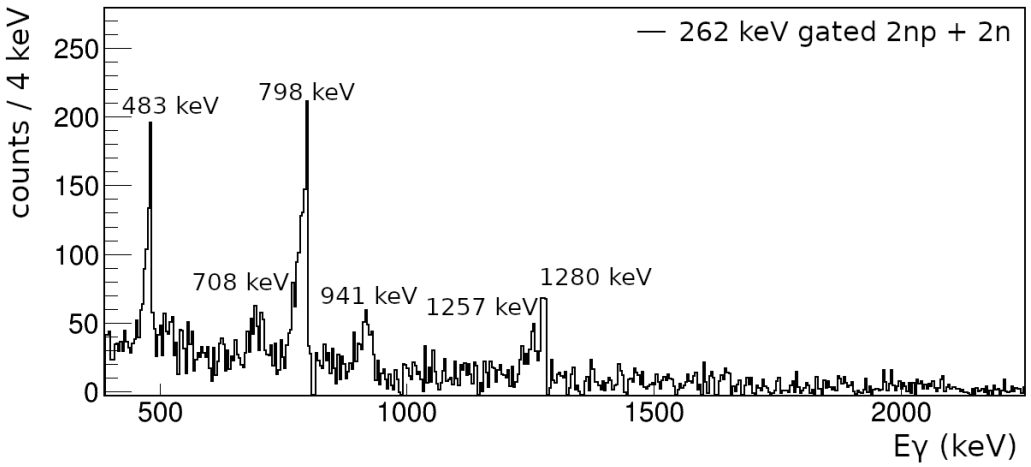

Figure 3.40: Background subtracted gamma-ray spectrum produced by gating on the 262 keV ($7/2^{(-)} \rightarrow 5/2^{-}$) gamma-ray transition in the (2np + 2n)-restricted gamma-gamma matrix. The indicated energies correspond to the observed transitions which depopulate excited states in the ^{49}Mn.

were also used as initial values for the grid-search algorithm performed by GEANT4, and the simulated spectrum with the obtained lifetimes can be observed in figure 3.43. The χ^2 as a function of level lifetimes are shown in Figures 3.44 and 3.45 for LINESHAPE and GEANT4, respectively. The uncertainty estimation procedure for the statistical and systematic components followed the same steps presented in the case of the ^{47}Cr.

The lifetime of the $15/2^{(-)}$ excited state was estimated using the line shape of the 708 keV gamma-ray, as it is the uppermost observed gamma-ray from which an excited state lifetime can be estimated. The resulting curve of both sets of programs was able to reproduce the observed shape for the 708 keV gamma-ray transition, as can be observed in Figures 3.42a and 3.43a. The observed 941 keV gamma-ray transition, depopulating the $13/2^{(-)}$ state, presents an unusual shape in the gamma-ray spectrum. Such a shape arises from the subtraction of the contaminating transition from the ^{49}Cr, causing a shortage of events in the 910 keV energy channel. This unusual shape caused both methods to fail in finding a minimum χ^2 value to the lifetime of the $13/2^{(-)}$, for this reason, the best curve for the 941 keV line shape was

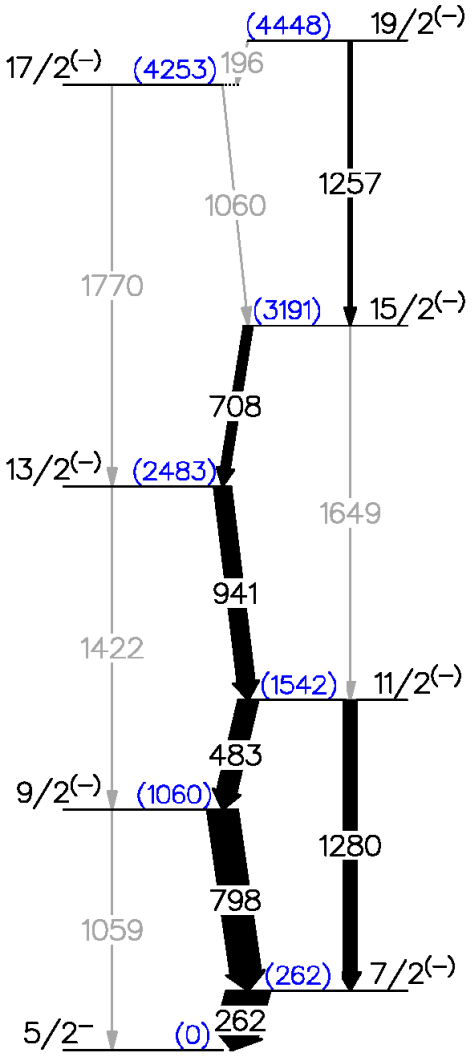

Figure 3.41: Partial level scheme for the ^{49}Mn with the gamma-ray energies found in the present work. The arrow's width is proportional to the intensities.

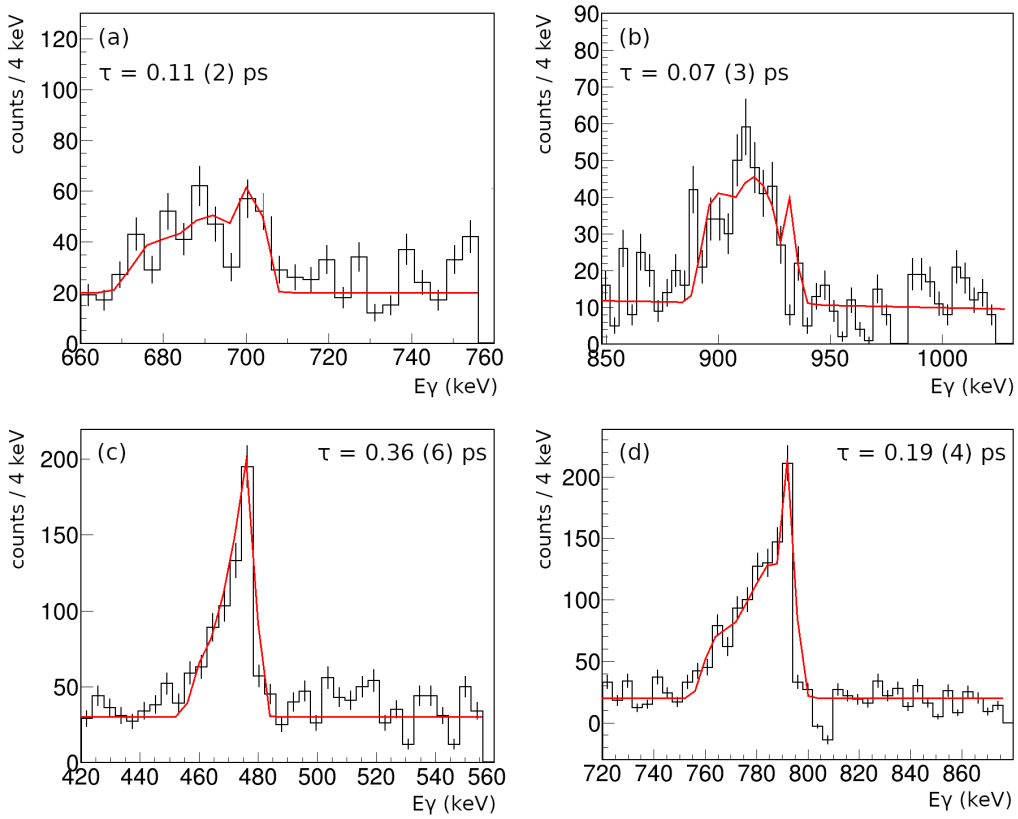

Figure 3.42: (a) LINESHAPE fitted for the 708 keV gamma-ray transition that depopulates the $15/2^{(-)}$ state. (b) Same for the 941 keV gamma-ray transition that depopulates the $13/2^{(-)}$ state. (c) Same for the 483 keV gamma-ray transition that depopulates the $11/2^{(-)}$ state. (d) Same for the 798 keV gamma-ray transition that depopulates the $9/2^{(-)}$ state.

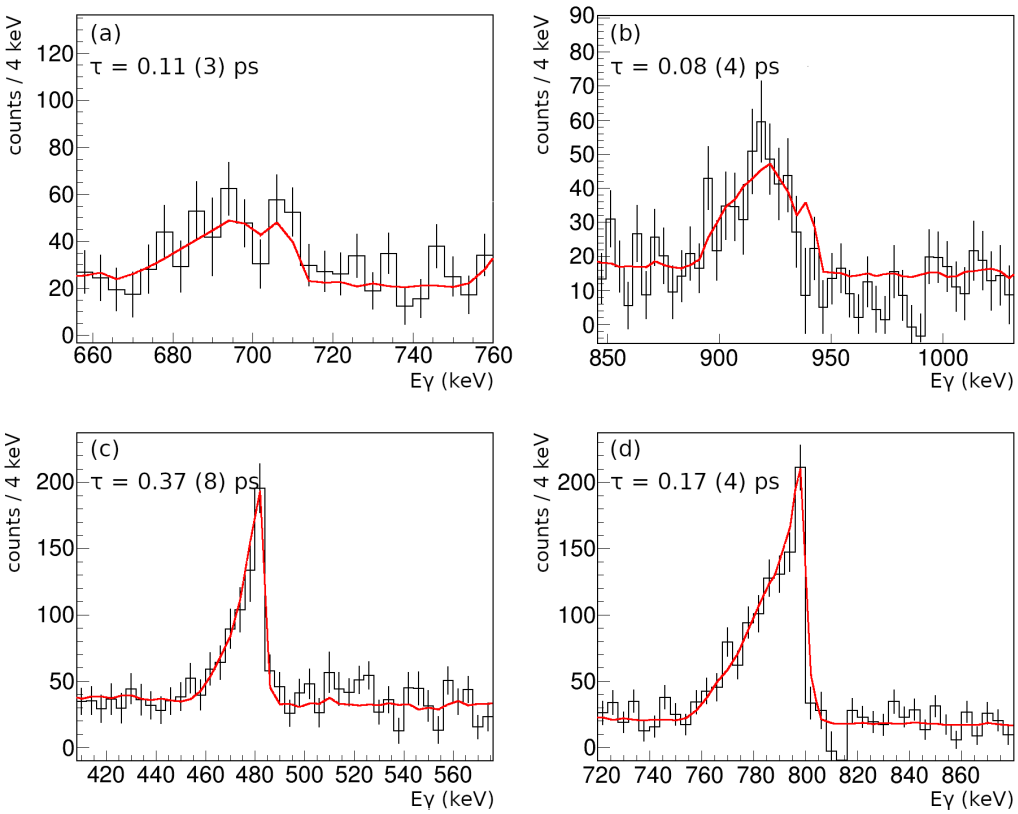

Figure 3.43: (a) GEANT4 fitted for the 708 keV gamma-ray transition that depopulates the $15/2^{(-)}$ state. (b) Same for the 941 keV gamma-ray transition that depopulates the $13/2^{(-)}$ state. (c) Same for the 483 keV gamma-ray transition that depopulates the $11/2^{(-)}$ state. (d) Same for the 798 keV gamma-ray transition that depopulates the $9/2^{(-)}$ state.

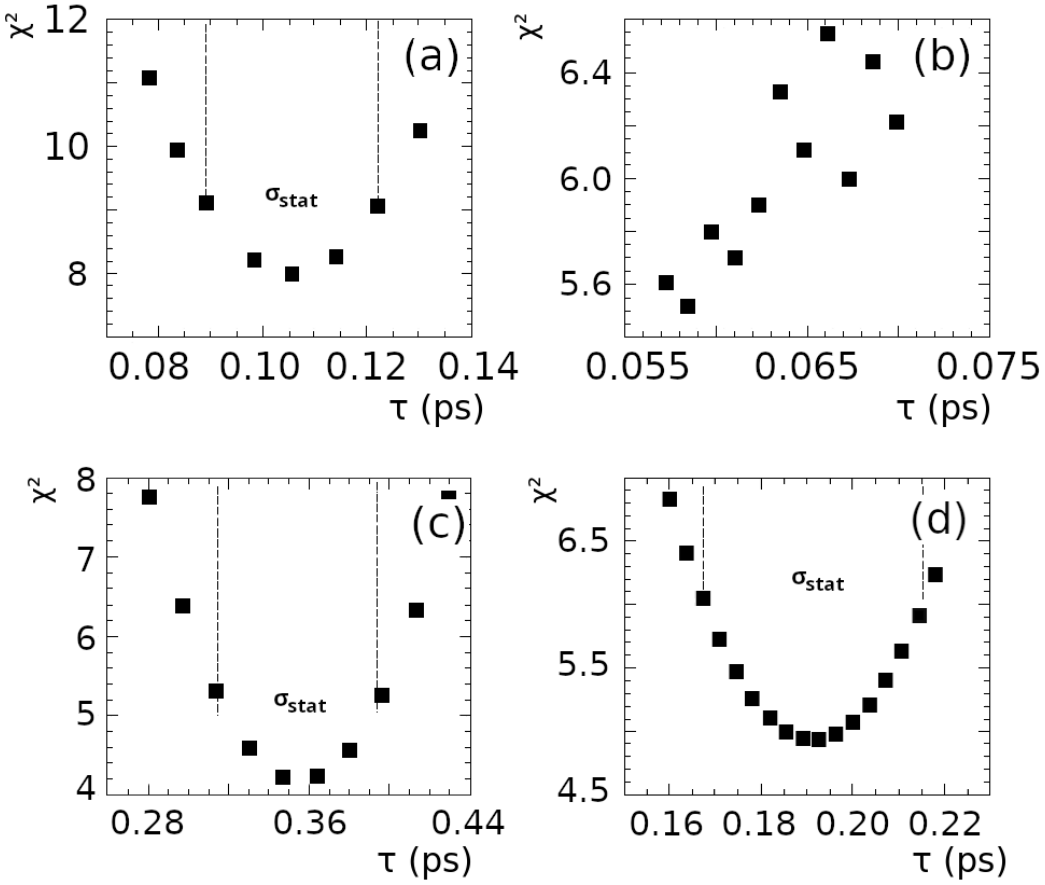

Figure 3.44: χ^2 curves as a function of the lifetime for the gamma-ray transitions of the ^{49}Mn estimated with LINESHAPE. The vertical dashed lines indicates the χ^2_{min} + 1 range. (a) χ^2 curve for the lifetime values of the $15/2^{(-)}$ state being depopulated by the 708 keV gamma-ray transition. (b) Same for the lifetime values of the $13/2^{(-)}$ state being depopulated by the 941 keV gamma-ray transition. (c) Same for the lifetime values of the $11/2^{(-)}$ state being depopulated by the 483 keV gamma-ray transition. (d) Same for the lifetime values of the $9/2^{(-)}$ state being depopulated by the 798 keV gamma-ray transition.

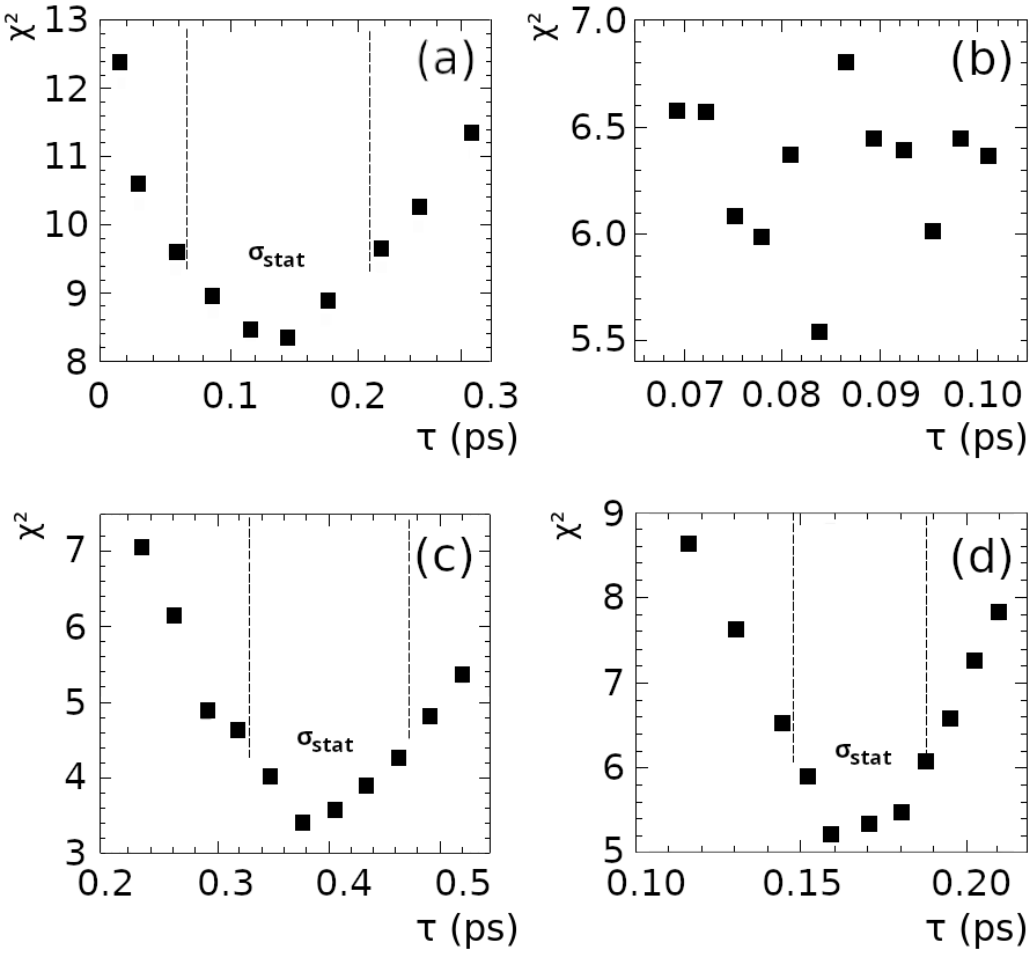

Figure 3.45: χ^2 curves as a function of the lifetime for the gamma-ray transitions of the ^{47}Cr estimated with Geant4. The vertical dashed lines indicates the χ^2_{min} + 1 range. (a) χ^2 curve for the lifetime values of the $15/2^{(-)}$ state being depopulated by the 708 keV gamma-ray transition. (b) Same for the lifetime values of the $13/2^{(-)}$ state being depopulated by the 941 keV gamma-ray transition. (c) Same for the lifetime values of the $11/2^{(-)}$ state being depopulated by the 483 keV gamma-ray transition. (d) Same curve for the lifetime values of the $9/2^{(-)}$ state being depopulated by the 798 keV gamma-ray transition.

determined "by eye". The stopped component in both cases is overestimated as can be observed in Figures 3.42b and 3.43b and it arises from the intensity coming from the level above and thus can not be changed. The lifetime of the $11/2^{(-)}$ excited state was estimated using the line shape of the 483 keV gamma-ray transition, as it is not overlapping with other gamma-rays. The resulting curve of both sets of programs can be observed in Figures 3.42c and 3.43c. The lifetime of the $9/2^{(-)}$ excited state was estimated using the line shape of the 798 keV gamma-ray transition, as it is the most intense gamma-ray depopulating this state. The resulting curve of both sets of programs can be observed in Figures 3.42d and 3.43d. The comparison between the experimental and the best GEANT4 full simulated gamma-ray spectrum is shown in Figure 3.46. The experimental results obtained with both methods

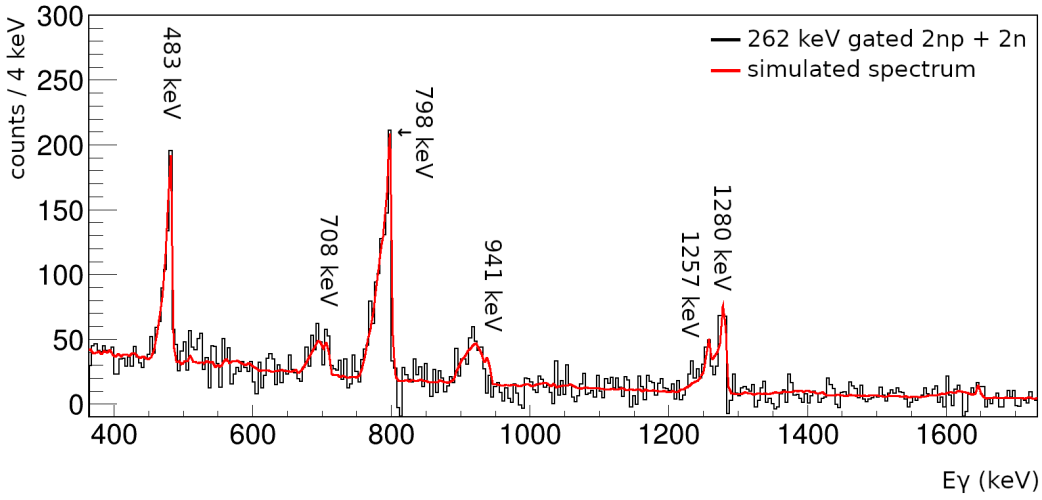

Figure 3.46: GEANT4 simulated gamma-ray spectrum over the background-subtracted one. The indicated energies correspond to the observed transitions which depopulate excited states in the ^{49}Mn.

were compiled in Table 3.4. The value of lifetime for the $19/2^{(-)}$ was manually included as a side-feeding contribution to reproduce the stopped component of the 708 keV gamma-ray depopulating the $15/2^{(-)}$ state.

Table 3.4: Experimental lifetime values obtained for the ^{49}Mn using LINESHAPE and GEANT4 set of programs.

Transition	E_γ (keV)	γ-BR (%)	Intensity (a.u.)	$\tau_{exp.}$ (ps) LINESHAPE	$\tau_{exp.}$ (ps) GEANT4	B(E2) (e^{2}fm^4) LINESHAPE	B(E2) (e^2fm^4) GEANT4
$9/2^{(-)} \rightarrow 5/2^{(-)}$	1059[a]	8[a]	-	0.19(4)	0.17(4)	265(64)	296(50)
$9/2^{(-)} \rightarrow 7/2^{(-)}$	798	92[a]	124(15)				
$11/2^{(-)} \rightarrow 7/2^{(-)}$	1280	50[a]	57(17)	0.36(6)	0.37(8)	327(64)	318(68)
$11/2^{(-)} \rightarrow 9/2^{(-)}$	483	50[a]	80(14)				
$13/2^{(-)} \rightarrow 9/2^{(-)}$	1422[a]	17[a]	-	0.07(2)	0.08(4)	335(138)	293(141)
$13/2^{(-)} \rightarrow 11/2^{(-)}$	941	83[a]	69(17)				
$15/2^{(-)} \rightarrow 11/2^{(-)}$	1649[a]	41[a]	-	0.11(2)	0.11(3)	246(58)	246(76)
$15/2^{(-)} \rightarrow 13/2^{(-)}$	708	59[a]	36(9)				
$19/2^{(-)} \rightarrow 15/2^{(-)}$	1257	89[a]	11(8)	2.15	2.09	111(9)	129(9)

[a] Ref. [13].

3.5.3 The Lifetime of ^{47}V excited states

To ensure the reliability of the methods adopted to obtain the lifetimes of the ^{47}Cr and ^{49}Mn, the same procedures using LINESHAPE and GEANT4 were applied to estimate the lifetime of excited states of the ^{47}V and ^{49}Cr. These nuclei are the strongest populated channels in the fusion-evaporation reaction ^{36}Ar + ^{16}O, with a predicted cross-section of 150 mb and 350 mb, respectively, according to PACE calculations. The number of events presented by these channels would allow procedures like gating on the transition above (GTA) and the narrow gate on the transition bellow (NGTB) to be performed, obtaining the lifetimes without the side feeding contribution to the uncertainty. However, the lifetimes of excited states of the ^{47}V and ^{49}Cr nuclei are well-known and these different techniques would not be useful to validate the procedure adopted for the ^{47}V and ^{49}Mn. For this reason, a gate in the lowermost transition of the ^{47}V, 88 keV ($5/2^- \rightarrow 3/2^-$), was performed, and the lifetimes of excited states of the ^{47}V in the sub-picosecond range were determined to validate the GEANT4 procedure. The LINESHAPE procedure

could not be applied for this channel due to its complex and overlapping level scheme pattern when gating from a transition below. The adopted level scheme is shown in Figure 3.47. The final spectrum used to estimate the lifetime of the excited states in the ^{47}V is shown in Figure 3.48. The values of lifetime found in the literature were used as initial values for the grid-search algorithm performed by GEANT4, and the simulated spectrum with the obtained lifetimes can be observed in figure 3.49.

The uncertainty estimation procedure for the statistical and systematic components followed the same steps presented in the cases of the ^{47}Cr and ^{49}Mn. However, it is important to point out that due to the high number of events of the ^{47}V gamma-ray transitions, the statistical contribution is much smaller than the systematic one. The χ^2 as a function of level lifetimes are shown in Figure 3.50.

The lifetime of the $23/2^-$ excited state was estimated using the line shape of the 1770 keV gamma-ray, as it is the uppermost observed gamma-ray from which an excited state lifetime can be estimated with the present data. However, the obtained lifetime value can be biased due to the manual insertion of two overlapping transitions of the ^{47}V, 1728 keV ($17/2^+ \rightarrow 13/2^+$), and 1774 keV ($(19/2^+) \rightarrow 15/2^+$) using fixed literature values. The lifetime of the $19/2^-$ excited state was estimated using the line shape of the 1518 keV gamma-ray transition, the agreement between experimental and simulation can be observed in Figure 3.49b. The lifetime of the $15/2^-$ excited state was estimated using the line shape of the 1320 keV gamma-ray transition and can be observed alongside a fit for the state $11/2^+$ depopulated by the 1276 keV gamma-ray for which the lifetime was estimated using the 668 keV gamma-ray transition observable in Figure 3.49f. The lifetime of the $11/2^-$ excited state was estimated using the line shape of the 1149 keV gamma-ray transition, the resulting curve can be observed in Figures and 3.49d. The lifetime of the $9/2^+$ excited state was estimated using the line shape of the 1602 keV gamma-ray transition, as it is not overlapping with other gamma-ray peaks, and the resulting curve can be observed in Figures 3.49e. The

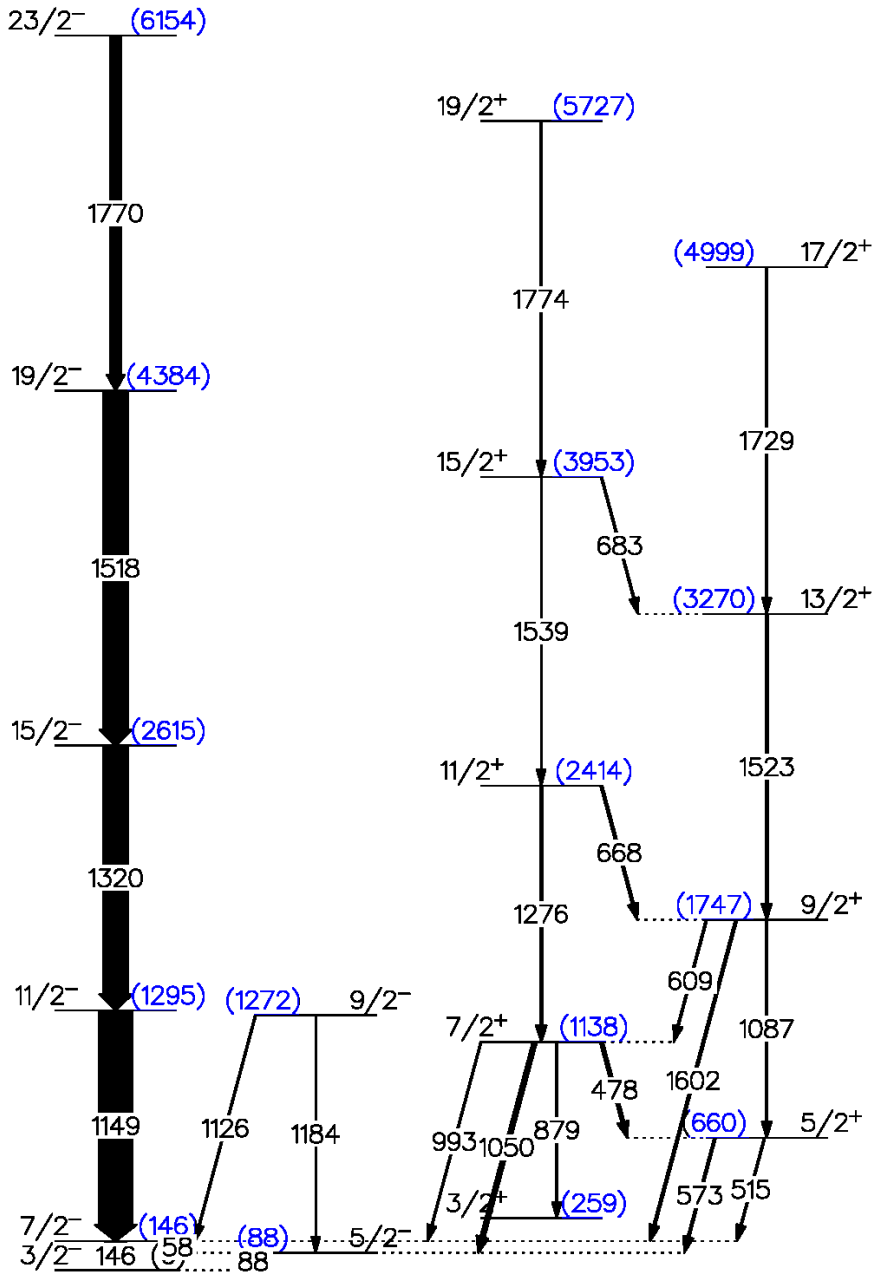

Figure 3.47: Partial level scheme for the ^{47}V with the gamma-ray energies found in the present work. The arrow's width is proportional to the intensities.

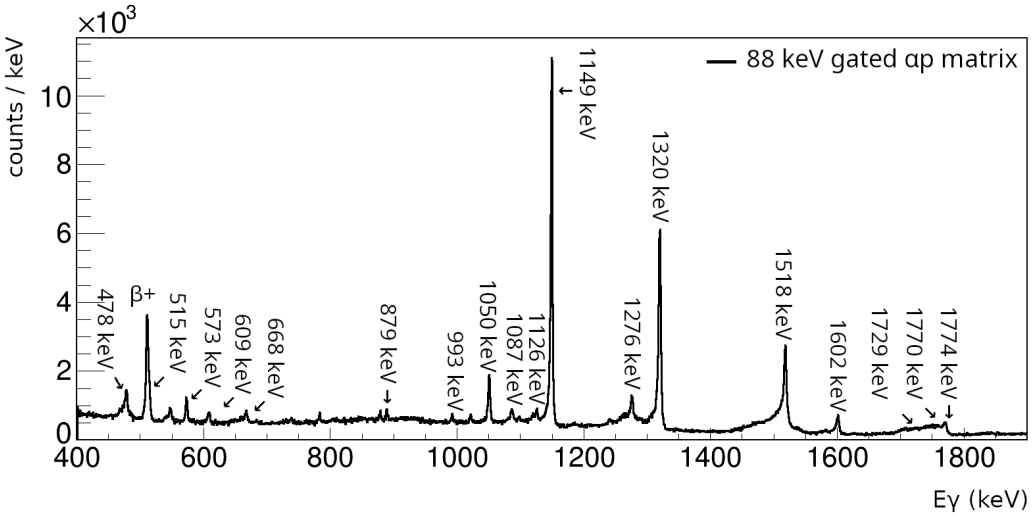

Figure 3.48: Background subtracted gamma-ray spectrum produced by gating on the 88 keV ($5/2^- \rightarrow 3/2^-$) gamma-ray transition in the αp-restricted gamma-gamma matrix. The indicated energies correspond to the observed transitions which depopulate excited states in the ^{47}V.

lifetime of the $11/2^+$ excited state was estimated using the line shape of the 668 keV gamma-ray transition, the resulting curve can be observed in Figure 3.49f. The comparison between the experimental and the best GEANT4 full simulated gamma-ray spectrum is shown in Figure 3.51. The experimental results obtained were compiled in Table 3.5.

3.5.4 The Lifetime of ^{49}Cr excited states

In order to validate the methods used for lifetime estimation, the procedures using both LINESHAPE and GEANT4 were applied to estimate the lifetime of excited states of the ^{49}Cr. To apply the same type of procedure for the low statistics channels, a gate in the lowermost transition of the ^{49}Cr, 272 keV ($7/2^- \rightarrow 5/2^-$), was performed, and the lifetimes of excited states of the ^{49}Cr in the sub-picosecond range were determined using both the LINESHAPE and GEANT4 set of programs. The adopted level scheme is shown in Figure 3.52. The final spectrum used to estimate the lifetime of the excited states in the ^{49}Cr is shown in Figure 3.53. As in the case of ^{47}Cr and

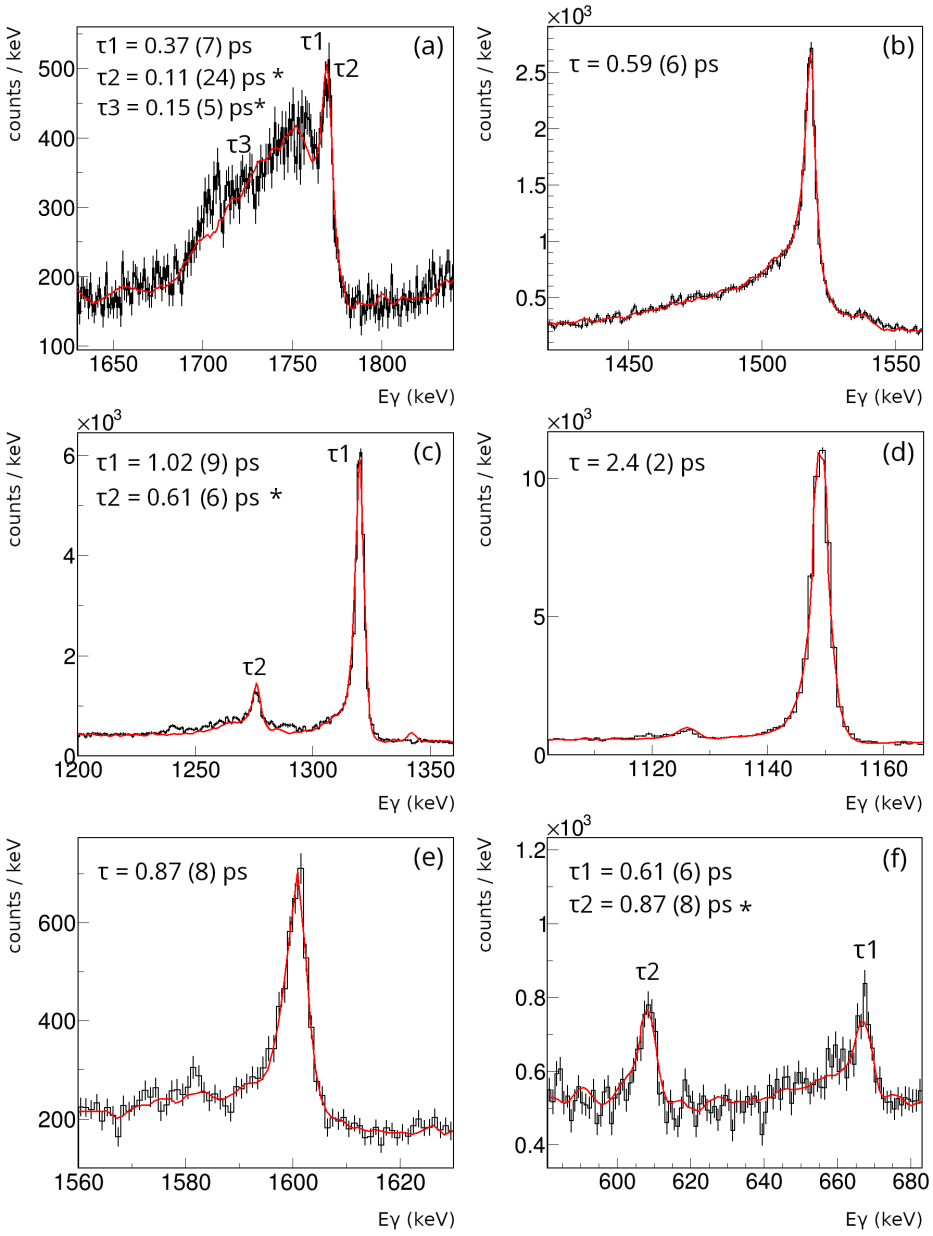

Figure 3.49: (a) GEANT4 fitted for the 1770 keV gamma-ray transition overlapping with the 1774 and 1729 keV gamma-rays, depopulating the $23/2^-$, $19/2^+$ and $17/2^+$ states, respectively. (b) Same for the 1518 keV gamma-ray transition that depopulates the $19/2^-$ state. (c) Same for the 1320 keV gamma-ray transition that depopulates the $15/2^-$ state and the 1276 keV gamma-ray transition that depopulates the $11/2^+$. (d) Same for the 1149 keV gamma-ray transition that depopulates the $11/2^-$ state. (e) Same for the 1602 keV gamma-ray transition that depopulates the $9/2^+$ state. (f) Same for the 668 keV gamma-ray transition that depopulates the $11/2^+$ state and the 609 keV gamma-ray transition that depopulates the $9/2^+$ state. The (*) symbol indicates that the lifetime was estimated with another transition depopulating the same state.

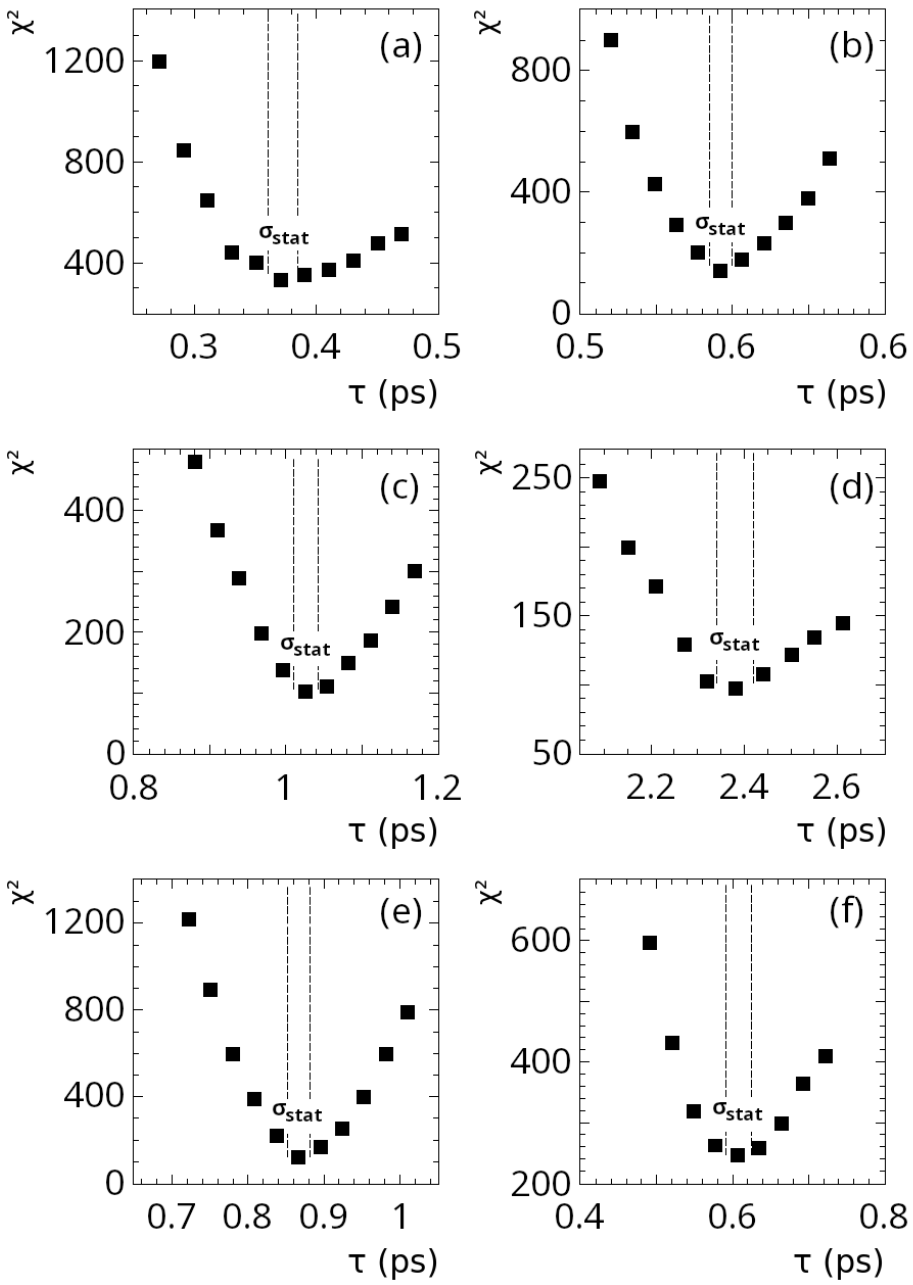

Figure 3.50: χ^2 curves as a function of the lifetime for the gamma-ray transitions of the ^{47}Cr estimated with Geant4. The vertical dashed lines indicates the χ^2_{min} + 1 range. (a) χ^2 curve for the lifetime values of the $23/2^-$ state being depopulated by the 1770 keV gamma-ray transition. (b) Same for the lifetime values of the $19/2^-$ state being depopulated by the 1518 keV gamma-ray transition. (c) Same for the lifetime values of the $15/2^-$ state being depopulated by the 1320 keV gamma-ray transition. (d) Same for the lifetime values of the $11/2^-$ state being depopulated by the 1149 keV gamma-ray transition. (e) Same for the lifetime values of the $9/2^+$ state being depopulated by the 1602 keV. (f) Same for the lifetime values of the $11/2^+$ state being depopulated by the 668 keV.

Table 3.5: Experimental lifetime values were obtained for the ^{47}V using GEANT4 set of programs.

Transition	E_γ (keV)	γ-BR (%)	Intensity (a.u.)	$\tau_{exp.}$ (ps)	B(E2) (e^2fm^4)
$7/2^- \rightarrow 5/2^+$	477	25.0(5)[a]	75(9)		
$9/2^- \rightarrow 7/2^-$	1126	81.8(1)[a]	46(9)		
$11/2^- \rightarrow 7/2^-$	1149	100[a]	833(7)	2.4(2)	169(15)
$15/2^- \rightarrow 11/2^-$	1320	99.6(6)[a]	614(26)	1.02(9)	198(18)
$19/2^- \rightarrow 15/2^-$	1518	100[a]	852(60)	0.59(6)	171(17)
$(23/2^-) \rightarrow 19/2^-$	1770	100[a]	358(42)	0.37(7)	127(24)
$5/2^+ \rightarrow 5/2^-$	573	14.1(3)[a]	32(8)		
$7/2^+ \rightarrow 3/2^+$	879	32.5(4)[a]	26(9)		
$7/2^+ \rightarrow 7/2^-$	992	4.4(2)[a]	24(11)		
$7/2^+ \rightarrow 5/2^-$	1050	38.0(4)[a]	102(19)		
$9/2^+ \rightarrow 5/2^+$	1086	46(1)[a]	39(11)		286(27)
$9/2^+ \rightarrow 7/2^+$	608	17(1)[a]	32(5)	0.87(8)	
$9/2^+ \rightarrow 7/2^-$	1601	36(2)[a]	67(9)		
$11/2^+ \rightarrow 7/2^+$	1276	86(1)[a]	146(37)	0.61(6)	43(6)
$11/2^+ \rightarrow 9/2^+$	667	11(1)[a]	58(15)		

[a] Ref. [90].

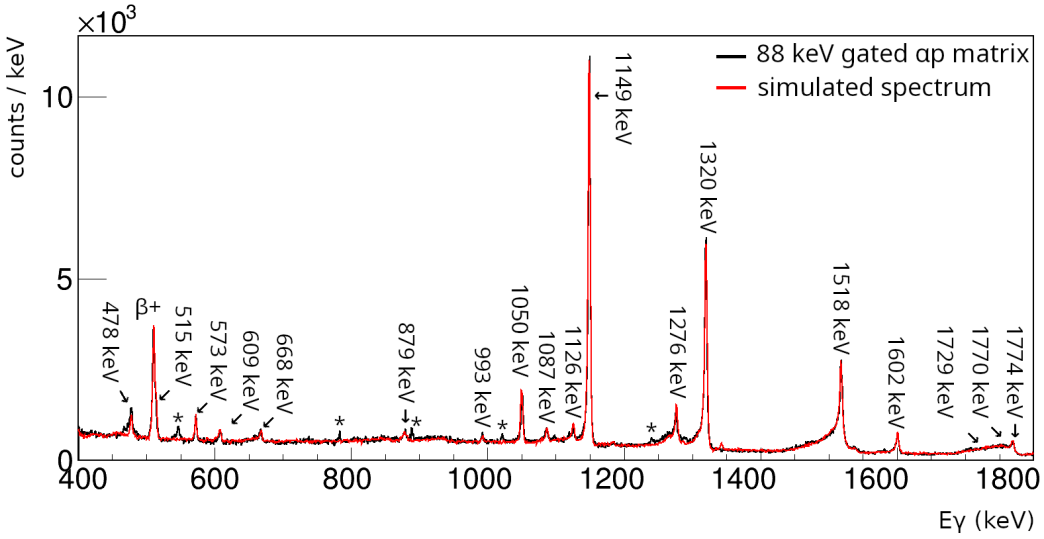

Figure 3.51: GEANT4 simulated gamma-ray spectrum over the background-subtracted one. The indicated energies correspond to the observed transitions which depopulate excited states in the ^{47}V. The (*) symbol corresponds to contaminant peaks.

^{49}Mn, the lifetime estimation procedure started with the LINESHAPE package, and the fits performed with the package are shown in Figure 3.54. The values of lifetime obtained using the LINESHAPE set of programs were also used as initial values for the grid-search algorithm performed by GEANT4, and the simulated spectrum with the obtained lifetimes can be observed in figure 3.55. The uncertainty estimation procedure for the statistical and systematic components followed the same steps presented in the cases of the ^{47}Cr and ^{49}Mn. However, it is important to point out that due to the high number of events of the ^{49}Cr gamma-ray transitions, the statistical contribution is much smaller than the systematic one. The χ^2 as a function of level lifetimes are shown in Figures 3.56 and 3.57 for LINESHAPE and GEANT4, respectively.

The lifetime of the $23/2^-$ excited state was estimated using the line shape of the 1596 keV gamma-ray, as it is the uppermost observed gamma-ray from which an excited state lifetime can be estimated. However, due to the presence of the overlapping 1628 keV gamma-ray transition, which depopulates

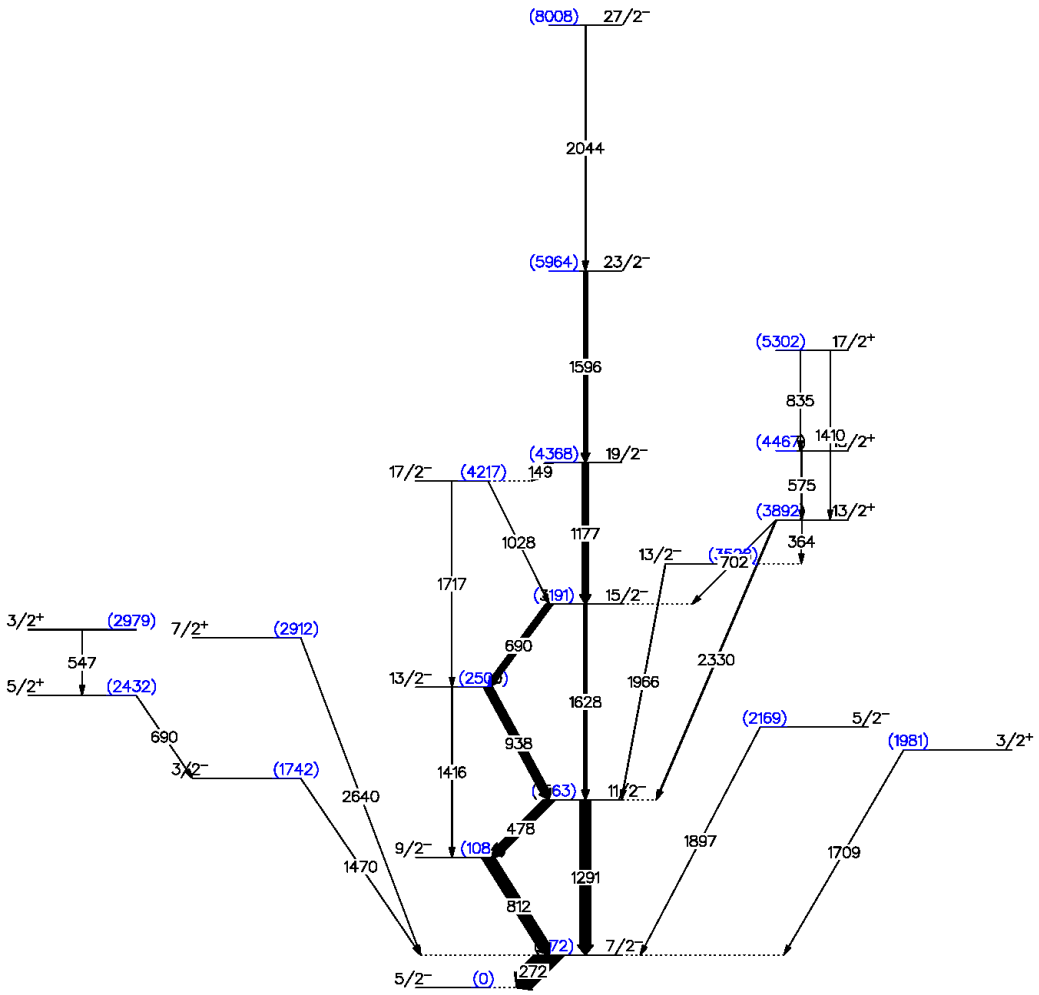

Figure 3.52: Partial level scheme for the ^{49}Cr. The arrow's width is proportional to the intensities of the transitions.

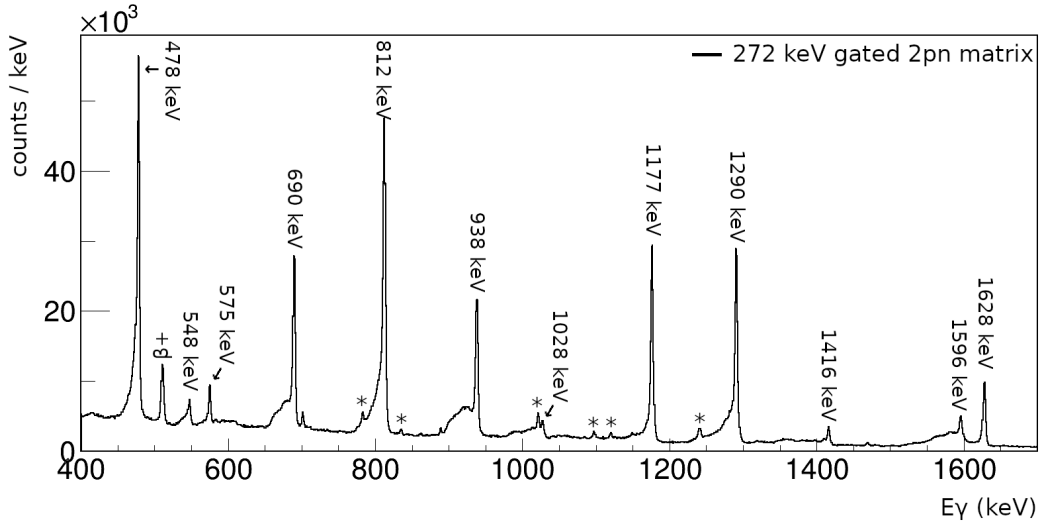

Figure 3.53: Background subtracted gamma-ray spectrum produced by gating on the 272 keV ($7/2^- \rightarrow 5/2^-$) gamma-ray transition in the 2pn-restricted gamma-gamma matrix.

the $15/2^-$ state, the minimum χ^2 method presented some limitations. Therefore the known value from the literature was assigned as the lifetime for the $23/2^-$ excited state, while the lifetime of the $15/2^-$ state was determined using the 690 keV gamma-ray transition. The resulting curve of both sets of programs was an acceptable enough reproduction of the observed experimental shape, as can be observed in Figures 3.54a and 3.55a. The lifetime of the $19/2^-$ excited state was estimated using the line shape of the 1177 keV gamma-ray transition, the obtained lifetime is at the limit of what can be measured with the DSAM technique. The better agreement of the GEANT4 fit with the peak left tail can be a consequence of the included better detector response function, which includes the neutron damage. The lifetime of the $15/2^-$ excited state was estimated using the line shape of the 690 keV gamma-ray transition, as it is not overlapping with other ^{49}Cr gamma-ray transitions. and the resulting curve of both sets of programs can be observed in Figures 3.54c and 3.55c, where a good agreement was achieved. The lifetime of the $13/2^-$ excited state was estimated using the line shape of the 938 keV gamma-ray transition, as it is the strongest transition depopulating the

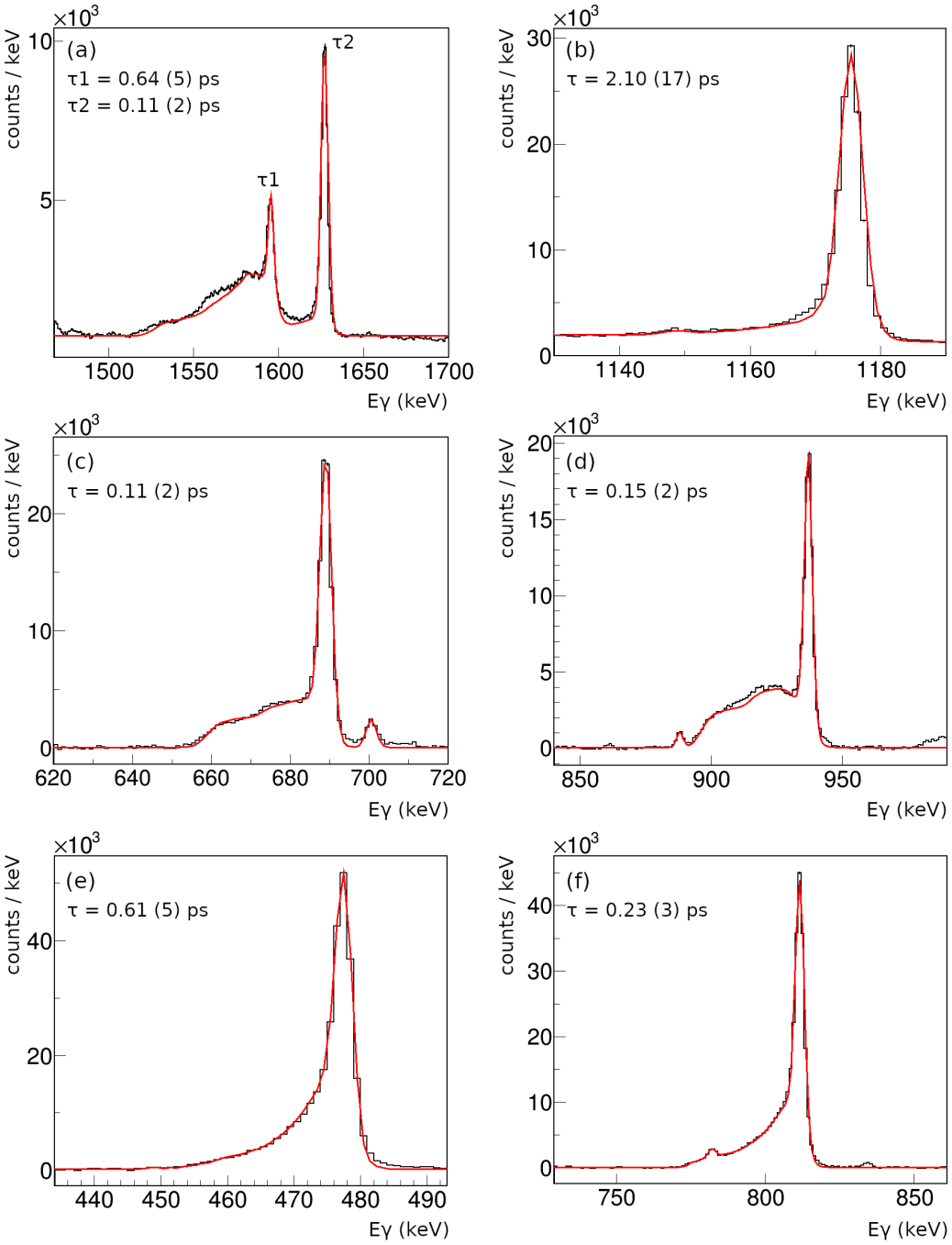

Figure 3.54: (a) LINESHAPE fitted for the 1596 keV gamma-ray transition overlapping with the 1628 keV gamma-ray, depopulating the $23/2^-$ and $15/2^-$ state, respectively. (b) Same for the 1177 keV gamma-ray transition that depopulates the $19/2^-$ state. (c) Same for the 690 keV gamma-ray transition that depopulates the $15/2^-$ state. (d) Same for the 938 keV gamma-ray transition that depopulates the $13/2^-$ state. (e) Same for the 478 keV gamma-ray transition that depopulates the $11/2^-$ state. (f) Same for the 812 keV gamma-ray transition that depopulates the $9/2^-$ state.

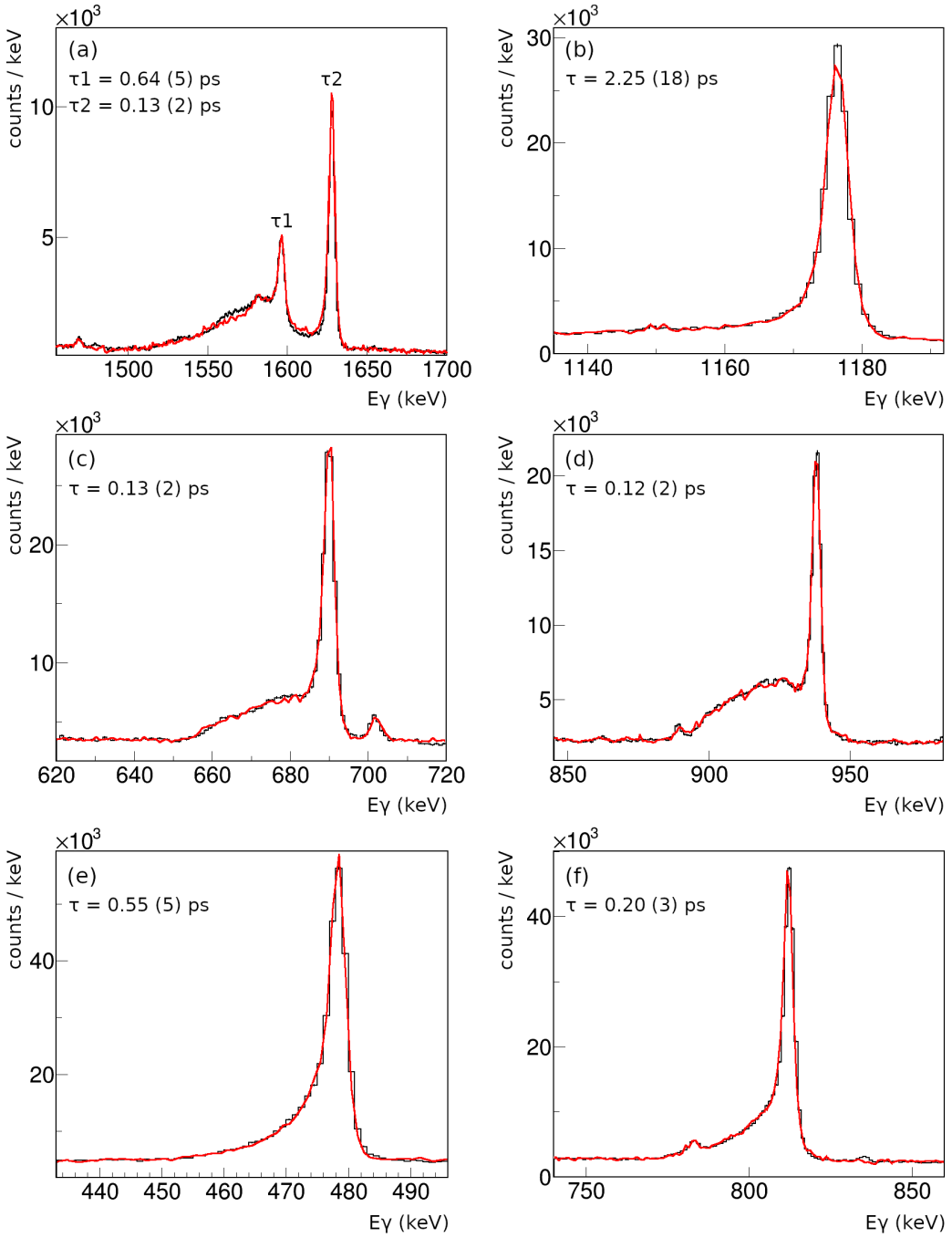

Figure 3.55: (a) GEANT4 fitted for the 1596 keV gamma-ray transition overlapping with the 1628 keV gamma-ray, depopulating the $23/2^-$ and $15/2^-$ state, respectively. (b) Same for the 1177 keV gamma-ray transition that depopulates the $19/2^-$ state. (c) Same for the 690 keV gamma-ray transition that depopulates the $15/2^-$ state. (d) Same for the 938 keV gamma-ray transition that depopulates the $13/2^-$ state. (e) Same for the 478 keV gamma-ray transition that depopulates the $11/2^-$ state. (f) Same for the 812 keV gamma-ray transition that depopulates the $9/2^-$ state.

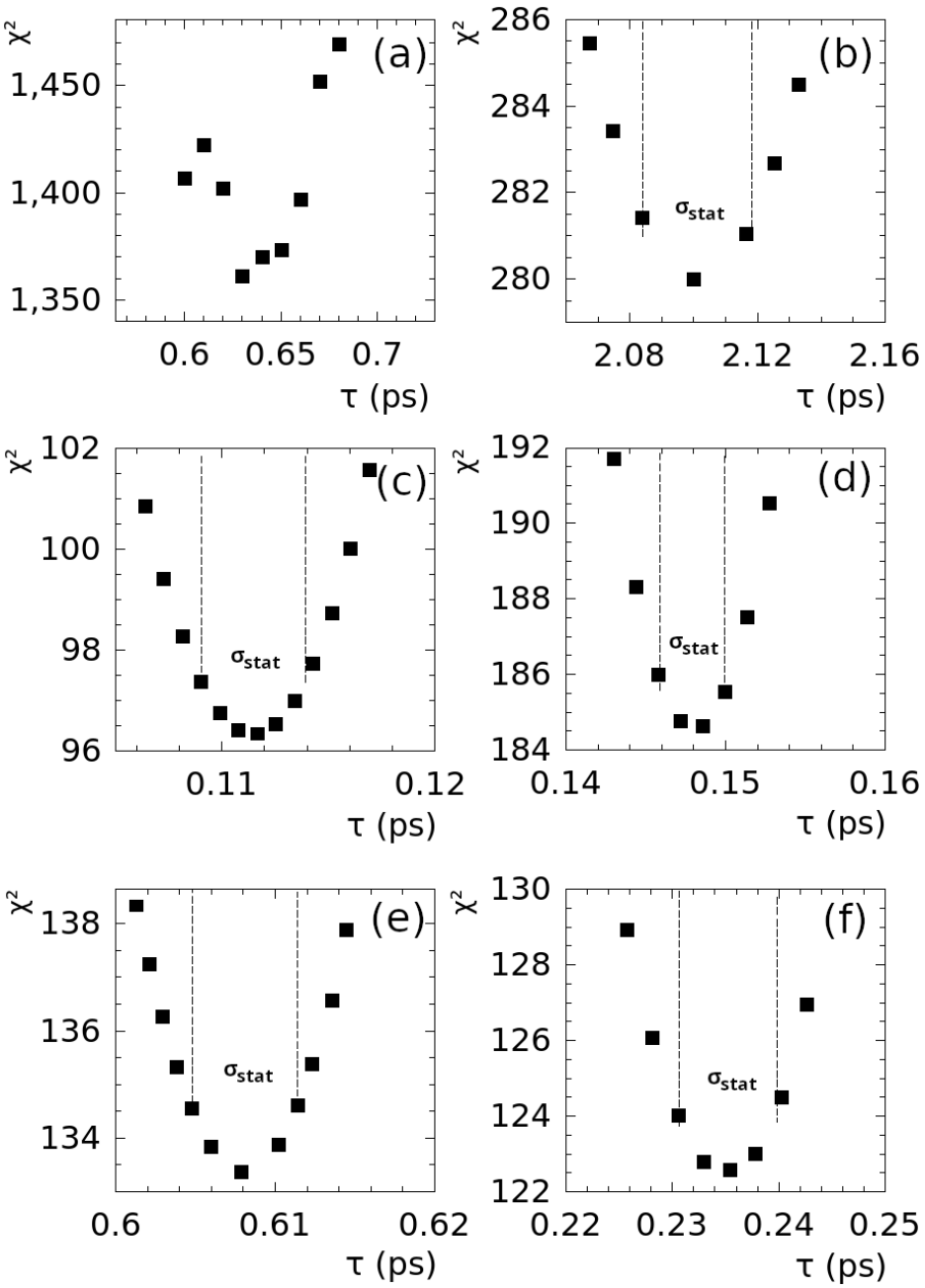

Figure 3.56: χ^2 curves as a function of the lifetime estimated with LINESHAPE for the ^{49}Cr. (a) χ^2 curve for the lifetime values of the $23/2^-$ and $15/2^-$ states being depopulated by the 1596 keV and 1628 keV gamma-ray transitions, respectively. (b) Same for the lifetime values of the $19/2^-$ state being depopulated by the 1177 keV gamma-ray transition. (c) Same for the lifetime values of the $15/2^-$ state being depopulated by the 690 keV gamma-ray transition. (d) Same for the lifetime values of the $13/2^-$ state being depopulated by the 938 keV gamma-ray transition. (e) Same for the lifetime values of the $11/2^-$ state being depopulated by the 478 keV gamma-ray transition. (f) Same for the lifetime values of the $9/2^-$ state being depopulated by the 812 keV gamma-ray transition.

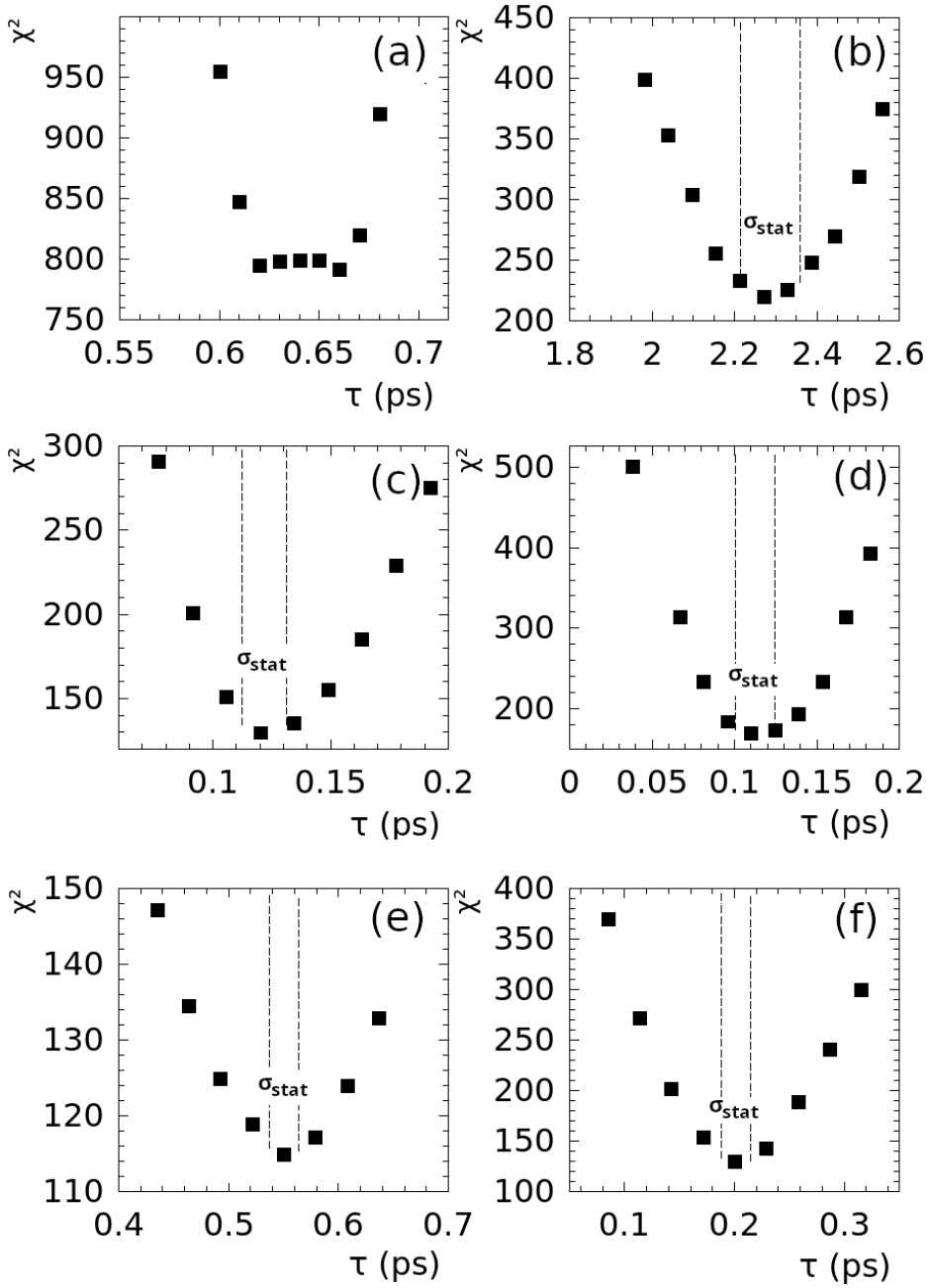

Figure 3.57: χ^2 curves as a function of the lifetime estimated with GEANT4 for the ^{49}Cr. (a) χ^2 curve for the lifetime values of the $23/2^-$ and $15/2^-$ states being depopulated by the 1596 keV and 1628 keV gamma-ray transitions, respectively. (b) Same for the lifetime values of the $19/2^-$ state being depopulated by the 1177 keV gamma-ray transition. (c) Same for the lifetime values of the $15/2^-$ state being depopulated by the 690 keV gamma-ray transition. (d) Same for the lifetime values of the $13/2^-$ state being depopulated by the 938 keV gamma-ray transition. (e) Same for the lifetime values of the $11/2^-$ state being depopulated by the 478 keV gamma-ray transition. (f) Same for the lifetime values of the $9/2^-$ state being depopulated by the 812 keV gamma-ray transition.

state, and the resulting curve of both sets of programs can be observed in Figures 3.54d and 3.55d. The lifetime of the $11/2^-$ excited state was estimated using the line shape of the 478 keV gamma-ray transition, as it does not overlap with other ^{49}Cr gamma-ray transitions, and the resulting curve of both set of programs can be observed in Figures 3.54e and 3.55e. The lifetime of the $9/2^-$ excited state was estimated using the line shape of the 812 keV gamma-ray transition, as it is the strongest transition depopulating the state, and the resulting curve of both sets of programs can be observed in Figures 3.54f and 3.55f. The comparison between the experimental and the best GEANT4 full simulated gamma-ray spectrum is shown in Figure 3.58. The experimental results obtained with both methods were compiled

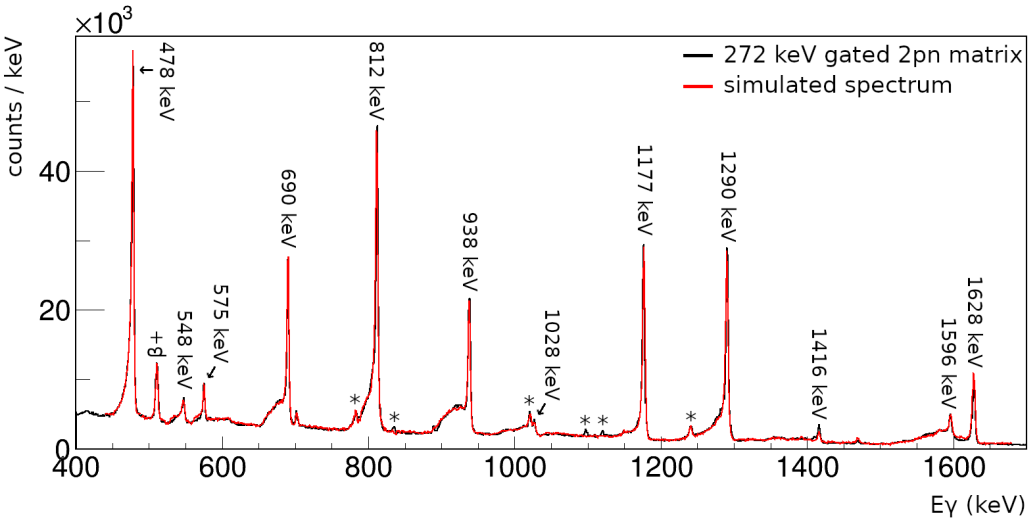

Figure 3.58: GEANT4 simulated gamma-ray spectrum over the background-subtracted one. The indicated energies correspond to the observed transitions which depopulate excited states in the ^{49}Cr. The (*) symbol indicates contaminant peaks.

in Table 3.6.

3.6 Shell Model calculation results

Shell model calculations were performed to describe the structure of the studied nuclei. The ANTOINE code was used with the effective interaction

Table 3.6: Experimental lifetime values were obtained for the ^{49}Cr using LINESHAPE and GEANT4 set of programs.

Transition	E_γ (keV)	γ-BR %	Intensity (a.u.)	$\tau_{exp.}$ (ps) LINESHAPE	$\tau_{exp.}$ (ps) GEANT4	B(E2) (e^2fm^4) LINESHAPE	B(E2) (e^2fm^4) GEANT4
$9/2^- \rightarrow 5/2^-$	1084	5(1)	-	0.23(3)	0.20(3)	126(29)	145(35)
$9/2^- \rightarrow 7/2^-$	812	95(1)	458(2)				
$11/2^- \rightarrow 7/2^-$	1291	55(5)	414(2)	0.61(5)	0.55(5)	203(25)	226(29)
$11/2^- \rightarrow 9/2^-$	478	45(5)	345(2)				
$13/2^- \rightarrow 9/2^-$	1416	10(5)	24(1)	0.15(2)	0.12(2)	72(49)	90(62)
$13/2^- \rightarrow 11/2^-$	938	90(5)	297(2)				
$15/2^- \rightarrow 11/2^-$	1628	28(6)	91(1)	0.11(2)	0.13(2)	183(51)	155(41)
$15/2^- \rightarrow 13/2^-$	690	72(6)	232(2)				
$17/2^- \rightarrow 15/2^-$	1717	28[a]	2.9(2)				
$17/2^- \rightarrow 15/2^-$	1028	72[a]	70				
$19/2^- \rightarrow 15/2^-$	1177	95(5)	283(2)	2.10(17)	2.25(18)	163(16)	152(15)
$19/2^- \rightarrow 17/2^-$	149	5(5)	15(1)				
$23/2^- \rightarrow 19/2^-$	1596	100		0.64(5)	0.64(5)	123(14)	123(14)

[a] Ref. [90].

KB3G-coul, which considers a ^{40}Ca inert core and includes Coulomb effects for the protons.

The structure of the ^{47}Cr for natural parity states was calculated by allowing the excitation of 4 protons and 3 neutrons in the fp space, and the structure of its mirror, ^{47}V, was calculated by allowing the excitation of 3 protons and 4 neutrons in the fp space. Some state not yet experimentally observed were included in the Shell Model calculations. In the ^{47}Cr, the states $J^\pi = 13/2^-$ and $J^\pi = 21/2^-$ were calculated to have an excitation energy of 2.342 and 5.817 MeV, respectively. In the ^{47}V, the $J^\pi = 17/2^-$ state was calculated to have an excitation energy of 4.260 MeV. The structure of the ^{49}Mn for natural parity states was calculated by allowing the excitation of 5 protons and 4 neutrons in the fp space, and the structure of its mirror, ^{49}Cr, was calculated by allowing the excitation of 4 protons and 5 neutrons in the fp space. In the ^{49}Mn, the states $J^\pi = 21/2^-$, $J^\pi = 25/2^-$, and $J^\pi = 29/2^-$, were calculated to have an excitation energy of 6.330, 8.425 and 10.512 MeV, respectively. The comparison between the experimental and the calculated excitation energies for the natural parity states in the mirror pairs shown in Figure 3.59 are in good agreement with the experimental data. All states with exception of the $17/2^-$ and $19/2^-$ in the ^{47}Cr are described in the correct order. The maximum observed discrepancy between the calculated excitation energy and the experimental one is observed for the high spin states of the ^{49}Mn-^{49}Cr and are in the order of 500 keV.

The eighteen experimental B(E2) values weighted by their uncertainties were compared to the Shell Model calculated ones for the nuclei under investigation. A systematic procedure to obtain the value of effective charges for the protons (e_π) and neutrons (e_ν) that better fits the experimental data was applied. Several different combinations of e_π and e_ν in steps of $0.02\,e$ were tested in a grid-search algorithm. The effective charge values that better described simultaneously the B(E2) in all four nuclei found by this procedure were $e_\pi = 1.30\,e$ and $e_\nu = 0.58\,e$. The comparison between experimental and Shell Model calculations for the electric quadrupole reduced transi-

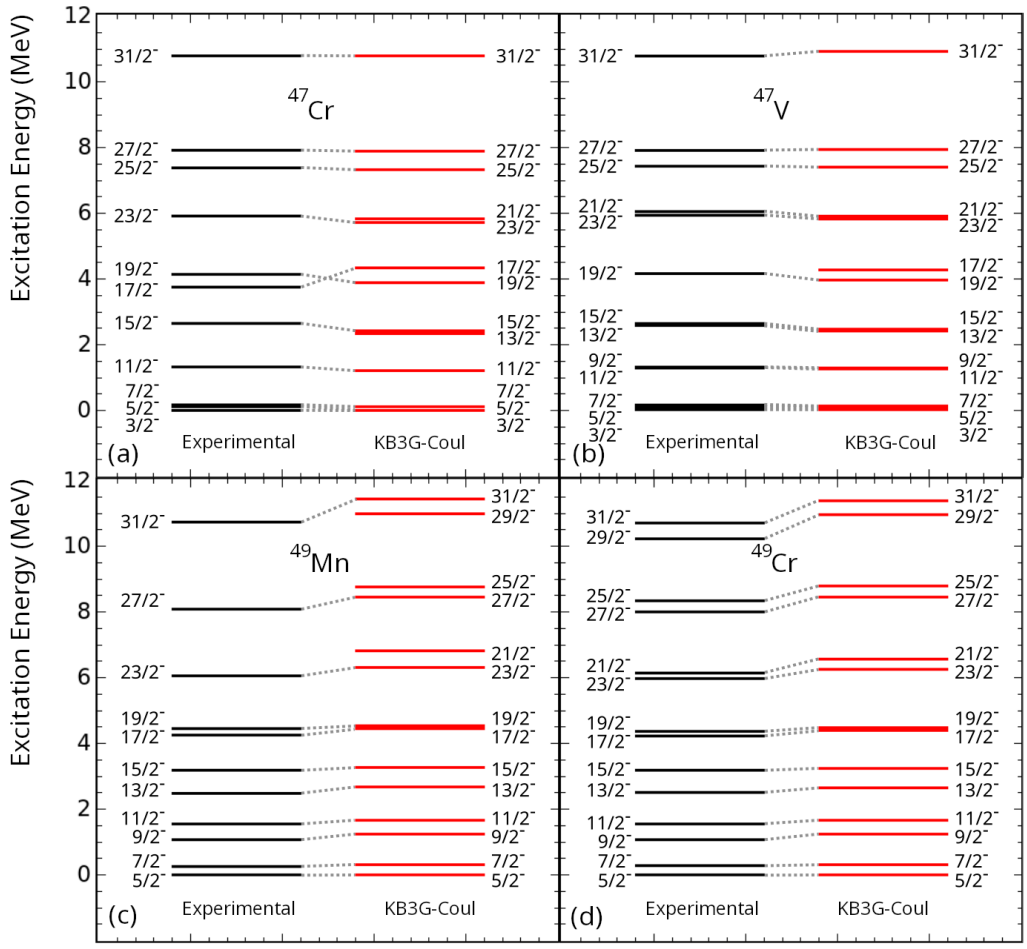

Figure 3.59: Comparison between experimental and Shell Model calculated natural parity yrast states for the mirror pairs A=47 and A=49.

tion probabilities B(E2) using different sets of effective charges are shown in Figure 3.60. The typical adopted values for effective charges $e_\pi = 1.50\,e$ and $e_\nu = 0.50\,e$ are shown alongside the values deduced by du Rietz et al. $e_\pi = 1.15\,e$ and $e_\nu = 0.80\,e$ [41], and Dufour and Zuker. $e_\pi = 1.31\,e$ and $e_\nu = 0.46\,e$ [91]. Using the obtained values for the effective charges it is

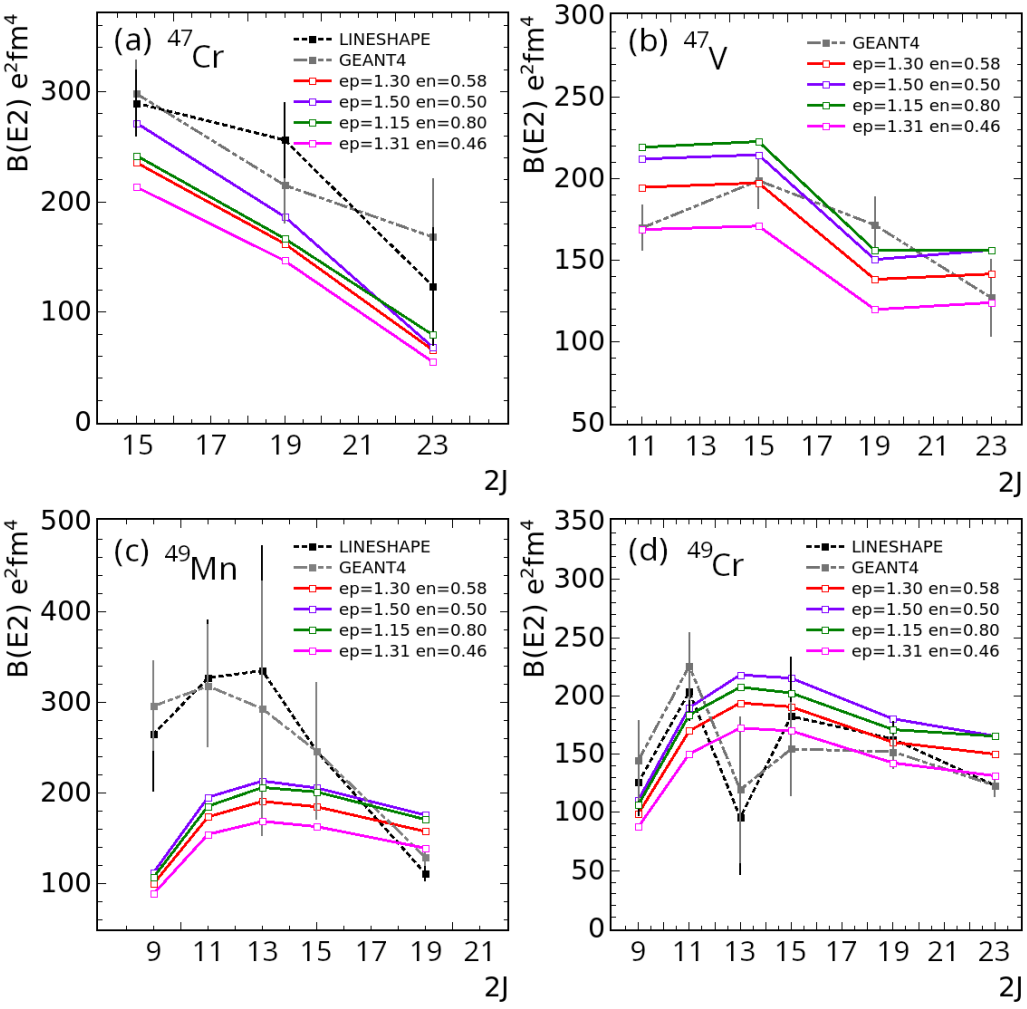

Figure 3.60: The Experimental and Shell Model calculated reduced transition probabilities B(E2) for excited states in (a) ^{47}Cr, (b) ^{47}V, (c) ^{49}Mn, and (d) ^{49}Cr.

possible to obtain the polarization charges according to the equation 2.23. The obtained values were $e^{(0)}_{pol} = 0.44$ and $e^{(1)}_{pol} = 0.14$. The value of $e^{(0)}_{pol}$ is

similar to the one obtained by du Rietz in agreement with Bohr-Mottelson formula 2.24.

The Shell Model B(E2) values calculated for the ^{47}Cr using all sets of effective charges decrease sharply with angular momentum, which is also observed in the experimental data. However, the B(E2) values experimental data are consistently higher than the Shell Model calculated ones. The Shell Model B(E2) values calculated for the ^{47}V are mostly compatible with the experimentally obtained values and show a smooth decrease in B(E2) as a function of the angular momentum. In the case of the Shell Model calculated B(E2) values for ^{49}Mn, an increase is predicted from $J^{\pi} = 9/2^{-}$ to the $J^{\pi} = 11/2^{-}$ by all sets of effective charges. Despite this same tendency being observed in the experimental values, the Shell Model values are about 3 times smaller than the experimental ones. The Shell Model predicts then a smooth increase towards $J^{\pi} = 13/2^{-}$ and from there a smooth decrease until $J^{\pi} = 19/2^{-}$. The experimental values on the other hand, other than being larger than the Shell Model calculated ones, present a strong decrease in the B(E2) values. The Shell Model calculated values of B(E2) for the ^{49}Cr show a good general agreement with the experimental data for all sets of effective charges. The only remarkable exception is the case of $J^{\pi} = 13/2^{-}$, which is a reduction of the B(E2) value caused by what is known as band crossing, interpreted by Brandolini et al [92] for the ^{46}V and ^{48}V, and observed for this same state in [90].

The experimental B(E2) values obtained for all four nuclei indicate a collective behavior of the excited states analyzed, given the high value for the reduced transition probability. In all cases, the value of the B(E2) decreases with the increase in the angular momentum. Such behavior is caused by the alignment of the valence nucleons to construct the state's angular momentum. The alignment of valence nucleons approaching band termination ultimately decreases the state's collective character. The Shell Model calculations for the B(E2) evolution of the ^{47}Cr present the same trend as the experimental ones. However, the Shell Model calculated values are predicted to be smaller

than the experimentally obtained ones. The calculation predictions for the ^{47}V show a good agreement with the experimental values, mainly for the effective charges obtained in the present work. The Shell Model calculations for the B(E2) evolution of the ^{49}Mn show instead a smoother increase and a decrease of the B(E2) values as a function of the angular momentum in comparison with the experimental results. The Shell Model calculation predicts smaller values than the experimentally observed ones. Overall, the calculation results for the ^{49}Cr show a good agreement with the experimental values, considering the typically adopted effective charges and the ones obtained in the present work. However, when comparing the B(E2) values between the mirrors ^{49}Mn - ^{49}Cr, it is possible to observe that the Shell Model predicts nearly identical values for the pair, which is not verified experimentally. From the experimental point of view the larger B(E2) values found for the ^{49}Mn are robust, as even considering that the lifetime values can be affected by systematic errors due to side feeding, this would have a tendency to overestimate the lifetime. This discrepancy between Shell Model prediction and experimental data for the ^{49}Mn is present for any set of effective charges. Such a result is surprising, considering that, in this mass region, the Shell Model can reproduce these differences reasonably well for the mirror nuclei that have been measured so far. For instance, in the mirror pair A = 43, the B(E2) value of the transition $19/2^- \rightarrow 15/2^-$ in the ^{43}Ti is twice as big as the value in its mirror counterpart and Shell Model can still reproduce this difference [93, 94, 95]. Another example of mirror pair in the mass region that present very different B(E2) values is the transition $3/2^- \rightarrow 7/2^-$ in the ^{45}V that is three times larger than its analogue transition in the ^{45}Ti [96, 97]. If Shell Model fails to reproduce this experimentally observed difference also for the mass A = 45 mirror pair, that might indicate some effect that is not being accounted when the proton-rich member of the isospin doublet has an odd number of protons. In such cases the mirror displacement energies is particularly large. A further experiment to measure lifetime in the mirror pair ^{53}Co - ^{53}Fe would also help to extend the understanding of this effect.

The observation of this discrepancy opens a discussion to different insights and, if confirmed, would bring new understanding to the nuclear structure in this mass region.

Chapter 4

Lifetime of the 6^+ excited state in the ^{54}Ni

Major improvements over the past decades in the production and separation of radioactive beams have enabled gamma-ray spectroscopy of nuclei very far from the stability. The experiment reported here was performed at Radioactive Ion Beam Factory (RIBF) facilities at RIKEN Nishina Center, Japan. The radioactive beams are produced in RIBF by fragmentation of the primary beam in a target that can be understood in terms of an abrasion-ablation process. The abrasion is the process in which the primary beam and target nuclei collide, shearing away pieces from the projectile and target [98]. The abraded nuclei of the beam deexcite by emitting light particles during the ablation phase, becoming the fragments that are separated to be used as radioactive beams [99].

An experiment to populate excited states in the ^{54}Ni was performed using a 345 MeV/u ^{78}Kr primary beam to produce the exotic secondary beam of ^{55}Ni. The products of the fragmentation of the 345 MeV/u ^{78}Kr beam were selected and tagged by the BigRIPS fragment separator. The 6^+ excited state of the ^{54}Ni was populated in one neutron-knockout reaction after the collision of the secondary ^{55}Ni beam in the 6 mm thick ^{9}Be target. The gamma rays were detected with the DALI2+ spectrometer array, and the ZeroDegree fragment separator identified the ^{54}Ni reaction product.

In the following sections, a description of the experimental setup used in this experiment, the lifetime measurement technique, data selection, data

analysis procedure, and the experimental results are presented.

4.1 Experimental setup

4.1.1 BigRIPS and ZeroDegree

One of the methods to produce RIB is the in-flight separation technique, in which a primary nuclear reaction is performed to produce a set of radioactive nuclei that are sorted in-flight to be used in the experiment [100]. The primary beam is provided by the accelerators installed in the Radioactive Ion Beam Factory (RIBF) facilities at Riken Nishina Centers, Japan. BigRIPS is

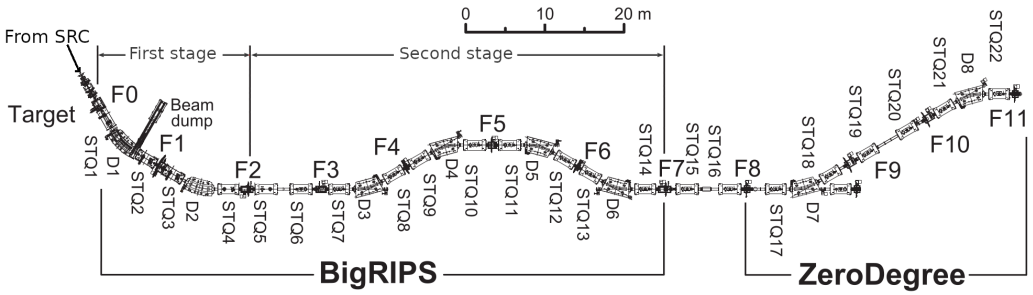

Figure 4.1: Scale representation of the BigRips fragment separator. Adapted from [19].

a two stages high-acceptance projectile fragment separator. The first stage is responsible for producing and selecting the radioactive secondary beam, and the second stage is used to identify the secondary beam [19]. As shown in Figure 4.1, the first stage is composed of two room-temperature dipoles with a bending angle of 30°, D1 and D2, and four superconducting quadrupole triplets, STQ1 - STQ4. In order to produce the radioactive beams, a thick target is positioned in the F0 focal plane, and it is bombarded by a high-energy, high-intensity stable beam. The nuclei of interest are selected using the momentum-loss achromatic technique ($B\rho$-ΔE-$B\rho$) [100, 101]. The dipoles bend the isotopes trajectory based on their different magnetic rigidity, providing a first degree of selectivity. However, this is sensitive only to the mass-charge ratio, as can be observed in equation 4.1. Where B is the magni-

tude of a uniform magnetic field, ρ is the trajectory radius, $\gamma = 1/\sqrt{1-\beta^2}$, A is the mass number, Z is the atomic number, u is the atomic mass unit, e is the elementary charge, $\beta = v/c$ and c is the speed of light.

$$B\rho = \gamma \frac{Au}{Ze} \beta c \tag{4.1}$$

The isotopes emerging from the production target pass through a wedge degrader located in F1 focal plane, allowing the selection of the isotopes based on their energy loss according to the Bethe-Bloch equation 4.2, where I is the average ionization potential of the material and N_m and Z_m are the density and the atomic number of the target [102, 58]. The shape of the wedge degrader ensures the achromaticity of the first stage by focusing the beam to a single point in the focal plane F2 [101, 102]. The combination of both Bρ and energy loss can discriminate the fragments since different Z will be subject to different energy losses.

$$\frac{dE}{dx} = -\frac{4\pi e^2 Z^2}{m_e v^2} N_m Z m \left[ln\left(\frac{2m_e v^2}{I}\right) - ln\left(1 - \frac{v^2}{c^2}\right) - \frac{v^2}{c^2} \right] \tag{4.2}$$

The second stage of BigRIPS is formed by the dipoles, D3-D6, and eight superconducting quadruple triplets, STQ7-STQ14. This stage is responsible for identifying and tagging the desired radioactive beam and relies on the TOF-Bρ-ΔE method. The time of flight (ToF) is calculated using the time difference between two plastic scintillators positioned in the foci F3 and F7. The determination of Bρ, according to equation 4.1, provides the mass-charge ratio needed to identify the fragments. This is achieved using the trajectory reconstruction allowed by the position-sensitive Parallel Plate Avalanche Counters (PPACS) positioned in the foci F3, F5, and F7 [102]. The PPACs are arranged in couples, further increasing their efficiency and serving as a backup in case of failure of one. The energy loss measurement is performed by a Tilted Electrode Gas Ionization Chamber (TEGIC) positioned in the F7 focal plane. This method allows selecting the desired radioactive beam to be used in the reaction, tagging in the desired isotope

before the reaction with the reaction target. After leaving the F7 ionization chamber, the radioactive beam is transported to the secondary target, where the reaction is induced.

The reaction products energies from the secondary target are identified on an event-by-event basis. For this reason, a two-bend achromatic system called ZeroDegree spectrometer is placed just after the secondary target in the beam line. It is composed of two dipoles and six STQs, indicated as D7 and D8 and STQ17–STQ22 in Figure 4.1 [22]. Similar to BigRIPS, the isotope identification is performed using TOF-Bρ-ΔE. The TOF is measured by the time difference between plastic scintillators positioned in the foci F9 and F11. The mass-charge ratio is obtained by measuring Bρ using PPACs positioned at the foci F8, F9, and F11. The energy loss is measured in with a TEGIC positioned in the focal plane F11. This double tagging procedure, i.e., BigRIPS to select the entering radioactive beam and ZeroDegree to select the reaction product, allows a selection of the reaction clean from contamination.

4.1.2 DALI2+

The Detector Array for Low-Intensity radiation was designed to detect low-intensity radiation emitted from heavy-ion-induced reactions using fast-moving radioactive beams. The array is composed of 226 detectors placed around the target to cover a large solid angle [20]. Each detector is composed of a NaI(Tl) scintillator encapsulated in a 1mm-thick aluminum housing coupled to Photo-Multiplier Tube (PMT). In Table 3.1 three different types of NaI(Tl) scintillators are shown. The wide angular coverage of DALI2+ al-

Table 4.1: Physical characteristics of the DALI2+ detectors. The PMT are manufactured by Hamamatsu. Taken from [101].

Manufacturer	dimensions (mm^3)	PMT model	PMT diameter (cm)
Saint-Gobain	$45 \times 80 \times 160$	R580	38
Scionix	$40 \times 80 \times 160$	R580	38
Bicron	$60 \times 60 \times 120$	R1306	50

lows it to be sensitive to the angular distribution of gamma rays, perform Doppler shift corrections for gamma rays emitted from nuclei with velocities of up to $\beta = 0.6$, and reduce the uncertainty in extracting the total gamma yield [20]. In Figure 4.2 a 3D rendering of the half-sector of the DALI2+ array is shown. The array's efficiency can be further improved by using an

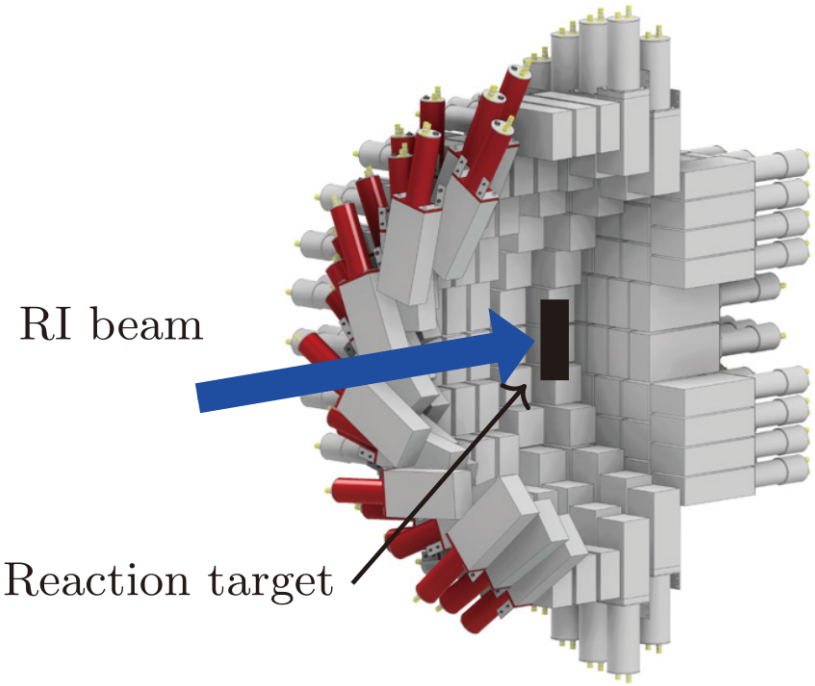

Figure 4.2: Tridimensional representation of half of DALI2+. Taken from [21].

add-back technique. This technique consists of using a detector's signals in coincidence with its neighboring detectors to create a cluster. The detector with the highest energy deposition is assumed to be the one where the first interaction happened, and the sum of energies of the cluster is recorded as the incident energy. The chance of the add-back procedure of misassigning the gamma-ray interaction point is below 20% [20]. The main parameters for the DALI2+ are summarized in Table 4.2.

Table 4.2: Nominal intrinsic energy resolution of the DALI2+ array. Without add-back / with 15 cm radius add-back. Taken from [21]

	$\beta = 0$	$\beta = 0.6$	
E_γ (keV)	eff. (%)	eff (%)	FWHM (keV)
500	37/43	40/48	38/43
1000	22/29	24/34	76/85
2000	13/19	15/23	139/155

4.2 Data selection

The techniques employed for the selection and identification of the radioactive beams rely on the detectors of BigRIPS and ZeroDegree separators. They allow tagging directly on the events corresponding to the desired isotope. The identification was performed by measuring its different mass over charge ratios and energy loss in a medium. Accordingly, with the equation 4.1, the mass over charge ratio can be determined by knowing the ion's velocity and their magnetic rigidity $B\rho$. Experimentally, the velocity of the ions is obtained by ToF measurements performed with plastic scintillators, and the $B\rho$ is determined using position reconstruction provided by the PPACs. In the following, the steps taken to ensure the proper measurement of Time-of-Flight, $B\rho$, and energy loss are described.

4.2.1 Time-of-Flight measurement

The plastic scintillators have two PMT, one on each side, generating a time signal, t_1 and t_2, and a signal proportional to the deposited charge, q_1 and q_2. The position where the ions hit the plastic can be extracted in accordance with the equations 4.3 and 4.4 [103], where V and λ are the speed of light and the attenuation length of light in the scintillation material, respectively.

$$x = -\frac{V}{2}\,(t_2 - t_1) \tag{4.3}$$

$$x = -\frac{\lambda}{2} ln(\frac{q_1}{q_2}) \tag{4.4}$$

As the position of the incident ion into the PPAC is unique due to the achromatic character of the separator[101], consistent events should fulfill the requirement indicated in the equation 4.5. The events detected by the plastic scintillators located at the foci F3, F7, F9, and F11 were verified for consistency. Given the relation 4.5 it is expected a linear diagonal shape in a plot of the logarithm of the charge ratios vs the time difference. This can be observed in Figure 4.3.

$$V\,(\,t_2 - t_1) = \lambda\, ln(\frac{q_1}{q_2}) \tag{4.5}$$

The double PMT approach also allows the obtaining of a time signal independent from the incident position of the ions by taking the average of t_1 and t_2, as shown in equation 4.6, where F is the number of the plastic detector.

$$T(F) = \frac{1}{2}\,(t_1(F) + t_2(F)) \tag{4.6}$$

Then, the ToF between two foci can be simply obtained by evaluating the difference of the time signals, as described in equation 4.7. Where TOF_{ab} is the time-of-flight from the Fa position to the Fb position.

$$\begin{aligned} TOF_{37} &= T(F7) - T(F3) + T_{offset}(37) \\ TOF_{911} &= T(F9) - T(F11) + T_{offset}(911) \end{aligned} \tag{4.7}$$

4.2.2 Magnetic rigidity measurement

The Parallel Plate Avalanche Counters (PPAC) are used to measure the trajectory of the ions and obtain a $B\rho$ measurement. Each PPAC is composed of three parallel electrodes separated by 4.3 mm, with the anode in the middle of two cathodes. The active area of 240 $\times$ 150 mm^2 of the detector is filled with C_3F_8 gas at 10 Torr. The detector anode has a 850 V bias applied to it. The ionization of the gas caused by the interacting ions generates an

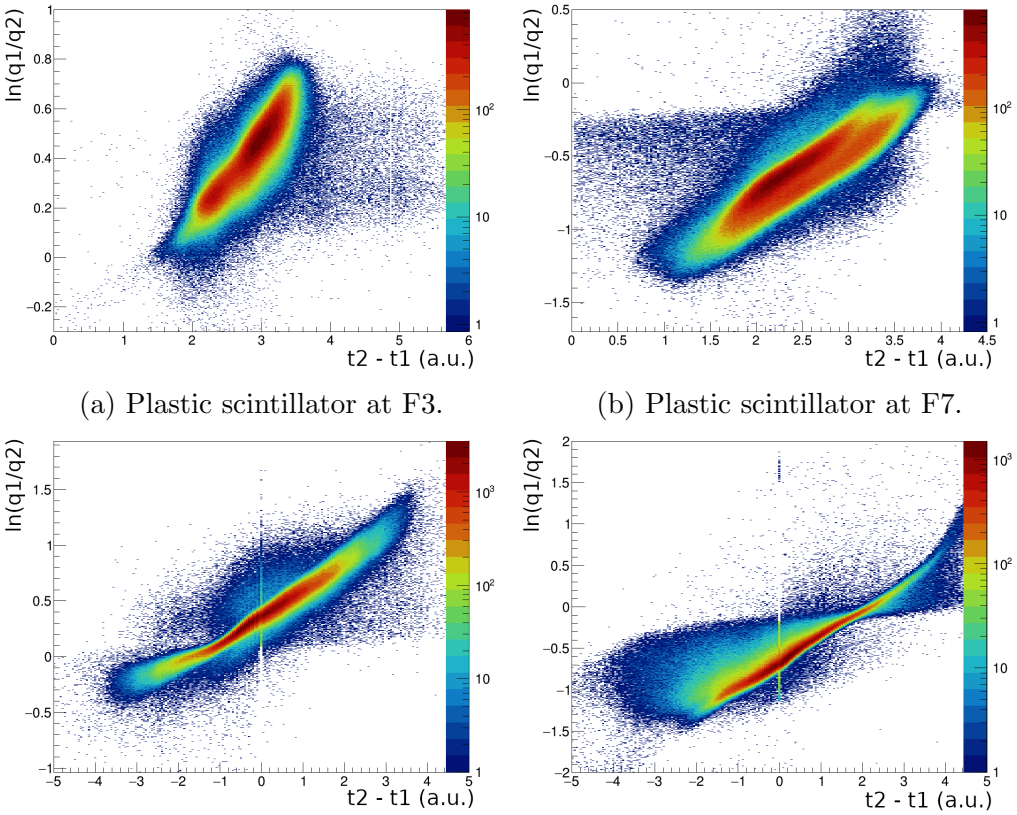

(a) Plastic scintillator at F3.

(b) Plastic scintillator at F7.

(c) Plastic scintillator at F9.

(d) Plastic scintillator at F11.

Figure 4.3: Example of two-dimensional histograms showing the correlation between the charges deposited in the plastic scintillators by the ions and the time difference of the signals detected by the PMT.

avalanche of electrons. Each PPAC outputs 5 signals, 2 signals from the X cathode, T_{X1} and T_{X2}, 2 signals from the Y cathode, T_{Y1} and T_{X2}, and a signal from the anode, T_A, that are processed and sent to a Time to Digital Converter (TDC). This time signal allows the precise determination of the interaction points of the ions in the PPAC, according to the equation 4.8, and provides position sensitivity. Where k_x and k_y (mm/ns) is the position coefficients, and the offsets are parameters to account for delay lines and geometrical misalignment[101].

$$\begin{aligned} x &= k_x \frac{T_{X1} - T_{X2}}{2} + X_{offset} \\ y &= k_x \frac{T_{Y1} - T_{Y2}}{2} + Y_{offset} \end{aligned} \tag{4.8}$$

The quantities T_{sum} presented in the equation 4.9, are constant for valid events, allowing a consistency check for good events to be performed.

$$\begin{aligned} T_{sumX} &= T_{X1} + T_{X2} - 2T_A \\ T_{sumY} &= T_{Y1} + T_{Y2} - 2T_A \end{aligned} \tag{4.9}$$

In Figure 4.4, the quantities T_{sum} are plotted for the PPACs located at the foci F3 and F4, it is possible to observe that the good events are concentrated around a constant value. After ensuring the consistency of the PPACs it is possible to obtain the mass-over-charge (A/Q) ratio following the procedure described in [101].

4.2.3 Energy loss measurement

According to the Bethe-Bloch formula, 4.2, the energy loss of the ions interacting with the material is proportional to the square of the atomic number Z. In order to measure the energy loss of the isotopes produced in BigRIPS and ZeroDegree, Tilted Electrode Gas Ionization Chambers (TEGIC) were positioned at the foci F7 and another one at F11. These ionization chambers consist of 12 anode plates, biased with $500\,V$, and 13 cathode plates, tilted 30° to reduce the electron-ion recombination probability. The electrode signals

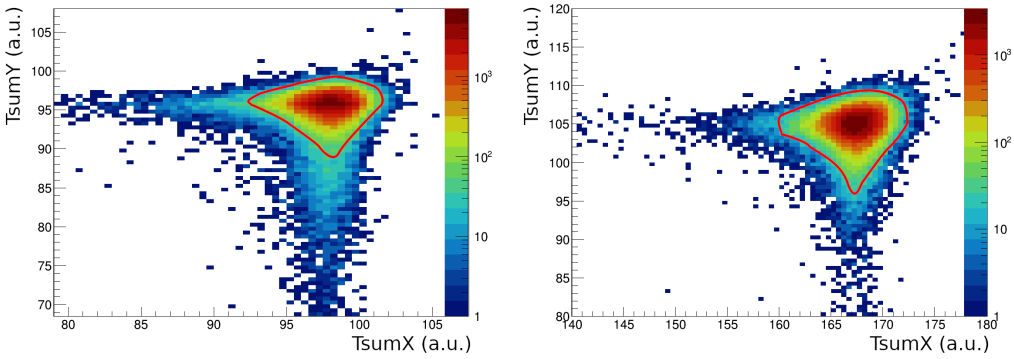

(a) PPAC3-1A located at F3. (b) PPAC7-1A located at F7.

Figure 4.4: Example of two-dimensional histograms of T_{sum} quantities for the first PPAC of the doublet A at focal point F3 (PPAC3-1A), and F7 (PPAC7-1A). The events lying inside the red curve are considered the good ones.

were taken combining two electrodes and, therefore, each TEGIC outputs 6 signals. The signals are processed using shaping amplifiers and digitized with a charge-to-digital converter (QDC). The geometric average of the signals is stored and used for the energy loss measurement. An example of a Z measurement performed with the TEGIC at the foci F7 is shown in Figure 4.5.

4.2.4 The Particle Identification - PID

After ensuring the consistency for all the detectors that constitute BigRIPS and ZeroDegree, it is possible to combine the optimized parameters to achieve maximum resolution in particle identification selectivity in both incoming and outgoing fragments. It is possible to obtain the PID using different groups of parameters in BigRIPS and ZeroDegree for the time of flight. The time of flight between F3 and F7 was found to be the one with better time resolution and higher statistics for the BigRIPS, while for the ZeroDegree, it was the time of flight from F9 to F11. These times of flight were combined with the energy loss measurement of the TEGIC at F7 and F11 for incoming and outgoing PIDs, respectively. Figure 4.6 shows calibrated

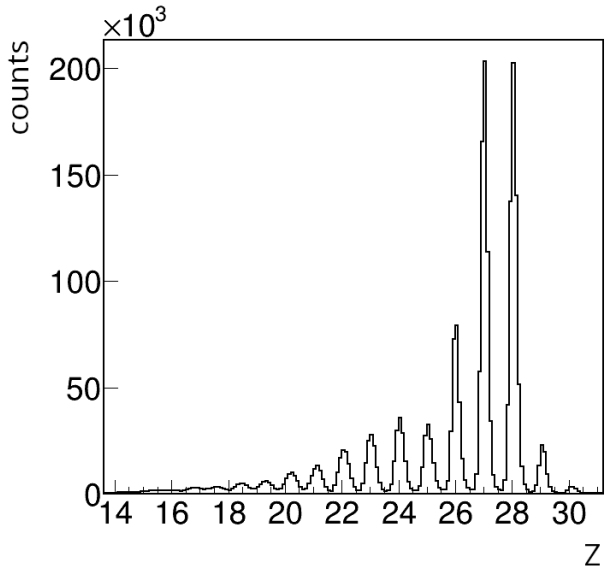

Figure 4.5: Calibrated measurement of the atomic number Z performed with the TEGIC located on the foci F7.

PID histograms before and after the reaction. All the details of this analysis are reported in [102]. It is possible to observe the background in the PID

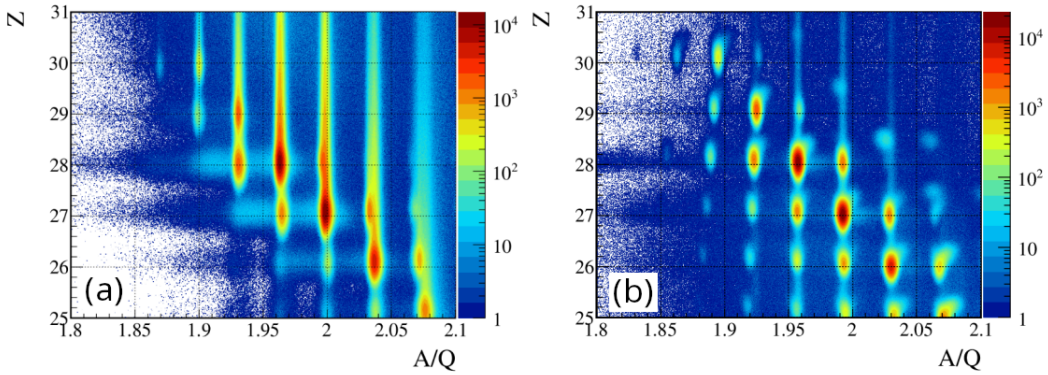

Figure 4.6: Calibrated PID. (a) Secondary beams on BigRIPS. (b) Outgoing fragments after the secondary reaction. Taken from [102].

histograms. The blue blob that spreads all over the PID spectrum can arise from multiple sources, signal pile-up, multi-hit, δ-rays, or not fully stripped ions. The signal pile-up was removed by requiring a correlation between the

signal in the TEGICs and plastic scintillators. By making the requirement that all PPACs fired, the number of inconsistent events due to multi-hit and δ-rays also decreased sharply. After such requirements, the resulting statistics are lower, but any contamination is removed. Figure 4.7 shows calibrated PID histograms before and after the reaction with the above-mentioned conditions. It is possible to observe a huge reduction in the background in comparison with Figure 4.6. The separation between different isotopes is extremely clean.

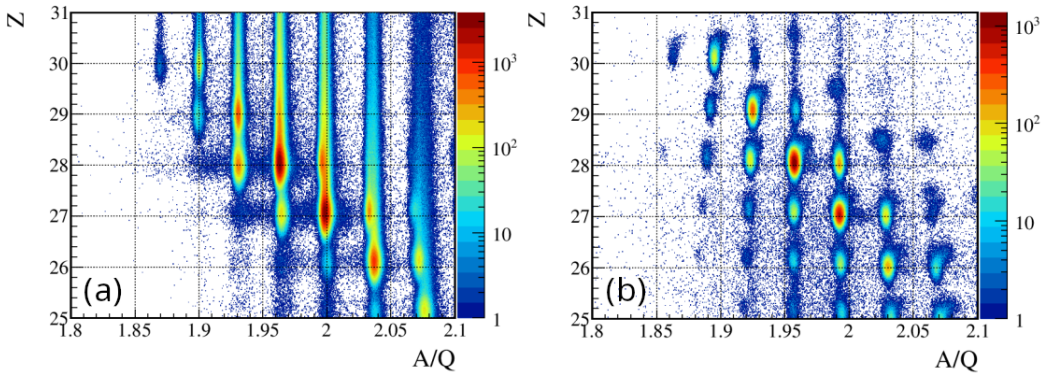

Figure 4.7: Calibrated PID bi-parametric histograms requiring all PPACS fired and correlation between plastic scintillators and TEGIC signals. (a) Secondary beams on BigRIPS. (b) Outgoing fragments after the secondary reaction. Taken from [102].

The gates performed on the PID spectra selected events of the ^{55}Ni in the BigRIPS in coincidence with the events of the ^{54}Ni fragment in the ZeroDegree. These conditions on the incoming and outgoing cleaned the gamma-ray spectrum from any detectable contamination. The detailed procedure for the time and energy calibration of the 223 working DALI2+ detectors using sources and background radiation is also presented in [102].

4.3 In-flight Line Shape Lifetime Measurements

For excited states with lifetimes longer than a few picoseconds, the usual DSAM technique does not apply, mainly because the recoil nuclei's excited

state will live long enough to decay at rest. However, if the recoil nuclei have enough velocity and the excited state lives for longer than some ps, the Doppler effect can still be used to extract the lifetime.

The detected gamma-ray energy arising from fast-moving ($\beta > 0.1$) recoil nuclei are subject to the Doppler shift given by the equation 3.2. The velocity of the recoil nuclei strongly affects the gamma-ray detected energy; consequently, the Doppler-shift correction procedure is mandatory to observe the correct energies in the gamma-ray spectrum. In Figure 4.8 the Doppler-shifted spectrum is shown overlaid with the Doppler-corrected one for the ^{54}Ni. The β is estimated considering fast gamma-ray transitions ($\tau < 1$ ps)

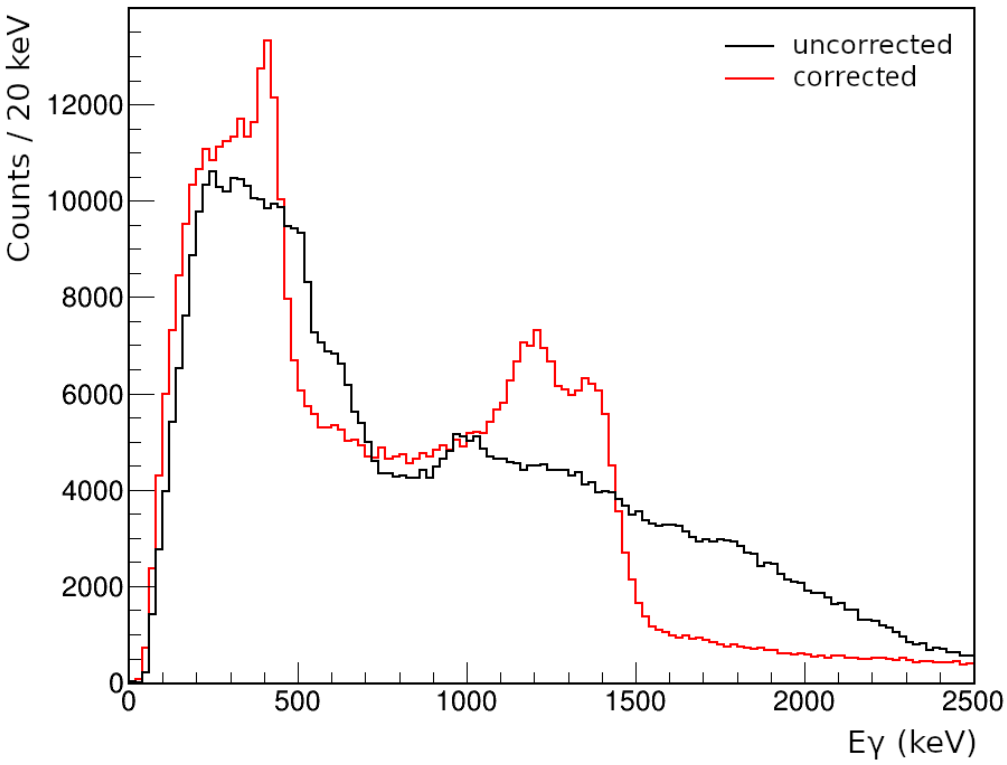

Figure 4.8: Experimental gamma-ray energy spectrum acquired by DALI2+ showing the effect of the Doppler-shift correction in the gamma-ray energy peaks 451 keV, 1227 keV, and 1392 keV. The adopted β to perform this correction was $\beta = 0.4984$.

occurring in the center of the target [101]. However, in case an excited state

lives for enough time the produced nucleus can move away from the target, distorting the gamma-ray energy peaks due to improper Doppler correction for those events. For instance, if a recoil has a $\beta = 0.5$, its flight distance over 100 ps will correspond to the macroscopic length of about 1.7 cm [104]. This technique has been applied to measure the lifetime of the 6^+ excited state of the ^{54}Ni. Geant4 simulations have been utilized to map the response function of the array for different lifetimes.

4.3.1 DALI2+ simulation code

A GEANT4 code for the gamma-ray spectrometer DALI2+ was made available by the SUNFLOWER collaboration [105]. Similar to the `Agata` code, it possesses an event generator, event builder, and reconstructor. The event generator handles the physical processes between the beam and target, the recoil nuclei, and gamma-ray emission. The event builder handles the response function of the array to the previously simulated gamma-rays, while the reconstructor allows Doppler correction in the simulated events and creates histograms that can reproduce experimental data with good accuracy. This code can simulate not only single gamma-ray emission but also multiple gamma-rays following the lifetime and the level scheme provided. In Figure 4.9 a Doppler corrected $E_\gamma = 1392$ keV simulated gamma-ray transition, depopulating the 2^+ state of ^{54}Ni, considering two different lifetimes, is shown. For states with lifetimes longer than ≈ 5 ps, it is possible to observe a distortion of the gamma-ray energy peak towards the low-energy and a small change in the spectrum as a whole. Consequently, the simulations involving gamma-rays emitted in cascade require weighting the contribution of each transition sequence. In the case of the ^{54}Ni, as the highest populated state is the 3070.7 keV ($J^\pi = 6^+$), this excited state and the ones bellow it needs to be simulated, i.e., the cascades $6^+ \rightarrow 4^+ \rightarrow 2^+ \rightarrow 0^+_{gs}$, $4^+ \rightarrow 2^+ \rightarrow 0^{+0}_{gs}$, and $2^+ \rightarrow 0^+_{gs}$. In figure 4.10 the individual decay cascades simulated with lifetime $\tau < 1$ ps for the ^{54}Ni are shown. The procedure to find the lifetime consists in fitting the contributions of the simulated cascades and a double

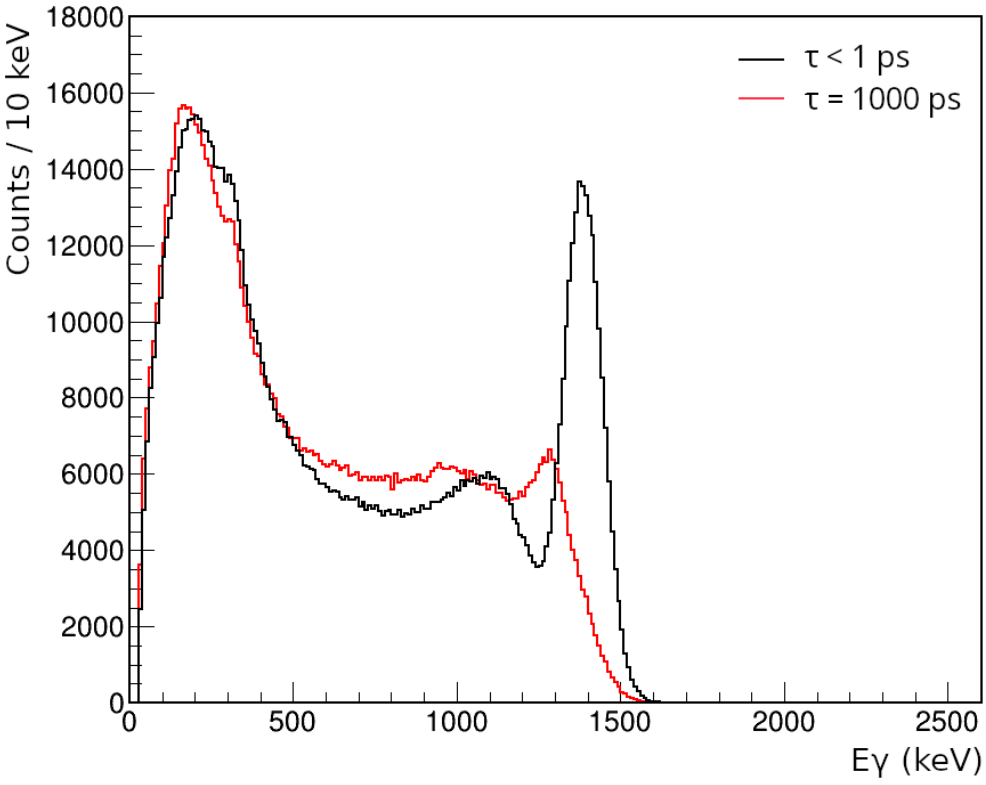

Figure 4.9: Simulated gamma-ray spectrum due to the emission of the E_γ = 1392 keV gamma-ray which depopulates the 2^+ state of ^{54}Ni.

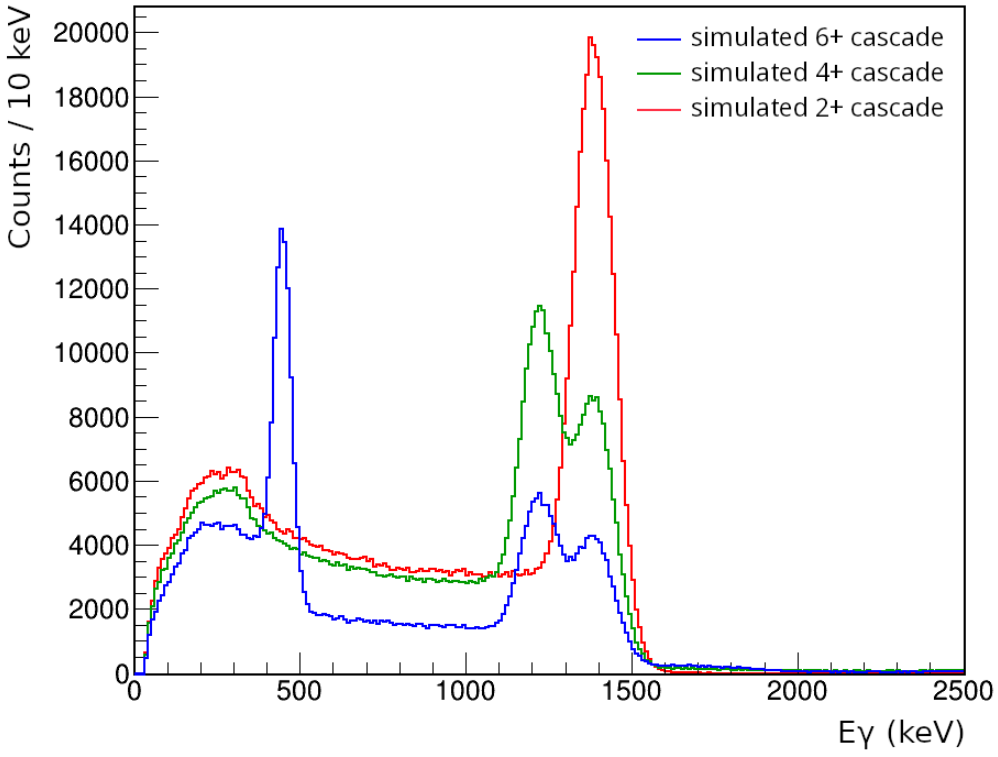

Figure 4.10: Simulated gamma-ray spectrum of the individual decay cascades of the ^{54}Ni. Here all cascades are presented with the same amount of events.

exponential background to the experimental data. The fit procedure has four free parameters for the background and two free parameters for each simulated cascade simulated. One parameter allows a small shift in energy to compensate for miscalibration or wrong Doppler correction, and the other is a scale factor that determines the weight of the cascade in the spectrum. The lifetime is determined by the minimization of the χ^2 procedure. Figure 4.11 shows the result of the described simulation and fitting procedure for a lifetime of 967 ps in the 6^+ state of the ^{54}Ni.

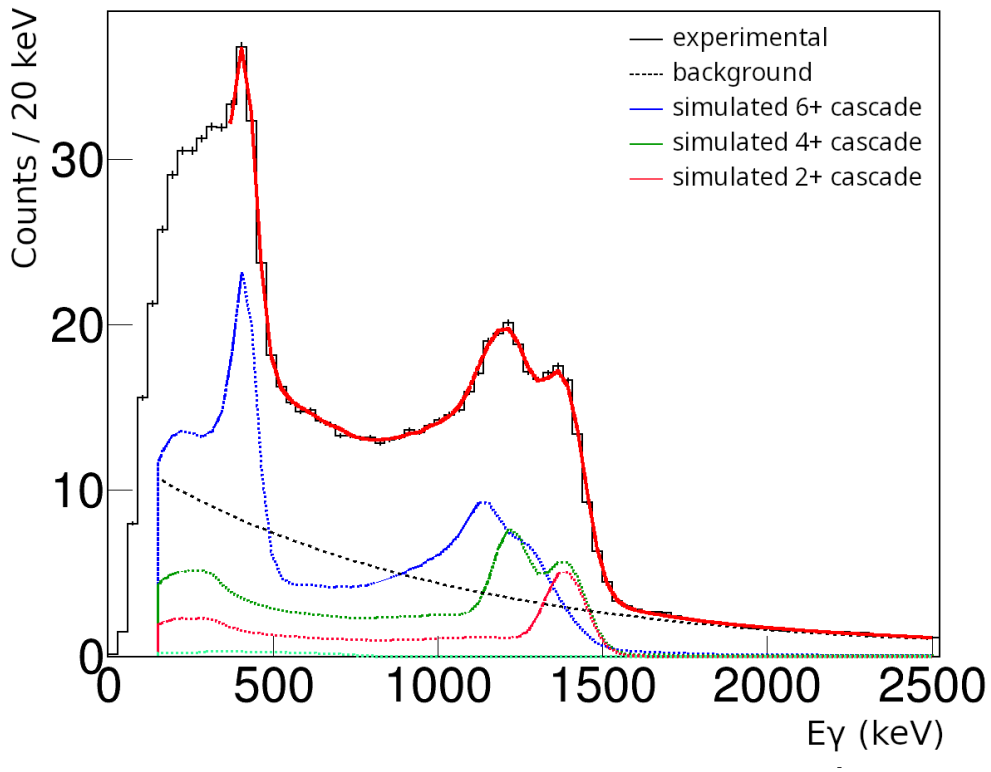

Figure 4.11: Simulated gamma-ray spectrum displaying the individual contributions of the multiple gamma-ray cascades summed to a double exponential background.

4.4 Experimental results

The one neutron knockout of the ^{55}Ni populated low spin states in the ^{54}Ni. The ^{55}Ni fragments were tagged in the BigRIPS, while the reaction product ^{54}Ni was tagged in the ZeroDegree separator. The gamma rays, detected by the DALI2+ array, in coincidence with the incoming ^{55}Ni and outgoing ^{54}Ni were sorted into energy spectra and coincidence matrices. In this work, only add-back gamma rays were used. The Doppler correction was applied to the gamma-ray energies using a β calculated. In Figure 4.12 the adopted β value is shown in a two-dimensional plot of the gamma-ray energies and β. In this plot, it is possible to observe that the calculated β corresponds to the best peak resolution. The gamma-ray coincidence matrix

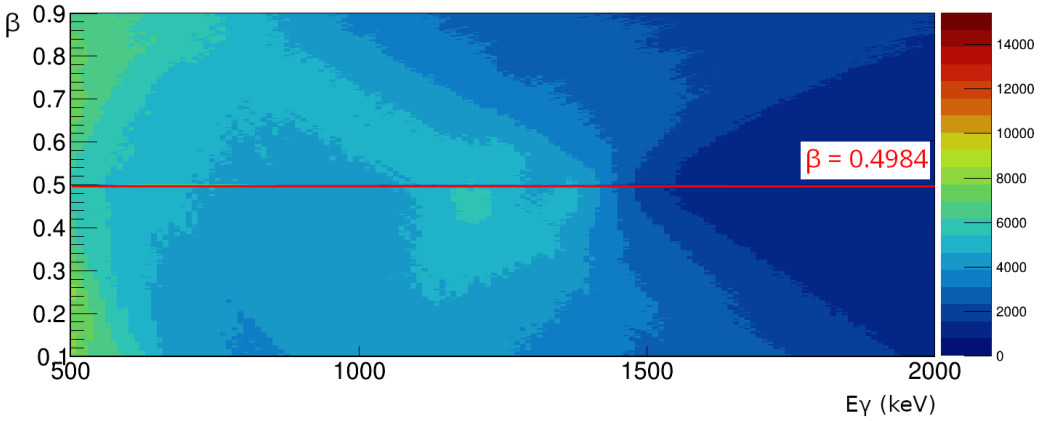

Figure 4.12: Two-dimensional histogram showing the effect of the various β values in the energy shapes. It is possible to observe that the resolution of the gamma-ray peaks is optimal for β values around 0.5.

and the gamma-ray spectrum after Doppler correction are presented in Figure 4.13. The level scheme displaying all known gamma-ray transitions of the ^{54}Ni is shown in Figure 4.14. The gamma-ray coincidence matrix was used to identify the highest populated state in the knockout reaction by performing gates in different known gamma-ray energies of the ^{54}Ni. Figure 4.15 shows that states above the 6^+ were not populated as no gamma-rays depopulating the 8^+ and 10^+ were observed. The conditions imposed by simultaneous coincidence on the incoming and outgoing channel of the one neutron knockout

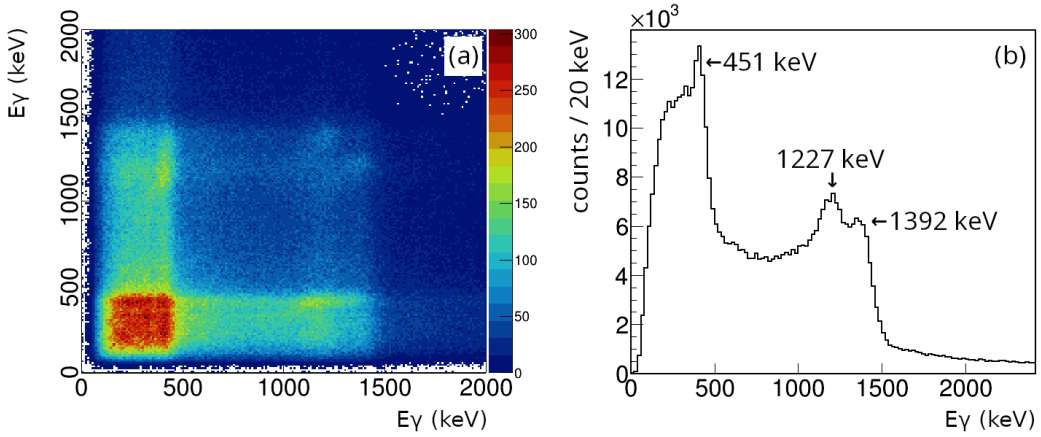

Figure 4.13: (a) Gamma-ray coincidence matrix created with Doppler corrected gamma-rays tagged in the incoming ^{55}Ni and outgoing ^{54}Ni. (b) Gamma-ray spectrum created with Doppler corrected gamma-rays tagged in the incoming ^{55}Ni and outgoing ^{54}Ni.

reaction generated a gamma-ray spectrum without observable contamination, allowing the lifetime determination to be performed without gating on gamma-rays.

The lifetime of the 6^+ state was determined using GEANT4 simulations to reproduce the observed shape. The direct population of the states was simulated separately and then weighted and added together to compose the final simulated spectrum. Other than the known gamma-ray transitions, a simulation to account for the extra 511 keV intensity, and a double exponential background were considered to reproduce the experimental spectrum. The 6^+ cascade includes the 451, 1227, and 1392 keV gamma-rays. The 4^+ cascade includes the 1227 and 1392 keV gamma-rays. The 2^+ cascade includes the 1392 keV gamma-ray. A total of two million events per cascade were simulated. The fit resulting from the grid search algorithm is presented in Figure 4.16. The χ^2 as a function of the lifetime is shown in figure 4.17. In order to validate the adopted procedure, the data was split in rings depending on their angular position and the fitted value was plotted over experimental data. In figures 4.18 and 4.19 the fitted values split in rings is shown. The uncertainty in lifetime estimation is composed of statistical and systematic

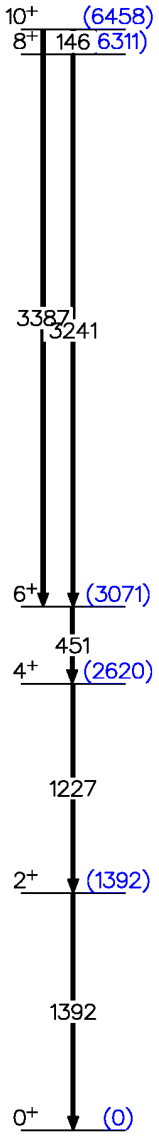

Figure 4.14: Partial level scheme for the ^{54}Ni taken from literature [106].

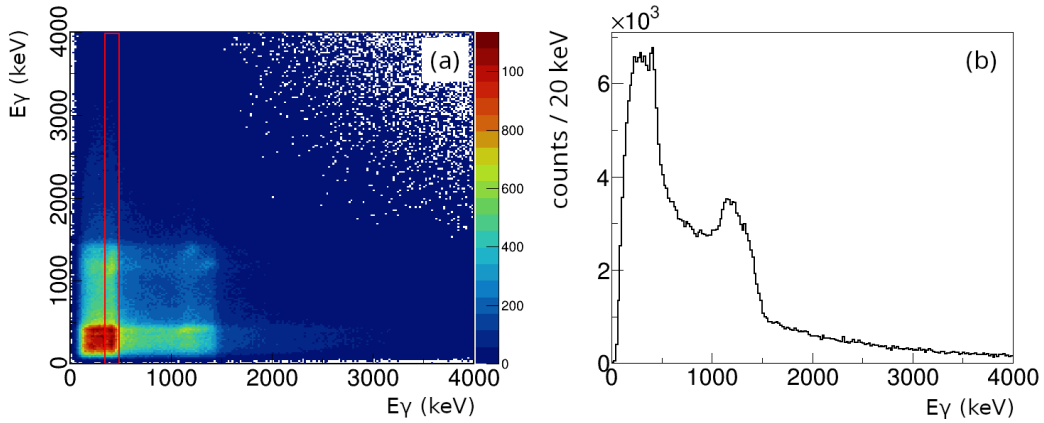

Figure 4.15: (a) Gamma-ray coincidence matrix. The red area corresponds energy used to perform the gate. (b) Gamma-ray spectrum gated on the 451 keV energy. No gamma rays depopulating states above the 6^+ can be observed.

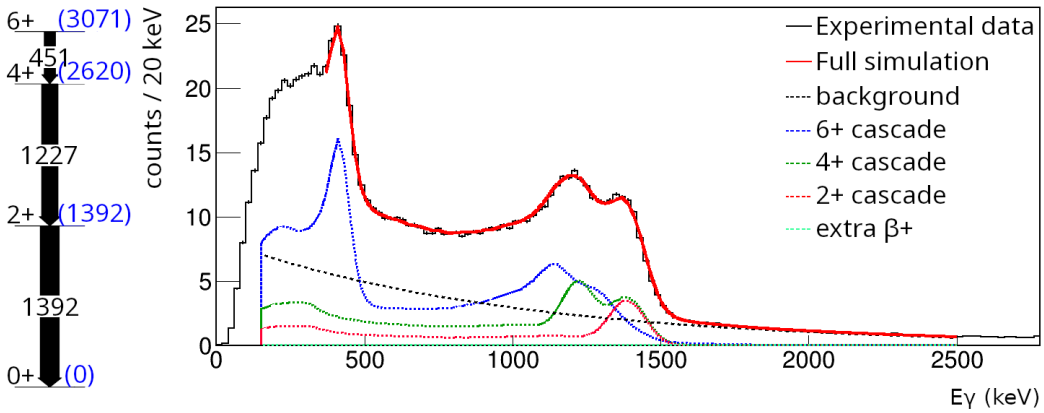

Figure 4.16: Experimental gamma-ray spectrum overlapped with the best fit. It is possible to see the contributions of each cascade to the simulation.

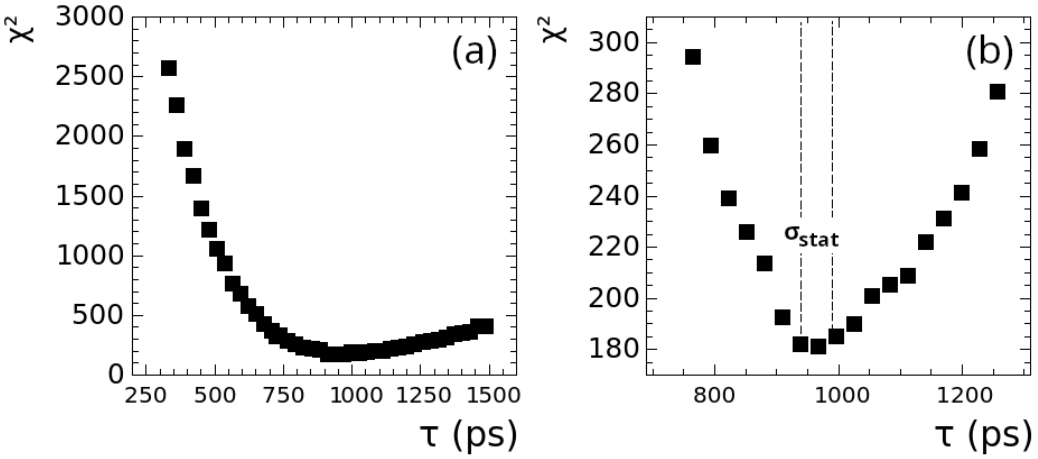

Figure 4.17: (a) χ^2 curve as a function of the lifetime for the fit of the entire spectrum. (b) Zoomed-in χ^2 curve as a function of the lifetime for the fit of the entire spectrum. The vertical dashed lines indicates the χ^2_{min} + 1 range.

components. The statistical uncertainty was estimated by evaluating the χ^2 curve as a function of the lifetime. The obtained τ value and the statistical uncertainty is $\tau^{+sta}_{-sta} = 967^{30}_{25}$ ps. In the present case, the main sources of systematic uncertainty are the uncertainty in the stopping power and the value of the Doppler correction. The estimated mean error for the stopping power of ^{54}Ni in ^{9}Be is 7.8%, according to TRIMM software. The adopted systematic error attributed to the estimated β value is 1.8%, and it was calculated by evaluating the differences caused by the β value in the peaks resolution observed in Figure 4.12. When considering all sources of uncertainty, the value of $\tau = 967^{83}_{81}$ ps is achieved. The reduced transition probability of this associated with this E2 transition is $B(E2) = 45(4)$ e^{2}fm^4. The obtained intensities for the 6+, 4+, and 2+ states are displayed in Table 4.3.

4.5 Shell Model calculation results

Shell model calculations were performed to describe the structure of the ^{54}Ni and its mirror ^{54}Fe. The ANTOINE code has been used with the effective interaction KB3GR, which considers a ^{40}Ca inert core. The excitation energies of the ^{54}Ni for the yrast natural parity states 2^+, 4^+, 6^+, 8^+ and

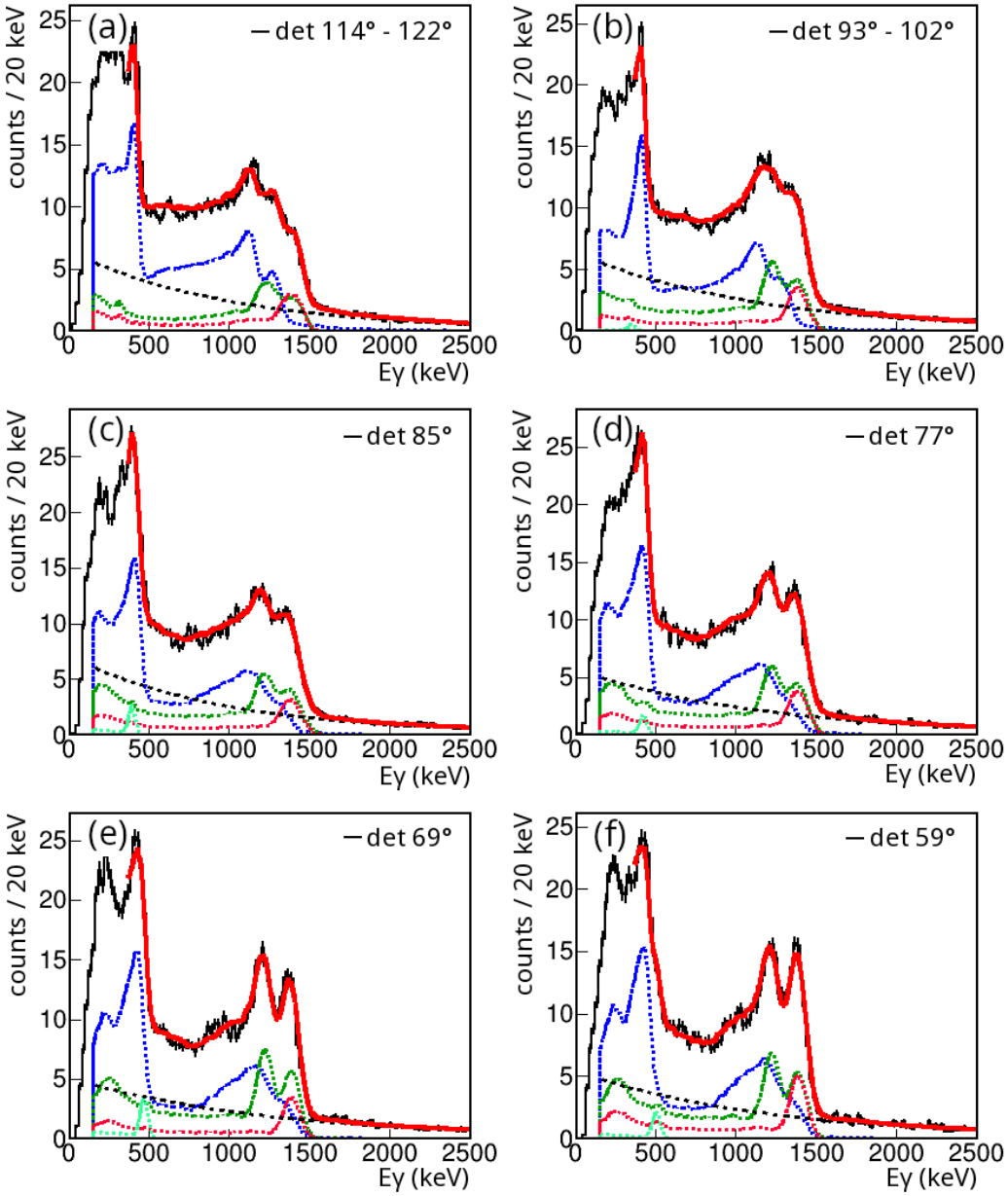

Figure 4.18: Experimental gamma-ray spectrum split in rings according with their angular position. In red, the fitted curve considering all contributions. In dotted blue, the contribution of the 6^+ cascade. In dotted green, the contribution of the 4^+ cascade. In dotted red, the contribution of the 2^+ cascade. In dotted light green, the contribution of β^+ peak.

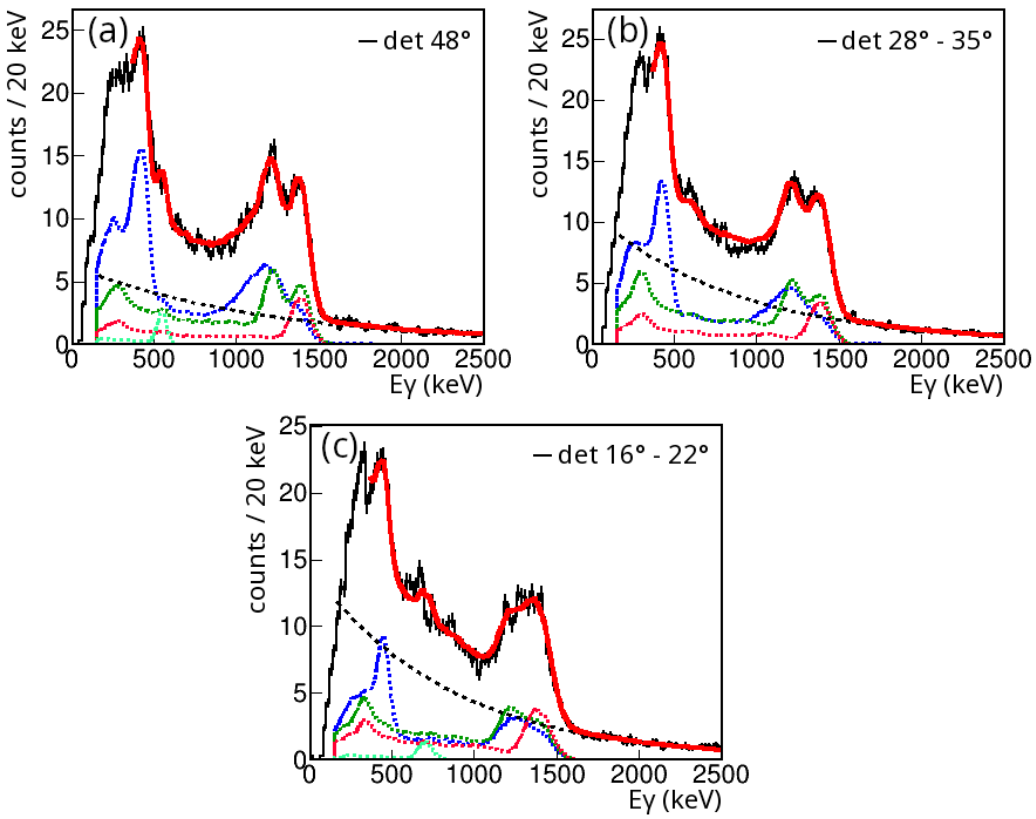

Figure 4.19: Experimental gamma-ray spectrum split in rings according with their angular position. In red, the fitted curve considering all contributions. In dotted blue, the contribution of the 6^+ cascade. In dotted green, the contribution of the 4^+ cascade. In dotted red, the contribution of the 2^+ cascade. In dotted light green, the contribution of β^+ peak.

Table 4.3: Experimental information obtained for the ^{54}Ni

Transition	E_γ (keV)	γ-BR %	Intensity (a.u.)	$\tau_{exp.}$ (ps)	B(E2) (e^2fm^4)
$6^+ \rightarrow 4^+$	451	100	41 (8)	967^{83}_{81} ps	45(4)
$4^+ \rightarrow 2^+$	1227	100	60 (9)		
$2^+ \rightarrow 0^+$	1392	100	68 (6)		

10^+ were calculated by allowing the excitation of 8 protons and 6 neutrons in the full fp space. An analogous calculation was performed for the mirror, ^{54}Fe, by allowing the excitation of 6 protons and 8 neutrons in the full fp space. The Shell Model calculated excitation energies are in good agreement with the experimentally observed values for the two states under investigation. An analogous procedure to the one applied for the mirror pairs A=47 and A=49, discussed in section 3.6, was applied to the ^{54}Ni and ^{54}Fe. The experimental B(E2) values weighted by their uncertainties were compared to the Shell Model calculated ones. A systematic procedure to obtain the value of effective charges for the protons (e_π) and neutrons (e_ν) that better fits the experimental data was applied. Several different combinations of e_π and e_ν in steps of $0.02\,e$ were tested in a grid-search algorithm. The effective charge values that better described simultaneously all three B(E2) values nuclei found by this procedure were $e_\pi = 1.30\,e$ and $e_\nu = 0.58\,e$, matching the values obtained for the other mirror pairs. The comparison between experimental and Shell Model calculations for the electric quadrupole reduced transition probabilities B(E2) using different sets of effective charges are shown in Figure 4.20. The obtained values for the polarization charges deduced from these effective charges were $e^{(0)}_{pol} = 0.44$ and $e^{(1)}_{pol} = 0.14$. The value of $e^{(0)}_{pol}$ is similar to the one obtained by du Rietz et al., in agreement with the Bohr-Mottelson formula 2.24.

In the case of ^{54}Fe, the general tendency of the experimental B(E2) values are well reproduced by the Shell Model calculations for all sets of effective charges. The experimental values for the ^{54}Fe were taken from literature [107]. The $J^\pi = 2^+$ experimental B(E2) lies higher than the Shell Model calculated values for all sets of effective charges. For the other excited states, all sets of effective charges can reproduce the experimentally obtained values. In the case of the ^{54}Ni, the Shell Model calculated B(E2) values are underestimated for all sets of effective charges. The $J^\pi = 2^+$ experimental B(E2) value lies much higher than the Shell Model calculation, indicating a higher degree of collectivity than theoretically predicted. The $J^\pi = 4^+$

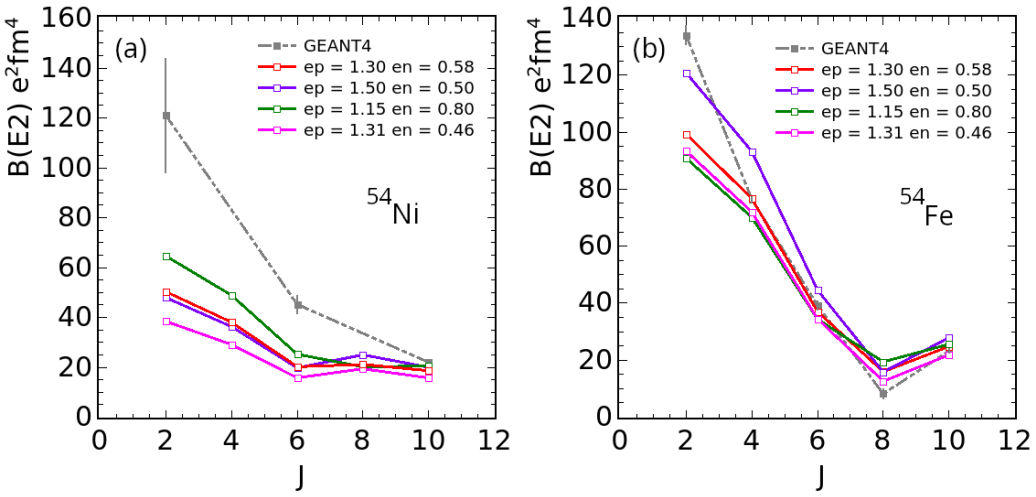

Figure 4.20: (a) B(E2) reduced transition probabilities as a function of the angular momentum for the ^{54}Ni. (b) Same for the ^{54}Fe. The standard adopted values for effective charges $e_\pi = 1.50\,e$ and $e_\nu = 0.50\,e$ are shown in violet. The values deduced by du Rietz et al. are shown in green, and the values deduced by Dufour and Zuker are shown in pink.

experimental B(E2) value was not obtained because the lifetime is out of reach for the employed technique. The Shell Model calculations predict a B(E2) value for the $J^\pi = 4^+$ raging from 28 to 50 e^{2}fm^4, which translates in lifetimes predicted to range from 5 to 10 ps. The $J^\pi = 6^+$ experimental B(E2) also lies higher than the Shell Model predicted value. The $J^\pi = 8^+$ experimental B(E2) value was not obtained because this state was not populated in the present work and the lifetime would be out of reach for the employed technique. The Shell Model calculations predict a B(E2) value for the $J^\pi = 8^+$ raging from 18 to 25 e^{2}fm^4, which translates in lifetimes predicted to range from 90 to 125 fs. An experimental measurement of the lifetime of both $J^\pi = 4^+$ and $J^\pi = 8^+$ state would help to determine which set of effective charges would better reproduce the experimental data. The $J^\pi = 10^+$ experimental value was taken from Rudolf et al.[106] and shows a resonable agreement with the Shell Model calculations considering the standard values for the effective charges and for the values derived by du Rietz et

al. The experimental and Shell Model calculated values are consistent with a nucleus losing its collective behavior as the B(E2) values get smaller with the increase of angular momentum.

Chapter 5

Conclusions

In this work, two different experiments, populating excited states in nuclei in the fp shell, were presented. In the first one, the lifetimes of analogue excited states for the mirror pairs ^{47}Cr - ^{47}V and ^{49}Mn - ^{49}Cr were measured. Excited states in these nuclei were populated using a fusion-evaporation reaction in which a 115 MeV beam of ^{36}Ar bombarded a target composed by 0.55 mg/cm^2 CaO and a 10 mg/cm^2 thick gold backing to stop the recoil nuclei. The gamma rays following the deexcitation of the produced nuclei were detected using AGATA gamma-ray spectrometer. The particles evaporated in the reaction were detected by the ancillary detectors DIAMANT, NEDA, and Neutron Wall. The high efficiency of the detection equipment allowed the selection and identification of gamma rays coming from weakly populated proton-rich nuclei, such as the ^{47}Cr and ^{49}Mn. Excited states lifetimes in the subpicosecond range were determined using the Doppler Shift Attenuation Method. The lifetimes for three excited states in the ^{47}Cr were obtained confirming the known values from the literature, and the lifetimes of four excited states in the ^{49}Mn were determined for the first time. The lifetimes of excited states in their correspondent mirror pairs, ^{47}V and ^{49}Cr, were also obtained and validated in the adopted procedure by confirming the values found in the literature. The experimentally reduced quadrupole electric transition probability B(E2) values were obtained from the experimental lifetime values. The structure of the four nuclei was calculated with the Shell Model using the ANTOINE code and the KB3G-coul effective interaction.

The ^{47}Cr Shell Model calculated excitation energies presented an inversion between the $17/2^-$ and $19/2^-$ with respect to the experimentally observed ones, while the ^{47}V experimental excitation energies are in good agreement with the Shell Model calculations. The Shell model calculated excitation energies of both ^{49}Mn and ^{49}Cr are in good agreement with the experimentally obtained ones. The effective charges appear in the Shell Model to account for the polarization effects caused by the valence nucleons on the inert core. The comparison between experimental B(E2) values and Shell Model calculated ones, allowed the determination of the best set of effective charges to simultaneously describe the B(E2) of all four nuclei using least squares fit. The obtained effective charges slightly underestimated the experimental B(E2) values of the ^{47}Cr while well describing the B(E2) values for the ^{47}V. A discrepancy between experimental B(E2) and Shell Model calculated values for the ^{49}Mn was found while the values for the ^{49}Cr are in good agreement with the experimental ones. This happened because Shell Model B(E2) values for the ^{49}Mn and ^{49}Cr nuclei are almost identical, which suggests that the model predicts very similar excited state lifetimes and transition energies for them. However, the experimental results indicated otherwise, with the ^{49}Mn having larger B(E2) values. Further experimental studies strongly populating excited states in the ^{49}Mn would help clarify the reasons for such difference. The obtained effective and polarization charges are slightly better to describe the B(E2) values for the four nuclei as the standard adopted ones.

The second experiment obtained the lifetime of 6^+ excited state of the ^{54}Ni. Low spin states in the ^{54}Ni were populated in one neutron knockout reaction between a beam of ^{55}Ni and a 6 mm thick ^{9}Be target. The ^{55}Ni beam was produced by fragmentation and was separated and selected using BigRIPS separator. The gamma rays emerging from the reaction of the beam with the target were detected with DALI2+ spectrometer. Further selection was achieved by tagging on the reaction products with the ZeroDegree spectrometer. The high detection efficiency and the unique capabilities of this experimental setup allowed the lifetime of the 6^+ excited state of the

^{54}Ni to be determined by fitting the Doppler broadening caused by the in-flight emission of gamma rays. The fitting procedure was performed using GEANT4 simulations to reproduce the observed experimental shape. Shell Model calculations were performed for the B(E2) values of the ^{54}Ni and its mirror ^{54}Fe. For the ^{54}Ni, the theoretical calculations underestimated the B(E2) values for the states under investigation, while for the ^{54}Fe the Shell Model calculations are in good agreement with the experimental data for all set of effective charges, except for the 2^+ state. The Shell Model calculations also allowed a prediction of the lifetime values of the 4^+ and 8^+ states of the ^{54}Ni.

In conclusion, the lifetimes of mirror nuclei in the fp shell have been measured. Experimental data from two different experiments have been analyzed and compared with Shell Model calculations, allowing the determination of a set of effective charges that better describes these nuclei in the fp shell. Further experiments measuring lifetimes of excited states in the studied nuclei and in this mass region could would be useful to test Shell Model theoretical predictions and refine the obtained values for the effective charges.

Appendix A

AGATA Event Structure

A.1 AGATA data flow

The signals generated in AGATA and its ancillary arrays are digitized and sent to be processed by the data acquisition system (DAQ). Then, the digitized traces received system are processed by several algorithms until the storage of reconstructed events [18]. NARVAL[1] is the software responsible to handle the data flow and the processing algorithms are called actors in its terminology [108]. Although NARVAL is written in ADA language its actors can load C/C++ shared libraries, allowing the implementation of a distributed system for processing the data, taking advantage of multiple CPU cores and computers in a network, so different actors can run across different computers. The NARVAL actors are grouped together according to their function on the processing chain, namely filters, dispatchers, or consumers, each type playing a different role. NARVAL process the data flow using a chain of different actors, for instance, the producer actors delivers useful data to the filter actors, which delivers data to the consumer actors, which are responsible for dumping the data on disk (Figure A.1). The selection of actors in a chain is read from a topology file provided by the user and determines the behavior of the acquisition and data processing systems. By providing different topology files, a chain of actors can be used to acquire data during the experiment or reprocess already acquired data after the experiment. The

[1] Nouvelle Acquisition temps-Réel Version 1.2 Avec Linux

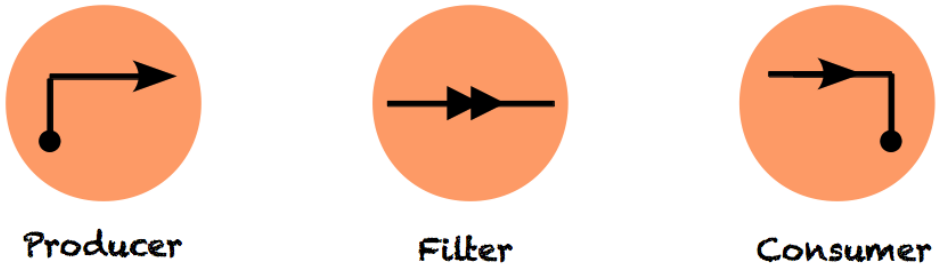

Figure A.1: NARVAL actors simplified diagram. Taken from [109].

available NARVAL actors can be summarized as: [110, 111]

- **Producer actors**
  - CrystalProducerATCA which reads the traces, regardless of whether they are coming directly from the front-end electronics (online, during the experiment) or a set of stored cdat format trace files (offline, after the experiment);
  - BasicAFP which starts a replay from already processed data allowing further filter call without recreating data from the traces;
- **Filter actors**
  - PreprocessingFilterPSA which applies energy and time calibrations, corrections and alignment;
  - PSAFilter which executes the Pulse Shape Analysis (PSA) algorithm, extracting the position of the interaction points from preprocessed data;
  - PostPSAFilter which performs the final corrections needed after PSA, like time alignment, neutron damage correction and energy recalibration;
  - TrackingFilterOFT which performs the tracking algorithm from the interaction points obtained by the PSA;

  - BasicATSB which builds events in a given time window, mainly used for the ancillary detectors events;

- **Dispatcher actors**

  - EventBuilder which builds AGATA events in a given time window;
  - EventMerger which builds together the ancillary and AGATA events in a given time window;

- **Consumer actors**

  - BasicAFC which finishes a data processing chain and write the processed information on disk (such as gamma-ray energies and hits information) in the adf format;
  - TreeBuilder which finishes a data processing chain and creates a ROOT Tree object with the processed data;
  - None which finishes a data processing chain without writing output files;

NARVAL calls its actors by reading topology files, which are different for online and offline data processing. A representation of topology files containing the sequence of actors that can be used to process online and offline data can be observed in the figures A.2 and A.3, respectively. For computational

Figure A.2: Graphical representation of NARVAL topology file, with actor names. In this example, NARVAL reads the traces coming from the front-end electronics, then applies the pre-processing and PSA filters and after dumps the gamma-ray information into adf files. Adapted from [110].

details about the data processing and Actors, refers to [109].

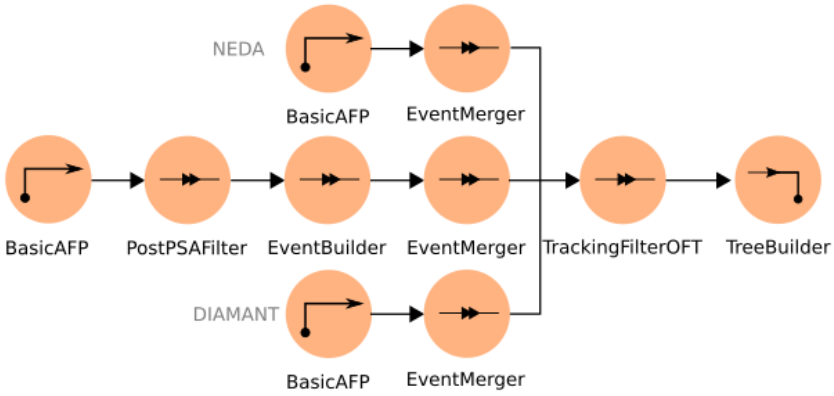

Figure A.3: Graphical representation of NARVAL topology file, with actor names. In this example, NARVAL reads adf files stored on disk to apply the post-PSA filter, builds AGATA events, reads and merges ancillary detectors events with the AGATA ones, implements tracking algorithms, and dumps the built events into a ROOT Tree object. This topology was utilized to perform the offline data processing of this work.

For convenience, the data processing procedure is divided in two ways, online and offline procedures. The online data processing is crucial for the experiment as it is responsible for data acquisition and storage. When signals pass the hardware trigger conditions, they are sent to the online data processing, where the signals are handled by the actors contained in the online topology file. There are two objectives to be achieved by the online procedure: to permit supervision and control over the experiment by allowing real-time access to the data as it is being acquired, and the reliable storage of the reconstructed events. A topology file defines the producer, filter, and consumer actors, as illustrated in figure A.2. The given example allows to record not only the reconstructed events after PSA, but also the digitized traces themselves, granting further flexibly, given the possibility of reprocessing the entire experiment from the digitized signals. Due to disk space limitations and data throughput, recording traces alongside the PSA data may become unpractical with certain trigger conditions, for this reason, it may be useful to perform calibration runs with full trace recording and establish the best parameters for the PreprocessingFilterPSA filter, then the

experiment can run and store only the PSA processed data.

The offline procedure can reprocess the experimental data after acquisition, eventually using a different set of parameters, in order to obtain suitable data to analyse. This replay is generally performed with more strict conditions on filters, times and coincidences than during the online procedure, as an experiment can not be repeated multiple times just to find the adequate set of parameters. Some strict conditions can also be applied at trigger level. The offline replays were performed with FEMUL (Flat EMULator), which is a software that emulates the NARVAL functionality and is able to run complex topologies [110]. The offline procedure is responsible for calling the PostPSAFilter which performs the last adjustments before applying the tracking filter, such as time alignments, energy recalibration and neutron damage correction. After all the corrections the data can be delivered to TrackingFilterOFT which implements the tracking algorithm described in 3.1.4. NARVAL (and its emulator) process not only AGATA data but also data from the ancillary detectors, in the offline procedure the reprocessing of data can be performed individually for each type of detector without building the event globally, which is called Local Level Processing (LLP). The LLP can save time during data processing as building only gamma rays, neutron or charged particle events to verify data consistency and parameters correctness, taking considerably less time than building entire events to perform the same task. However, in order to have a complete event the Global Processing Procedure is necessary, given that the data from AGATA + ancillaries must be merged together to it [112].

A typical event built during the data processing procedure must contain information from the incident gamma-ray radiation and may include ancillary detector data. The processed events were dumped into ROOT Tree objects, combining the event information into variables that facilitate plotting and the imposition of conditions on the data. Figure A.4 shows an example of a processed event, the variables and their content can be briefly described in the following list:

- **nbHits**: contains the number of gamma-ray interactions;
- **hitE**: contains the energies in keV of each gamma-ray interaction;
- **hitGX, hitGY, hitGZ**: contains the x, y and z position in millimeters of each gamma-ray interaction points;
- **hitId**: contains the id of the crystals hit by the gamma-rays;
- **hitSg**: contains the id of the segments hit by the gamma-rays;
- **nbCores**: contains the number of crystals with gamma-ray interaction events;
- **nbHitsperCry**: contains the number of gamma-ray interactions recorded per crystal;
- **coreId**: contains the id of the crystals with gamma-ray interaction events;
- **coreE0**: contains the energy in keV of each gamma-ray interaction collected by the core contact;
- **coreTS**: contains the timestamp of each gamma-ray interaction collected by the core contact;
- **TSHit**: contains the global timestamp for the event;
- **nbTrack**: contains the number of tracked gamma-ray energies in the event;
- **trackE**: contains the gamma-ray energies in keV obtained with the tracking algorithm;
- **trackX1, trackY1, trackZ1**: contains the x, y and z position in millimeters of the tracking gamma-ray interactions;
- **trackT**: contains the time of each tracking event;

- **trackCrystalID**: contains the id of the crystals with tracking energies;
- **TStrack**: contains the global timestamp for tracking;
- **nbNEDA**: contains the number of interactions on NEDA;
- **BoardId**: contains the id number of the NUMEXO board that fired;
- **ChannelId**: contains the id number of the channel that fired in a given NUMEXO board;
- **NEDAId**: contains the id number of the NEDA detector;
- **NEDA_Tdc**: contains the value of NEDA TDC;
- **NEDAEnergy**: contains the uncalibrated energy of NEDA;
- **NEDAFast, NEDASlow**: contains the integral of the fast and slow components of the incident signal, respectively;
- **TSNEDA_Hit**: contains the timestamp of the interactions on NEDA;
- **TSNeda**: contains the global timestamp of the NEDA event;
- **nbDIAMANT**: contains the number of interactions on DIAMANT;
- **DIAMANTBoard**: contains the id number of the NUMEXO board that fired;
- **DIAMANTChannel**: contains the id number of the channel that fired in a given NUMEXO board;
- **DIAMANTd**: contains the id number of the DIAMANT detector;
- **DIAMANT_E**: contains the uncalibrated energy of DIAMANT;
- **DIAMANT_PID**: contains the particle identification number for DIAMANT;

- **DIAMANT_Hit**: contains the timestamp of the interactions on DIAMANT;
- **TSDIAMANT**: contains the global timestamp of the DIAMANT event;

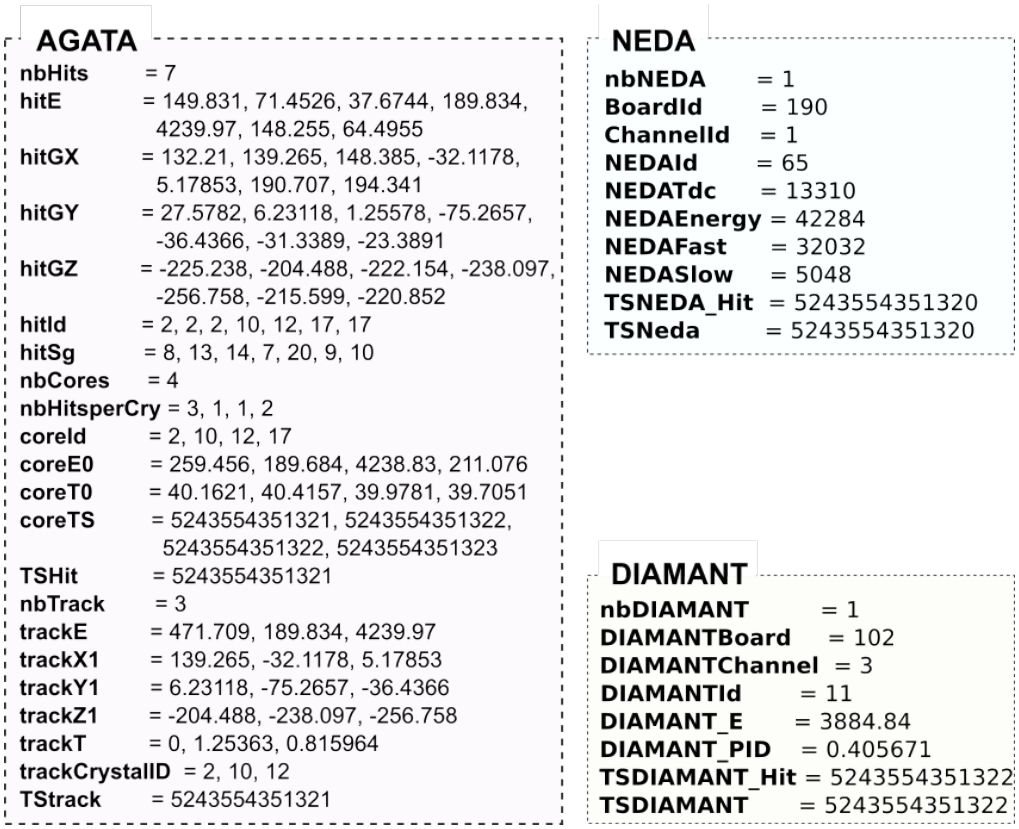

Figure A.4: Example of the main set of information contained in an event after post-PSA. The information is shown with its original name as recorded on disk by the TreeBuilder actor.

Bibliography

[1] K. Brading and E. Castellani, *Symmetries in Physics: Philosophical Reflections*. Cambridge University Press, 2003.

[2] M. A. Bentley and S. M. Lenzi, "Coulomb energy differences between high-spin states in isobaric multiplets," *Progress in Particle and Nuclear Physics*, vol. **59**, pp. 497–561, 2007.
doi:**10.1016/j.ppnp.2006.10.001**.

[3] J. Chadwick, "The existence of a neutron," *Proc. R. Soc. Lond. A*, vol. **136**, pp. 692–708, 1932.
doi:**10.1098/rspa.1932.0112**.

[4] W. Heisenberg, "On the structure of atomic nuclei. i.," *Z. Phys.*, vol. **77**, 1932.

[5] D. Iwanenko, "The neutron hypothesis," *Nature*, vol. **129**, no. 798, 1932.

[6] E. Majorana *N. Cimento*, vol. **9**, no. 43, 1932.

[7] D. H. Wilkinson, *Isospin in Nuclear Physics*. North-Holland Publishing Company - Amsterdam, 1969.

[8] M. A. Bentley *et al.*, "Isospin-breaking interactions studied through mirror energy differences," *Physical Review C*, vol. **92**, no. 024310, 2015.
doi:**10.1103/PhysRevC.92.024310**.

[9] D. Tonev *et al.*, "Isospin dependence of electromagnetic transition strengths among an isobaric triplet," *Physics Letters B*, vol. **797**,

no. 134835, 2019.
doi:**10.1016/j.physletb.2019.134835**.

[10] J. A. Cameron *et al.*, "Mirror nuclei at high spin in the f7/2 shell," *Physics Letters B*, vol. **319**, pp. 58–62, 1993.

[11] F. Brandolini, "Mirror energy differences and nuclear structure in f7/2 nuclei," *The European Physical Journal A*, vol. **41**, pp. 115–124, 2009.
doi:**10.1140/epja/i2009-10774-9**.

[12] D. Tonev *et al.*, "Transition rates and nuclear structure changes in mirror nuclei ^{47}Cr and ^{47}V," *Physical Review C*, vol. **65**, no. 034314, 2002.
doi:**10.1103/PhysRevC.65.034314**.

[13] J. A. Cameron *et al.*, "Progress in particle and nuclear physics," *Physics Letters B*, vol. **235**, no. 3-4, 1990
doi:**10.1016/0370-2693(90)91957-D**.

[14] J. A. Cameron *et al.*, "Recoil-separated gamma-ray spectroscopy of ^{47}Ti, ^{47}V, ^{47}Cr, ^{48}V and ^{48}Cr," *Physical Review C*, vol. **49**, no. 3, 1994
doi:**10.1103/physrevc.49.1347**.

[15] C. D. O'Leary *et al.*, "Mirror symmetry up to the band termination in ^{49}Mn and ^{49}Cr," *Physical Review Letters*, vol. **79**, no. 22, 1997
doi:**10.1103/PhysRevLett.79.4349**.

[16] S. Lenzi *et al.*, "Coulomb Energy Differences in T=1 mirror rotational bands in ^{50}Fe and ^{50}Cr," *Physical Review Letters*, vol. **87**, no. 12, 2001.
doi:**10.1103/PhysRevLett.87.122501**.

[17] D. Rudolph *et al.*, "Mirror symmetry at mass A=54: E4 effective charges near doubly magic ^{56}Ni," *Physics Letters B*, vol. **830**, no. 137144, 2022.
doi:**10.1016/j.physletb.2022.137144**.

[18] S. Akkoyun *et al.*, "AGATA—advanced gamma tracking array," *Nuclear Instruments and Methods in Physics Research A*, vol. **668**, pp. 26–58, 2012.
doi: **10.1016/j.nima.2011.11.081**.

[19] T. Kubo, "In-flight RI beam separator BigRIPS at RIKEN and elsewhere in Japan," *Nuclear Instruments and Methods in Physics Research B*, vol. **204**, pp. 97–113, 2003.
doi:**10.1016/S0168-583X(02)01896-7**.

[20] S. Takeuchi *et al.*, "DALI2: A Nai(Tl) detector array for measurements of γ rays from fast nuclei," *Nucl. Instrm. Methods Phys. Res. Section A*, vol. **763**, pp. 596–603, 2014.
doi:**10.1016/j.nima.2014.06.087**.

[21] I. Murray *et al.*, "DALI2+ at the RIKEN nishina center RIBF," *RIKEN Accel. Prog. Rep.*, vol. **51**, p. 158, 2018.

[22] T. Kubo *et al.*, "BigRIPS separator and ZeroDegree spectrometer at RIKEN RI Beam Factory," *Prog. Theor. Exp. Phys.*, vol. **03C003**, 2012.
doi:**10.1093/ptep/pts064**.

[23] S. S. M. Wong, *Introductory Nuclear Physics.* Wiley-VCH Verlag GmbH & Co. KGaA, Weinheim, 2004.

[24] M. G. Mayer, "On closed shells in nuclei. II," *Physical Review Letters*, vol. **75**, pp. 1969–1970, 1949.
doi:**10.1103/PhysRev.75.1969**.

[25] O. Haxel, J. H. D. Jensen, and H. E. Suess, "On the magic numbers in nuclear structure," *Physical Review Letters*, vol. **75**, p. 1766, 1949.
doi:**10.1103/PhysRev.75.1766.2**.

[26] D. L. Toufen, "Sistema para medida de estados isoméricos," Master's thesis, Universidade de São Paulo, 2008.

[27] R. F. Casten, *Nuclear Structure From A Simple Perspective.* Oxford University Press, 1990.

[28] K. S. Krane, *Introductory Nuclear Physics.* John Wiley & Sons Inc., 1988.

[29] E. Caurier, "Shell model and nuclear structure," *Progress in Particle and Nuclear Physics*, vol. **59**, pp. 226–242, 2007. doi:**10.1016/j.ppnp.2006.12.012**.

[30] E. Caurier, G. Martinez-Pinedo, F. Nowacki, A. Poves, and A. P. Zuker, "The shell model as a unified view of nuclear structure," *Reviews of Modern Physics*, vol. **77**, pp. 427–488, 2005.

[31] F. Nowacki and E. Caurier, "Shell model and nuclear structure far from stability," *Reviews of Modern Physics*, vol. **30**, no. 3, pp. 749–753, 1999.

[32] P. R. P. Allegro, *Sistemática de núcleos ímpar- ímpar de Ga na região de massa A = 60 - 70.* PhD thesis, Universidade de São Paulo, 2013.

[33] A. Poves, "Shell model study of the isobaric chains A = 50, A = 51 and A = 52," *Nuclear Physics A*, vol. **694**, pp. 157–198, 2001.

[34] *KB3GR interaction.* Private communication.

[35] E. P. Wigner *Proceedings of the Robert A Welch Conference on Chemical Research*, vol. **1**, no. 67, 1957.

[36] A. Boso, *Study of Isospin Symmetry Breaking effects in the A=23 and A=46 multiplets.* PhD thesis, Università Degli Studi di Padova, 2017.

[37] J. A. Nolen *et al. Ann. Rev. Nucl. Sci.*, vol. 19, no. 471, 1969.

[38] K. Okamoto, "Coulomb energy of 3He and possible charge asymmetry of nuclear forces," *Physics Letters*, vol. 11, pp. 150–153, 1964. doi:**10.1016/0031-9163(64)90650-X**.

[39] P. V. Isacker, *Measuring isospin mixing from E1 and E2 transitions.* PhD thesis, Isospin symmetry, 2011.

[40] E. K. Warburton *et al.*, *The role of isospin in electromagnetic transitions.* North Holland Pub. Co., Amsterdam, 1969.

[41] R. du Rietz *et al.*, "Effective charges in the fp shell," *Physical Review Letters*, vol. 93, no. 222501, 2004.

[42] M. N. Harakeh and A. van der Woude, *Systematic of isovector and isoscalar giant quadrupole resonances in normal and superfluid spherical nuclei.* Clarendon Press, Oxford, 2001.

[43] M. Hunyadi *et al.*, "Giant resonance overtones: Compression modes of the nucleus," *Nuclear Physics News*, vol. 18, no. 1, 2008.

[44] A. Bohr and B. R. Mottelson, *Nuclear Structure, Volume II - Nuclear Deformations.* World Scientific Publishing Co. Pte. Ltd., 1998.

[45] V. Metag *et al.*, "Nuclear structure and reactions studied with the Darmstadt-Heidelberg Crystal Ball," *International Symposium on Heavy Ion Physics*, vol. **763**, 1984.

[46] P. L. Nolan *et al.*, "Large arrays of escape-suppressed gamma-ray detectors," *Annu. Rev. Nucl. Part. Sci.*, vol. 45, pp. 561 – 607, 1994.

[47] P. J. Twin *et al.*, "Tessa : A multi-detector gamma-ray array designed to study high spin states," *Nuclear Physics A*, vol. **409**, pp. 343–352, 1983.

[48] D. Bazzacco *Procedings of conference on the physics from Large γ-ray detector arrays*, vol. **694**, p. 376, 1992.
Chalk River, Ontario, Canada.

[49] C. R. Alvarez, "The GASP array," *Nuclear News Europe*, vol. **2**, no. 10, 1993.

[50] C. R. Alvarez, "The EUROBALL array," *Nuovo Cimento A*, vol. **111**, no. 601, 1998.

[51] J. Simpson, "The EUROBALL spectrometer," *Zeitschrift für Physik*, vol. **358**, no. 139, 1997.

[52] R. Diamond, "Gamma-sphere proposal," *Lawrence Berkley National Laboratory Report*, vol. **5202**, no. 139, 1997.

[53] I. Y. Lee, "The gamasphere," *Nuclear Physics A*, vol. **520**, pp. 641–655, 1990.

[54] F. Recchia, *In-beam test and imaging capabilities of the AGATA prototype detector*. PhD thesis, Università Degli Studi di Padova, 2008.

[55] N. Medina, "In-beam gamma-ray spectroscopy with GASP," *Acta Physica Hungarica - Heavy Ion Physics 2*, pp. 141–159, 1995.

[56] Division of Nuclear Physics, The DOE/NSF Nuclear Science Advisory Committee, U.S. Department of Energy, Office of Science, Opportunities in Nuclear Science, DOE Long Range Plan, 2002.

[57] *Technical Design Report*. Internal communications, 2008.
AGATA Collaboration.

[58] G. F. Knoll, *Radiation Detection and Measurement*. John Wiley & Sons, 1989.

[59] C. Michelagnoli, *The lifetime of the 6.79 MeV state in ^{15}O as a challenge for nuclear astrophysics and γ-ray spectroscopy: a new DSAM measurement with the AGATA Demonstrator array*. PhD thesis, Università Degli Studi di Padova, 2013.

[60] G. J. Schmid *et al.*, "A γ-ray tracking algorithm for the greta spectrometer," *Nuclear Instruments and Methods in Physics Research A*, vol. **430**, pp. 69–83, 1999.

[61] J. Scheurer *et al.*, "Improvements in the in-beam y-ray spectroscopy provided by an ancillary detector coupled to a Ge γ-spectrometer:the DIAMANT-EUROGAM ii example," *Nuclear Instruments and Methods in Physics Research A*, vol. **385**, pp. 501–510, 1997.

[62] J. Gal *et al.*, "The VXI electronics of the DIAMANT particle detector array," *Nuclear Instruments and Methods in Physics Research A*, vol. **516**, pp. 502–510, 2004.

[63] J. J. Valiente-Dobón *et al.*, ": NEDA—neutron detector array," *Nuclear Instruments and Methods in Physics Research Section A*, vol. **927**, pp. 81–86, 2019.
doi: **10.1016/j.nima.2019.02.021**.

[64] O. Skeppstedta, ": Neda—neutron detector array," *Nuclear Instruments and Methods in Physics Research Section A*, vol. **421**, no. 3, pp. 531–541, 1999.

[65] G. Jaworski *et al.*, "Simulations of fusion-evaporation reactions with agata and ancillary detectors," *Warsaw University Heavy Ion Laboratory Annual Report*, pp. 57–59, 2007.

[66] O. Skeppstedt *et al.*, "The euroball neutron wall – design and performance tests of neutron detectors," *Nuclear Instruments and Methods in Physics Research A*, vol. 421, pp. 531 – 541, 1999.

[67] H. Morinaga and T. Yamazaki, *In-Beam Gamma-Ray Spectroscopy.* North-Holland Publishing Company, 1976.

[68] F. Brandolini *et al.*, "Precise DSAM lifetime measurements in ^{48}Cr and ^{50}Cr as a test of large scale shell model calculations," *Nuclear Physics A*, vol. **642**, pp. 387–406, 1998.
doi:**10.1016/S0375-9474(98)00543-0**.

[69] D. Branford and I. F. Wright, "A Doppler shift attenuation method for measuring lifetimes in the range 10^{-13} - 10^{-15} s using heavy-ion induced

reaction," *Nuclear Instruments and Methods*, vol. **106**, pp. 437–443, 1973.

[70] B. Bruyneel *et al.*, "Correction for hole trapping in AGATA detectors using pulse shape analysis," *The European Physical Journal A*, vol. 49, no. 61, 2013.

[71] C. A. Kalfas *et al.*, "SPECTRW: A software package for nuclear and atomic spectroscopy," *Nuclear Instruments and Methods in Physics Research A*, vol. **830**, pp. 265–274, 2016.

[72] D. C. Radford, "Background subtraction from in-beam hpge coincidence data sets," *Nuclear Instruments and Methods in Physics Research A*, vol. **361**, pp. 306–316, 1995.

[73] C. Ryan, "SNIP, a statistics-sensitive background treatment for the quantitative analysis of PIXE spectra in geoscience applications," *Nuclear Instruments and Methods in Physics Research Section B*, vol. **34**, no. 3, pp. 396–402, 1988.
doi: **10.1016/0168-583X(88)90063-8**.

[74] M. Morháč *et al.*, "Background elimination methods for multidimensional coincidence γ-ray spectra," *Nuclear Instruments and Methods in Physics Research A*, vol. **401**, pp. 113–132, 1997.

[75] P. A. Söderström *et al.*, "Digital pulse-shape discrimination of fast neutrons and γ-rays," *Nuclear Instruments and Methods in Physics Research A*, vol. **594**, pp. 79–89, 2008.
doi: **10.1016/j.nima.2008.06.004**.

[76] G. R. Gilmore, *Practical Gamma-ray Spectrometry*. John Wiley Sons, Ltd., 2008.

[77] J. C. Wells and N. R. Johnson, "Lineshape: A computer program for doppler-broadened lineshape lifetime analysis," *Report No. ORNL-6689*, vol. **44**, 1991.

[78] F. Brandolini and R. V. Ribas, "Doppler shift attenuation method analysis with the narrow gate on transitions below procedure," *Nuclear Instruments and Methods in Physics Research Section A*, vol. **417**, no. 1, pp. 150–157, 1998. doi:**10.1016/S0168-9002(98)00653-6**.

[79] J. Lindhard *et al. Mat.-Fys. Medd. Dan. Vid. Selsk*, vol. **33**, p. 14, 1963.

[80] L. C. Northcliffe and R. Schilling, "Range and stopping-power tables for heavy ions," *Nuclear Data Tables A 7*, pp. 233–463, 1970. doi:**10.1016/S0092-640X(70)80016-X**.

[81] S. Sie *et al.*, "Measurement of lifetimes for high spin states in 152Sm, 154Gd and 156Gd by the doppler broadened lineshape method," *Nuclear Physics A*, vol. **221**, pp. 443–458, 1977. doi:**10.1016/0375-9474(77)90331-1**.

[82] S. Agostinelli *et al.*, "Geant4 - a simulation toolkit," *Nuclear Instruments and Methods in Physics Research A*, vol. **506**, no. 3, pp. 250–303, 2003. doi: **10.1016/S0168-9002(03)01368-8**.

[83] E. Farnea *et al.*, "Conceptual design and monte carlo simulations of the agata array," *Nuclear Instruments and Methods in Physics Research A*, vol. **621**, pp. 331–343, 2010. doi: **10.1016/j.nima.2010.04.043**.

[84] P. A. Söderström *et al.*, "Interaction position resolution simulations and in-beam measurements of the agata HPGe detectors," *Nuclear Instruments and Methods in Physics Research A*, vol. **638**, pp. 96–109, 2011. doi: **10.1016/j.nima.2011.02.089**.

[85] J. Pellumaj, "Lifetimes measurement in the f7/2 shell using the AGATA spectrometer," Master's thesis, Università Degli Studi di Padova, 2020.

[86] O.B.Tarasov *et al.*, "Development of the program LISE: Application to fusion-evaporation," *Nuclear Instruments and Methods in Physics Research B*, vol. **204**, pp. 174–178, 2008.
doi:**10.1016/S0168-583X(02)01917-1**.

[87] A. A. Pakou *et al.*, "Onset of collectivity in the ground-state band of 50Cr," *Physical Review C*, vol. **50**, p. 2608, 1994.
doi:**10.1103/PhysRevC.50.2608**.

[88] H. Hellmeister *et al.*, "Statistical model calculations of continuum feeding times in heavy-ion fusion reactions," *Nuclear Physics A*, vol. 307, no. 3, pp. 515–532, 1978.

[89] F. Cristancho *et al. Nuclear Physics A*, no. 501, pp. 118–136, 1989.

[90] F. Brandolini *et al.*, "Lifetimes in the middle of 1f7/2 shell:cross-conjugated nuclei ^{47}V and ^{49}Cr," *Nuclear Physics A*, vol. **693**, p. 517–532, 2001.

[91] M. Dufour *et al.*, "Realistic collective nuclear hamiltonian," *Nuclear Physics A*, vol. 54, no. 4, 1996.

[92] F. Brandolini *et al.*, "Electromagnetic transitions and structure in the z=n nucleus 46V," *PHYSICAL REVIEW C*, vol. 64, no. 044307, 2001
doi:**10.1103/PhysRevC.64.044307**.

[93] R. Hoischen *et al. Journal of Physics G: Nuclear and Particle Physics*, vol. 38, no. 035104, p. 17, 2011.

[94] M. Ferraton *et al. The European Physical Journal A*, vol. 35, pp. 167–170, 2008.

[95] S. Lenzi *Internal communication*, 2022.

[96] S. A. Gronemeyer *et al. Phys. Rev. C*, vol. 21, no. 1290, 1980.

[97] F. J. Lynch *et al. Physics Letters B*, vol. 32, no. 1, pp. 38–40, 1970.

[98] C. M. Werneth *et al.*, "Relativistic abrasion–ablation de-excitation fragmentation model," *Nuclear Instruments and Methods in Physics Research Section B*, vol. 502, no. 1, pp. 118–135, 2021
doi:**10.1016/j.nimb.2021.06.016**.

[99] J. D. Bowman *et al. In: unpublished report LBL-2908*, 1973.

[100] L. Olivier, *Nuclear structure in the vicinity of 78Ni : in-beam gamma-ray spectroscopy of 79Cu through proton knockout*. PhD thesis, Université Paris-Saclay, 2017.

[101] M. L. C. Sua, *Inelastic scattering of Ni and Zn isotopes off a proton target*. PhD thesis, Fachbereich Physik der Technischen Universität Darmstadt, 2016.

[102] S. Pigliapoco, "Isospin symmetry in the fp-shell mirror nuclei," Master's thesis, Università Degli Studi Di Padova, 2020.

[103] M. Lettmann, *Spectroscopy of neutron-rich germanium and krypton isotopes - A quest of triaxiality*. PhD thesis, Fachbereich Physik Institut für Kernphysik, 2018.

[104] N. Imai *et al.*, "Anomalously hindered E2 strength," *Physica Review Letters*, vol. **92**, no. 6, 2004.
doi:**10.1103/PhysRevLett.92.062501**.

[105] "https://www.nishina.riken.jp/collaboration/sunflower/," SUNFLOWER (Spectroscopy of Unstable Nuclei with Fast and sLOW beam Experiments at RIBF) Collaboration. Accessed: 2022-08-30.

[106] D. Rudolph *et al.*, "Isospin symmetry and proton decay: Identification of the 10+ isomer in 54Ni," *Physical Review C*, vol. **78**, no. 021301(R), 2008.
doi:**10.1103/PhysRevC.78.021301**.

[107] Y. Dong *et al. Nucl. Data Sheets 121, 1*, vol. 1, no. 121, 2014.

[108] X. Grave *et al.*, "NARVAL a modular distributed data acquisition system with ada 95 and RTAI," *Institut de Physique Nucléaire D'Orsay.*

[109] *GammaWare(GW) User's Guide.* Internal communication.
AGATA Data Analysis Team, 2013.

[110] *AGATA Data Analysis User's guide for Local Level Processing.* Internal communication.
AGATA Data Analysis Team, 2019.

[111] E. Calore and D. Mengoni, "AGATA DAQ: a NARVAL prototype installation and test," *LNL Annual Report*, 2008.

[112] *AGATA Data Analysis User's guide Global Level Processing.* Internal communication.
AGATA Data Analysis Team, 2018.